QUANTITATIVE IMAGING OF SPINAL CORD USING DIFFUSION MAGNETIC RESONANCE IMAGING

by

Nabraj Sapkota

A dissertation submitted to the faculty of
The University of Utah
in partial fulfillment of the requirements for the degree of

Doctor of Philosophy

in

Physics

Department of Physics and Astronomy

The University of Utah

May 2017

THE UNIVERSITY OF UTAH GRADUATE SCHOOL

STATEMENT OF DISSERTATION APPROVAL

The dissertation of **Nabraj Sapkota**

has been approved by the following supervisory committee members:

Brian Saam	, Chair	**09/13/2016** Date approved
Eun-Kee Jeong	, Member	**09/13/2016** Date approved
Dennis L. Parker	, Member	**09/13/2016** Date approved
Vikram V. Deshpande	, Member	**09/13/2016** Date approved
Gernot Laicher	, Member	**09/13/2016** Date approved

and by **Benjamin C. Bromley** ,Chair/Dean of

the Department /College/School of **Physics and Astronomy**

and by **David B. Kieda**, Dean of The Graduate School.

ABSTRACT

The spinal cord provides the major pathway for the signal transmission between the brain and peripheral nervous system. Any injury on the spinal cord may disrupt the signal transmission partially or completely, and lead to the permanent disability of the patient. Therefore, a technique which can evaluate the spinal cord disease burden and monitor the treatment progress noninvasively is very essential. Magnetic resonance imaging (MRI) has emerged as a powerful tool for imaging of the spinal cord because of its high soft-tissue contrast and specificity to the pathologic cord. However, using the conventional MRI methods such as T_1-weighted and T_2-weighted imaging, the disease burden and monitoring process cannot always be assessed accurately. An advanced imaging method, the diffusion MRI of spinal cord, has been proven as a more successful imaging method than the conventional MRI methods to detect the lesions in earliest stages; however, diffusion MRI of spinal cord is challenging. The major technical challenges for the high-resolution diffusion MRI of the spinal cord include the low signal-to-noise ratio (SNR) from the small cross-sectional area and deep location of the cord, large field inhomogeneity in the static magnetic field due to the magnetic susceptibility difference between tissue-bone interface, and patient's involuntary as well as voluntary motions. In addition to the above technical challenges, the signal behavior and outcomes of the diffusion MRI cannot be easily interpreted in the spinal cord because of its complex microscopic structure.

This dissertation contributes significantly in three areas to overcome the difficulties currently faced in diffusion MRI of the spinal cord. A Monte Carlo simulation (MCS) of water diffusion in white matter (WM) has been developed and performed. The simulation provides the deeper understanding of the signal measured in diffusion MRI, which facilitates easier interpretation of the outcomes of diffusion MRI. The results of the ultrahigh-b radial diffusion-weighted imaging (UHB-rDWI) of excised pig cervical spinal cord (CSC) agree fairly well with the results of the simulation.

An improvement in the SNR of the spinal cord images was achieved by constructing an 8-channel CSC dedicated coil, which does not require a commonly used preamplifier decoupling technique to minimize the interaction between nonadjacent elements. The newly constructed coil provides 1.4−2 time SNR improvement compared with the manufacturer's coil (Siemens' head neck and spine matrix).

A new sequence, 2D single-shot diffusion-weighted stimulated echo planar imaging with reduced field of view (2D ss-DWSTEPI-rFOV), has been developed for the UHB-rDWI of the spinal cord. The 2D ss-DWSTEPI-rFOV sequence acquires an image in a single excitation, and thereby reduces motion related artefacts. The reduced phase field of view imaging capability of the new sequence minimizes the off-resonance (field inhomogeneity and chemical shift) related artefacts. The time efficient sequence acquires stimulated echoes (STE) for the high-resolution UHB-rDWI of the spinal cord.

To my parents and wife

TABLE OF CONTENTS

LIST OF TABLES

LIST OF ACRONYMS

2D	Two Dimensional
ADC	Apparent Diffusion Coefficient
CHPC	Center for High Performance Computer
CSC	Cervical Spinal Cord
CSC-WM	Cervical Spinal Cord White Matter
DTI	Diffusion Tensor Imaging
DW	Diffusion Weighted
DWI	Diffusion Weighted Imaging
DWSE	Diffusion Weighted Spin Echo
DWSTE	Diffusion Weighted Stimulated Echo
EA	Extra-Axonal
EMF	Electromotive force
EPI	Echo Planar Imaging
EV	Eigenvector
FA	Fractional Anisotropy
FID	Free Induction Decay
FOV	Field of View
GM	Gray Matter
GPD	Gaussian Phase Distribution

GRE	Gradient Echo
IA	Intra-Axonal
IDEA	Integrated Development Environment for Applications
LMI	Light Microscopy Image
MCF	Monoexponential Plus Constant Fitting
MCS	Monte Carlo Simulation
MD	Mean Diffusivity
MoM	Method of Moment
MPI	Message Passing Interface
MR	Magnetic Resonance
MRI	Magnetic Resonance Imaging
NF	Noise Figure
NMR	Nuclear Magnetic Resonance
ODI	Orientation Dispersion Index
PBS	Phosphate Buffered Saline
PGSE	Pulse-field Gradient Spin Echo
RF	Radio Frequency
ROI	Region of Interest
SC	Spinal Cord
SE	Spin Echo
SNR	Signal to Noise Ratio
SOS	Sum of Square
SPG	Short Gradient Pulse

STE	Stimulated Echo
TE	Echo Time
TR	Repetition Time
T/R	Transmit/Receive
TSE	Turbo Spin Echo
UHB	Ultra-High-b
UHB-rDWI	Ultrahigh-b Radial Diffusion Weighted Imaging
WM	White Matter

ACKNOWLEDGEMENTS

I would first like to express my deepest gratitude to my Ph.D. advisor, Professor Eun-Kee Jeong. Without his incredible patience and continuous effort, my understanding of the basic principles of MRI could not be complete. His endless assistance to solve the problems related not only to my research, but also to my personal life made this dissertation possible. I am greatly indebted to him for his guidance and support.

I would also like to thank Professor Denis Parker for initially introducing me the world of MRI and the UCAIR. I am also thankful to other members of my Ph.D. committee; Professors Brian Saam, Vikram Deshpande, and Gernot Laicher for generously taking their time to serve on my Ph.D. committee. My deep appreciation goes to Dr. John Rose for providing me the profound knowledge of the anatomy and diseases of the spinal cord. This thesis would not have been completed without his constant support. I am especially thankful to Professor Scott Miller for his support and encouragement.

My heartily thanks also go to my colleagues Bijaya Thapa, YouJoung Lee, and KC Erb; visiting scholars Drs. Hyung Suk Seo and Sook Yoon; and collaborators Drs. Lubdha Shah and Erica Bisson, for their valuable contributions on my thesis. My thanks also go to a number of people, who have contributed to this thesis in one or other way.

Finally, but most importantly, I would like to express my sincere and deep appreciation to my parents and wife. Without their unconditional love and invaluable

care, I would not have completed this work. I cannot forget to thank my son Rowan and daughter Riana for their sweet smiles and words, which energized me every morning and evening to complete this work.

CHAPTER 1

INTRODUCTION

1.1 Motivations

The spinal cord is an important structure in the human body, which provides the main pathway for the signal transmission between the brain and body. The human spinal cord is an approximately cylindrical structure contained in the vertebral column. The spinal cord extends from the medulla caudally down to the disc between the first and second lumbar vertebrae and is roughly 42−45 cm long and 1 cm in diameter (1). A spinal cord cross-section is composed of a butterfly-shaped gray matter (GM) core surrounded by the outer white matter (WM). The white matter is composed of longitudinally placed tracts of axons which are surrounded by the myelin sheaths, and the gray matter is made of the neurons and glia. A lipid bilayer myelin, which surrounds the axons in the WM, is a lipid riched membrane (70−80 % lipid and 20−30 % protin by dry weight) (2).

Any injury on the spinal cord interferes with the signal transmission between the brain and peripheral nerves, which may cause permanent disability in the patients. Common spinal cord injuries or diseases are traumatic spinal cord injury, chronic spinal cord myelopathy, and autoimmune neurodegenerative diseases such as multiple sclerosis and amyotrophic lateral sclerosis. An inflammatory disorder disease, multiple sclerosis, is

characterized by inflammation, demyelination, incomplete remyelination, axonal loss, and gliosis. Multiple sclerosis is the most common neurological disorder among young people (3). A disease or injury in the spinal cord can have a devastating impact on the physical and mental health of the affected individual, their families and society. Therefore, a noninvasive evaluation technique, which describes the disease burden of the spinal cord and its recovery after a therapy, is highly desired.

Magnetic resonance imaging (MRI) has emerged as a powerful noninvasive imaging method for the spinal cord because of its high soft-tissue contrast and specificity to the pathologic cord (4). Conventional MRI of the spinal cord includes T_1-weighted and T_2-weighted imaging. T_1-weighted imaging provides the anatomic detail, and G_d-based contrast is usually employed to detect disruption of the blood-brain barrier that implies a more acute (or active) lesion. T_2-weighted imaging may provide the best combination of lesion detection and artefact minimization. However, it is commonly accepted that these conventional imaging methods usually under-detect actual cord lesions. It is also difficult to distinguish between neuronal structures and interstitial parenchymal tissues using these conventional MRI techniques (5). Therefore, various advanced high resolution imaging methods such as diffusion and perfusion MRI have emerged in the area of spinal cord imaging.

Diffusion MRI relies on the diffusive (Brownian) motion of water molecules in the tissue. Although diffusion MRI is known to provide a unique biomarker to evaluate spinal cord diseases, the interpretation of the diffusion MRI measurements is not always straightforward because the diffusive motion of water molecules in the complex biological tissue is not simply Gaussian. It is impossible to derive an analytical solution of the

Bloch-Torry equation (6), which describes the tissues' bulk magnetization, and hence, the signal behavior in the presence of the diffusion-weighted (DW) gradient. Therefore, a Monte Carlo simulation (MCS) of water diffusion in biological tissue may provide in-depth knowledge of the origin of the signal behavior observed in the diffusion MRI.

Diffusion MRI with low-b (b is determined from the applied gradient field strength, and its duration and separation between two gradient lobes) is not always successful for the detection of spinal cord abnormalities (7,8). The use of diffusion MRI with ultrahigh-b diffusion-weighting has been evolving for spinal cord imaging. Although ultrahigh-b diffusion MRI of the spinal cord is beneficial to detect the pathologic changes, there are three major technical challenges for ultrahigh-b diffusion MRI of the spinal cord. First, obtaining ultrahigh-b ($b > 5000$ s/mm^2) DW images in most clinical scanners with gradient field strength 40 mT/m is almost impossible using a conventional spin-echo as the signal decays heavily during the long echo-time (TE ~150 ms) due to the relatively short T_2 (80−100 ms). Secondly, a single-shot diffusion-weighted echo planar imaging (EPI) technique is commonly used for diffusion MRI of the spinal cord to minimize motion related artefacts. However, the severe geometrical distortion is induced on the images obtained with conventional single-shot EPI because of the large field inhomogeneity in the static field created by the magnetic susceptibility change in the bone-tissue interface. The distortion can be minimized by effectively reducing the field of view (FOV) in the phase-encoding direction. Therefore, single-shot DW stimulated echo planar imaging (EPI) with a reduced phase FOV scheme is desired.

Thirdly, the spinal cord images, which are acquired using the reduced FOV technique, suffer from low signal-to-noise ratio (SNR) because of reduced amount of the

measured data. The SNR of an image can be improved either by increased signal averaging or by using a spinal cord dedicated array coil. Use of the spinal cord dedicated array coil has been often the preferred choice because it increases subject comfort and reduces imaging cost by shorting imaging time. Therefore, a dedicated array is desired for high-quality imaging of the spinal cord.

1.2 Outline of the Dissertation

There are six chapters in this dissertation, including this "Introduction" chapter. Chapter 2 introduces the basic principles and theories used in this dissertation. The basic principles of nuclear magnetic resonance have been discussed in section 2.1. Then, the principles of the magnetic resonance imaging are briefly introduced in section 2.2. The concept of diffusion MRI is described in section 2.3. The design and construction strategies of surface and phased array coils are presented in the last section of Chapter 2.

Chapter 3 demonstrates an application of ultrahigh-b radial diffusion-weighted imaging (UHB-rDWI) for characterization of WM. The results of the MCS of water diffusion in WM provide in-depth knowledge of the signal behavior observed in the diffusion-weighted imaging (DWI) of WM. The results of the UHB-rDWI of the excised pig cervical spinal cord (CSC) support the findings of the MCS.

Chapter 4 describes the construction of a CSC dedicated 8-channel receive-only array. The array is designed to use 50 Ω preamplifiers instead of commonly used low-input impedance preamplifiers. The new 8-channel CSC array yields higher SNR in T_2-weighted imaging, DWI, and UHB-rDWI of the cervical spinal cord compared with the manufacturer's coil (Siemens' head, neck, and spine array).

In Chapter 5, a new acquisition scheme for the UHB-rDWI, 2D single-shot diffusion–weighted stimulated EPI with reduced FOV (2D ss-DWSTEPI-rFOV), is presented. The time efficient 2D ss-DWSTEPI-rFOV sequence can acquire high-resolution ultrahigh-b DW images of localized structures such as spinal cord and optic nerve with significantly reduced distortion, and without aliasing artefact.

Finally, in Chapter 6, summary and overall conclusions of this dissertation and suggestions for the future works are presented.

CHAPTER 2

PRINCIPLES OF MAGNETIC RESONANCE IMAGING

2.1 Nuclear Magnetic Resonance Physics

2.1.1 Historical Perspectives

The history of nuclear magnetic resonance (NMR) can be traced back to the fundamental work performed by Rabi[1] and his group in the 1930s (9,10). Rabi and his group demonstrated that a stream of hydrogen molecules sent through a magnetic field in the presence of the radio frequency (RF) energy could absorb the RF energy at specific frequencies. Later in 1946, the NMR phenomenon was first observed in bulk materials independently by Bloch, Hansen, and Packard at Stanford University (11) and by Purcell, Torrey, and Pound at Harvard University (12).[2] The concept of nuclear relaxation and dipole-dipole interaction in a solid and liquid was explained by Bloembergen, Purcell, and Pound (13) in 1948. Since then, NMR has bloomed as a major tool in physics and chemistry to study the dynamic and structural properties of molecules. NMR has also been used to study the structural information of proteins in biology. After the first use of NMR in medicine in the 1970s, it became an indispensable method to obtain magnetic resonance images and spectra of human tissues noninvasively for diagnostic purposes.

[1]Rabi received the Nobel Prize in Physics in 1944 for the discovery of the resonance method for recording the magnetic properties of the atomic nuclei.
[2]In 1952, Bloch and Purcell received the Nobel Prize in Physics for their NMR discoveries.

2.1.2 Nuclear Magnetic Moments

An atomic nucleus is composed of neutrons and protons. The magnetic moment of a nucleus arises from a nonzero spin angular momentum of the nucleons (protons and neutrons). In the classical description, the magnetic moment $\vec{\mu}$ of a nucleus is related to the spin angular momentum $\vec{J}$ by

$$\vec{\mu} = \gamma \vec{J} \qquad [2.1]$$

where γ is the gyromagnetic ratio constant and is a nucleus-dependent constant, for instance, 2.675 $\times 10^8$ rads/s/T ($\gamma/2\pi = 42.59$ MHz/T) for ^{1}H and 7.705 $\times 10^7$ rads/s/T ($\gamma/2\pi = 11.26$ MHz/T) for ^{31}P.

In the quantum mechanical approach, the nuclear magnetic moment is related to the nuclear spin quantum number I by

$$\mu = \gamma\hbar\sqrt{I\,(I+1)} \qquad [2.2]$$

where $\hbar = h/2\pi = 1.05\times 10^{-34}$ Js and h is Plank's constant.

The spin quantum number I takes zero or half-integer or integer values such that

$$I = 0,\ 1/2,\ 1,\ 3/2,\ \ldots \qquad [2.3]$$

The value of the spin quantum number I for a particular nucleus is determined by the following rules: (i) nuclei with an odd mass number, such as ^{1}H, ^{13}C, and ^{23}Na, have half-integral spin quantum number, (ii) the nuclei with an even mass number and an even proton number, such as ^{12}C and ^{16}O, have zero spin quantum number, and (iii) the nuclei with an even mass number and an odd proton number, such as ^{2}H, ^{14}N, and ^{6}Li, have integral spin quantum number. The values of γ and I of the selected nuclei common in the human body are listed in Table 2.1.

Table 2.1: List of the selected nuclei common in the human body with their gyromagnetic ratio and spin quantum number.

Nucleus	Gyromagnetic ratio ($\gamma/2\pi$) MHz/T	Spin quantum number (I)
^{1}H	42.58	1/2
^{13}C	10.71	1/2
^{17}O	−5.77	5/2
^{19}F	40.08	1/2
^{23}Na	11.27	3/2
^{31}P	17.25	1/2
^{2}H	6.54	1

2.1.3 Classical Description

A nucleus with a nonzero spin quantum number creates a magnetic field around it, which is analogous to the magnetic field created by a bar magnet. When a nucleus with a nonzero spin quantum number is placed in a magnetic field ($\vec{B}$), it experiences a torque

$$\vec{\tau} = \vec{\mu} \times \vec{B} \qquad [2.4]$$

The torque is defined as a rate of change in the angular momentum $\frac{d\vec{J}}{dt}$. Therefore, one can rewrite Eq. [2.4] as

$$\frac{d\vec{J}}{dt} = \vec{\mu} \times \vec{B} \qquad [2.5]$$

Since $\vec{\mu} = \gamma\vec{J}$, Eq. [[2.5] becomes

$$\frac{d\vec{\mu}}{dt} = \gamma\vec{\mu} \times \vec{B} \qquad [2.6]$$

Assuming $\vec{B}$ is along the z-direction, i.e., $\vec{B} = B_0\,\vec{k}$, Eq. [2.62.6] can be rewritten as

$$\frac{d\vec{\mu}}{dt} = \gamma\vec{\mu} \times B_0\,\vec{k} \qquad [2.7]$$

Eq. [2.7] is the equation of motion for isolated spins in the classical treatment. In terms of the components, one can write Eq. [2.7] as

$$\begin{cases} \dfrac{d\mu_x}{dt} = \gamma B_0 \mu_y \\ \dfrac{d\mu_y}{dt} = -\gamma B_0 \mu_x \\ \dfrac{d\mu_z}{dt} = 0 \end{cases} \quad [2.8]$$

After differentiating $\frac{d\mu_x}{dt}$ and $\frac{d\mu_y}{dt}$ with respect to t and substituting the values of $\frac{d\mu_y}{dt}$ and $\frac{d\mu_x}{dt}$, Eq. [2.8] becomes

$$\begin{cases} \dfrac{d^2\mu_x}{dt^2} = -\omega_0^2 \mu_x \\ \dfrac{d^2\mu_y}{dt^2} = -\omega_0^2 \mu_y \\ \dfrac{d\mu_z}{dt} = 0 \end{cases} \quad [2.9]$$

where $\omega_0 = \gamma B_0$ is the Larmor frequency. The components μ_x and μ_y follow the equation of harmonic motion. The general solution of the second-order differential equation which obeys harmonic motion is in the form $A\cos(\omega_0 t) + B\sin(\omega_0 t)$. Setting the initial conditions to $\mu_x(0)$, $\mu_y(0)$, and $\mu_z(0)$, one can write the solution of Eq. [2.9] as

$$\begin{cases} \mu_{xy}(t) = \mu_{xy}(0)\, e^{-i\omega_0 t} \\ \mu_z(t) = \mu_0(0) \end{cases} \quad [2.10]$$

where i is an imaginary number and $\mu_{xy}(t) = \mu_x(t) + i\,\mu_y(t)$. The solution (Eq. [2.10]) of the equation of motion of an isolated spin describes that the magnetic moment $\vec{\mu}$ precesses about the applied external magnetic field $B_0\vec{k}$ with the angular frequency $\omega_0 = \gamma B_0$, as depicted in Figure 2.1.

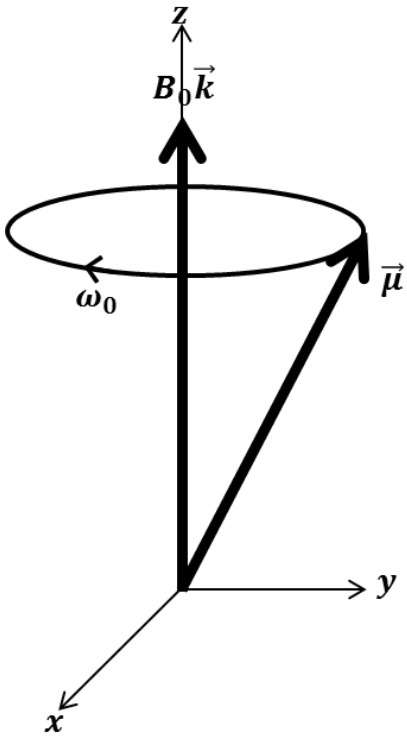

Figure 2.1: Precession of an isolated spin magnetic moment in an external magnetic field.

We have thus far discussed the behavior of an isolated spin magnetic moment in the presence of a static magnetic field. Let us now study the behavior of an isolated nuclear spin magnetic moment in the presence of both the static and oscillating magnetic fields. Suppose an isolated spin is placed in the presence of a static magnetic field $\vec{B} = B_0\vec{k}$ and an oscillating magnetic field $\vec{\mathrm{B}}_1(t) = B_1 \cos(\omega t)\,\vec{\imath}$, where B_1 is the field amplitude and ω is the excitation carrier frequency. The linearly polarized $\vec{\mathrm{B}}_1(t)$ field can be mathematically decomposed into two circularly polarized fields rotating in opposite directions,

$$\vec{\mathrm{B}}_1(t) = \frac{1}{2}B_1\,(\cos(\omega t)\vec{\imath} - \sin(\omega t)\,\vec{\jmath}) + \frac{1}{2}B_1\,(\cos(\omega t)\vec{\imath} + \sin(\omega t)\,\vec{\jmath}) \qquad [2.11]$$

where the first term rotates clockwise and the second term counter-clockwise. The second term rotates in the direction opposite to the spins precession, thus, exerts a negligible torque on a spin system. Therefore, one can drop the second term from Eq. [2.11] and then $\vec{\mathrm{B}}_1(t)$ can be expressed as

$$\vec{\mathrm{B}}_1(t) = \frac{1}{2} B_1 \left(\cos(\omega t)\vec{\imath} - \sin(\omega t)\,\vec{\jmath}\right) \qquad [2.12]$$

In the presence of both static and oscillating magnetic fields, the equation of motion Eq. [2.7] can be written as

$$\frac{d\vec{\mu}}{dt} = \gamma\vec{\mu} \times (B_0\,\vec{k} + \vec{\mathrm{B}}_1(t)) \qquad [2.13]$$

2.1.4 Quantum Description

An isolated nucleus with nuclear magnetic moment $\vec{\mu}$ interacts with the applied magnetic field $\vec{B}$. The energy of the interaction is described by the Zeeman interaction as

$$H = -\vec{\mu} \cdot \vec{B} \qquad [2.14]$$

Since $\vec{B} = B_0\,\vec{k}$, and $\vec{\mu} = \gamma\hbar\vec{I}$, where I is the spin quantum number of the nucleus. Eq. [2.14] can be rewritten as

$$H = -\gamma\hbar B_0 I_z \qquad [2.15]$$

The eigenvalues of this Hamiltonian are

$$E = -\gamma\hbar B_0 m \;\; m = I, I-1, \ldots, I \qquad [2.16]$$

and the most general time-dependent corresponding wave function is

$$\psi(t) = \sum_{m=-I}^{I} c_m u_{I,m}\, e^{-\frac{i}{\hbar}E_m t} \qquad [2.17]$$

where c_m and $u_{I,m}$, respectively, denote the complex constants and time independent solutions of the Schrödinger equation. In quantum mechanics, the expectation value of any observable, for instance μ_x, can be calculated as

$$< \mu_x(t) >= \int \psi^*(t)\mu_x\psi(t)d\tau \qquad [2.18]$$

For a spin 1/2 (I =1/2 and $m = -1/2,\ 1/2$) system, the expectation values of the components of the nuclear magnetic moment can be calculated using Eq. [2.18] as

$$\begin{cases} < \mu_x(t) > = \gamma\hbar ab\cos(\alpha - \beta + \omega_0 t) \\ < \mu_y(t) > = -\gamma\hbar ab\sin(\alpha - \beta + \omega_0 t) \\ < \mu_z(t) > = \gamma\hbar(a^2 - b^2)/2 \end{cases} \qquad [2.19]$$

where $c_{1/2} = ae^{i\alpha}$ and $c_{-1/2} = be^{i\beta}$ in Eq. [2.17]. Eq. [2.19] clearly describes that $< \mu_x >$ and $< \mu_y >$ oscillate in time at the Larmor frequency ω_0, but $< \mu_z >$ remains stationary.

In quantum mechanics, the equation of motion of an operator F can be written as

$$\frac{dF}{dt} = \frac{i}{\hbar}[HF - FH] \qquad [2.20]$$

Since $H = -\gamma\hbar B_0 I_z$ and $[I_x, I_y] = i\, I_z$, the equation of motion of an observable $\vec{I}$ becomes

$$\frac{d\vec{I}}{dt} = \vec{I} \times \gamma\vec{B} \qquad [2.21]$$

Since $\vec{\mu} = \gamma\hbar\vec{I}$, the equation of motion (Eq. [2.21]) of the expectation of the magnetization can be written as

$$\frac{d < \vec{\mu} >}{dt} = < \vec{\mu} > \times \gamma\vec{B} \qquad [2.22]$$

In the presence of both the static magnetic field $B_0\vec{k}$ and the oscillating magnetic field $\vec{B}_1(t) = B_1\cos\omega t\,\vec{i}$, the equation of motion (Eq. [2.22]) can be rewritten as

$$\frac{d\vec{\mu}}{dt} = \vec{\mu} \times \gamma(B_0\vec{k} + \vec{\mathrm{B}}_1(\mathrm{t})) \quad [2.23]$$

Consider a frame of reference which is rotated at the frequency ω about z-axis, the equation of motion in the rotating frame becomes

$$\frac{\partial\vec{\mu}}{\partial t} = \vec{\mu} \times \gamma[(B_0 - \frac{\omega}{\gamma})\vec{k} + B_1\,\vec{\imath}] \quad [2.24]$$

This equation is equivalent to the classical equation of motion of the magnetization. The quantum mechanical treatment of an isolated spin in the presence of both static and oscillating magnetic fields is presented in detail by Slichter (14).

2.1.5 Bulk Magnetization

In a sample containing a large number of spins, the bulk (total) magnetization is the vector sum of all the spin magnetic moments ($\vec{\mu}$) within the sample. Mathematically, the bulk magnetization ($\vec{M}$) of a spin system is defined as

$$\vec{M} = \sum_{n=1}^{N} \overrightarrow{\mu_n} \quad [2.25]$$

where N is the total number of spins in the sample.

In the absence of an external magnetic field, the magnetic moments of the spins are orientated randomly due to thermal agitation, resulting in zero net magnetization ($\vec{M} = 0$). Consider a case of spin 1/2 system. When an external magnetic field is applied to a spin system, the magnetic moment of the spins will be oriented either parallel or antiparallel to the field. According to the theory of quantum mechanics, the energy level of a spin 1/2 system splits into two energy levels in the presence of an external magnetic

field as shown in Figure 2.2. The splitting of the energy level in the presence of a static magnetic field is also known as Zeeman splitting.

The quantum particles, spins, obey quantum statistics, specifically, Fermi-Dirac statistics. However, at the high-temperature limit, the Fermi-Dirac statistics reduces to the classical Boltzmann statistics. Therefore, the population difference of the spins in two spin states is given by Boltzmann statistics as

$$n = N_{\frac{1}{2}} - \mathrm{N}_{-\frac{1}{2}} \approx \mathrm{N}\frac{\gamma\hbar \mathrm{B}_0}{2k_B \mathrm{T}} \qquad [2.26]$$

where k_B is the Boltzmann constant and T is the absolute temperature of the spin system. Equation [2.26] is derived in the high-temperature approximation, which requires $\gamma\hbar B_0 \ll k_B T$. The requirement of the high-temperature approximation is certainly achieved at room temperature (300 K) for the commonly available static field strength $1-20$ T.

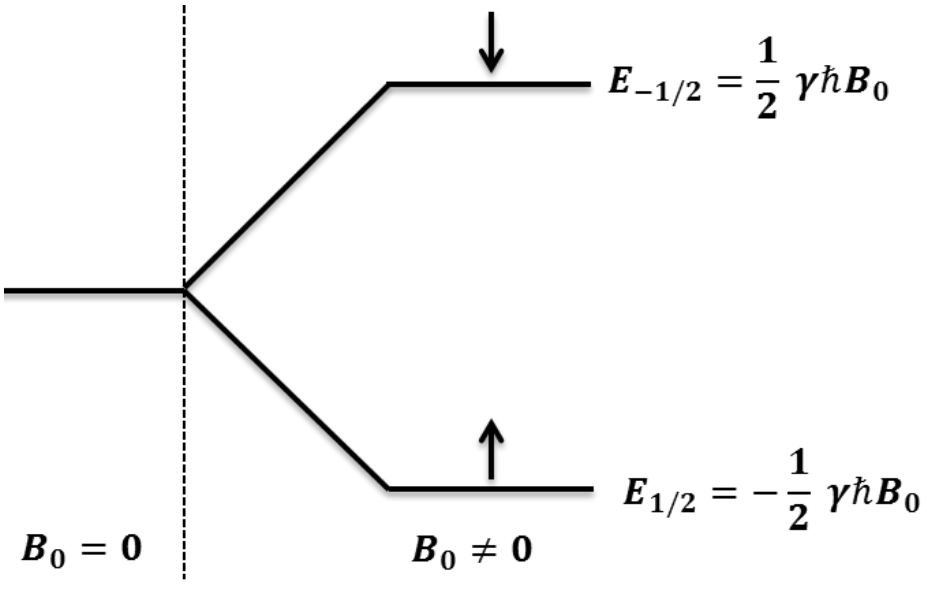

Figure 2.2: Splitting of the energy level of spin 1/2 system in the presence of an external magnetic field (Zeeman splitting).

The population difference between two states is calculated as ~ 6 ppm using Eq. [2.26] at room temperature (300 K) in the presence of static magnetic field strength of 3 T. Only six spins out of one-million spins contributes to the NMR signal, therefore, the NMR/MRI is considered a low sensitive technique. The bulk magnetization of a spin system is now calculated as (14)

$$\vec{M} = n|\mu_z|\vec{k} = \mathrm{N}\frac{\gamma^2\hbar^2\mathrm{B}_0}{4\mathrm{k}_\mathrm{B}\mathrm{T}}\vec{k} \qquad [2.27]$$

It should be noted that the expression for the bulk magnetization, Eq. [2.27], is derived for the spin 1/2 system. For a spin I system, the expression becomes

$$M_z^0 = |\vec{M}| = \mathrm{NI}\,(\mathrm{I}+1)\frac{\gamma^2\hbar^2\mathrm{B}_0}{3k_B\mathrm{T}} \qquad [2.28]$$

also known as Curie's law of magnetization.

2.1.6 Bloch Equation

In the previous subsections 2.1.3 and 2.1.4, the precession of a microscopic magnetic moment (individual spin) has been described in the presence of an external magnetic field. However, the bulk magnetization precesses as well as relaxes in the presence of an external magnetic field. The relaxation of the bulk magnetization was first described by Felix Bloch in 1946. The equation, which describes the precession and relaxation of the bulk magnetization, is called the Bloch equation and is given by

$$\frac{d\vec{M}}{dt} = \gamma\vec{M}\times\vec{B} - \frac{M_x\vec{\imath} + M_y\vec{\jmath}}{T_2} - \frac{(\mathrm{M_z} - M_z^0)\vec{k}}{T_1} \qquad [2.29]$$

where M_z^0 is the thermal equilibrium value of the bulk magnetization $\vec{M}$ in the presence of an external static field $B_0\vec{k}$. T_1 and T_2 are time constants characterizing the relaxation

process of a spin system after being disturbed from its equilibrium state. The solution of the Bloch equation is well known and described in Slichter's book (14).

2.1.7 Relaxation Times

In the presence of an external static magnetic field $B_0\vec{k}$, thermal equilibrium magnetization (longitudinal magnetization) M_z^0 is built in a spin system. When an oscillating magnetic field (radio frequency pulse) is applied in addition to the $B_0\vec{k}$, the equilibrium state of the system is perturbed. As a result, the transverse magnetization M_{xy} is created. According to the laws of thermodynamics, a system in perturbed state returns back to the equilibrium state, provided the external perturbation is removed and sufficient time is allowed. The relaxation process in which the longitudinal magnetization recovers back to the equilibrium positon is known as spin-lattice or longitudinal relaxation (T_1 −relaxation) and the relaxation process in which the transverse magnetization destructs is known as spin-spin or transverse relaxation (T_2 −relaxation).

Spins excited into higher energy states are relaxed back into the lowest energy state by transferring the excess energy to the molecule or atom (other than the spins), also known as a lattice. The translational, rotational, and vibrational motions of a molecule due to the thermal energy create a complex magnetic field around the nucleus. The T_1 −relaxation is determined by the fluctuating magnetic field which is responsible for the transition of the spin states from the higher to lower energy states. The fluctuating magnetic field is mainly caused by dipole−dipole interaction between water molecules.

In the transverse plane, phase coherence of spins is lost due to spin diffusion, which causes the decrease in the transverse component of the magnetization. In contrast

to the T_1 −relaxation, the T_2 −relaxation occurs without transferring energy between the lattice and spin systems; but it occurs with the exchange of energy between neighboring spins through flip-flop transitions. Spin diffusion is mainly caused by the dipole-dipole interaction between two adjacent spin magnetic moments.

2.2 Basic Principles of Magnetic Resonance Imaging

2.2.1 Historical Perspective

In 1971, Raymond Damadian discovered a difference in relaxation time of water protons in normal tissue and tumor, which could be used to distinguish cancer from healthy tissue (15). After this discovery, scientists attempted to use NMR for diagnostic purposes. In 1973, Paul Lauterbur obtained a first magnetic resonance (MR) image on small test tube samples by applying magnetic field gradients (16). Peter Mansfield developed an ultra-fast imaging method called "echo-planar imaging (EPI)" in 1975 (17). The first MR image obtained by Lauterbur[3] was constructed using a back projection technique. In the same year of Mansfield's development of the EPI method, Richard Ernst[4] introduced MR imaging using phase and frequency encoding and the Fourier Transform techniques (18). In 1977, Damadian constructed the first magnetic resonance imaging (MRI) scanner and the first human MR image was produced using the field focused NMR voxel-imaging technique. The first MR image was acquired by scanning the subject for nearly 5 h. After the 1970s pioneer works in the field of MR imaging, there have been tremendous advances in MR imaging techniques and hardware. With the

[3]Lauterbur and Mansfield were jointly awarded the 2003 Nobel Prize in Physiology or Medicine for their discoveries regarding the magnetic resonance imaging.
[4]Ernst received the Novel Prize in Chemistry in 1991 for his discovery of the pulsed Fourier Transform NMR spectroscopy and its derivates.

recent improvements and advances in MR imaging techniques and hardware, the scope of MRI has been expanding from the macroscopic (mm scale) to microscopic (μm scale) imaging. Today, MRI is routinely used to study dynamic properties, such as self-diffusion, flow, and relaxation, of human tissue for diagnostic purposes.

2.2.2 Signal Detections

MR signal is detected based on Faraday's law of electromagnetic induction and the principle of reciprocity. An electromotive force (EMF) is induced in a properly oriented RF coil due to the precessing transverse magnetization of a sample resulting from the application of an external static as well as the alternating magnetic field. The magnetic flux linkage through a coil by the precessing magnetization $\vec{M}(\vec{r},t)$ at a distance $\vec{r}$ from the coil is given by

$$\phi(t) = \int \vec{B}(\vec{r}) \,.\, \vec{M}(\vec{r},t)\, \mathrm{d}r^3 \qquad [2.30]$$

where $\vec{B}(r)$ is the magnetic field at the location $\vec{r}$ produced by an imaginary unit DC flowing in the coil. According to Faraday's law of electromagnetic induction, the EMF induced in the coil is

$$emf = -\frac{\partial \phi(t)}{\partial t} = -\int \vec{B}_{xy}(\vec{r}).\frac{\partial \vec{\mathrm{M}}_{\mathrm{xy}}(\vec{r},t)}{\partial \mathrm{t}}\, \mathrm{d}r^3 \qquad [2.31]$$

The z-term in the Eq. [2.31] is ignored because $M_z(\vec{r},t)$ varies very slowly for $T_1 \sim$ 1 sec compared to $M_{xy}(\vec{r},t)$. Since $M_{xy}(\vec{r},t) \propto M_z^0 e^{-i\omega_0 t}$, the induced EMF is proportional to the thermal equilibrium magnetization (M_z^0), resonance frequency (ω_0), and detection sensitivity ($\vec{B}_{xy}$) of the receive coil.

2.2.3 Imaging Gradients

Imaging of an object requires position-dependent information. In MRI, the signals are basically encoded using selective excitation and spatial encodings. Modern MRI systems are equipped with three independent orthogonal gradient coils. The thickness of an imaging slice is often selected using a slice-selection gradient (selective excitation). After the spins in a slice have been excited by a selective RF pulse, the spatial information along the other imaging directions is obtained using frequency-encoding (readout) and phase-encoding gradients.

An RF pulse can only be a frequency selective; therefore, it is necessary to make the spin resonance frequency position dependent. When a gradient field is applied along the slice-selection direction, the magnetic field along the slice direction varied linearly and hence spins at different positions precess at different frequencies. An RF pulse (certain bandwidth), which is applied simultaneously with a slice-selection gradient, excites the spins only from a selected frequency band. The carrier frequency (f_1) of a slice-selective RF pulse and strength of the slice-selection gradient (G_{ss}) are determined by the desired slice thickness (Δz), bandwidth (Δf_{RF}) of the RF pulse, and position of the slice from the magnet's isocenter (z_1) as

$$\begin{cases} f_1 = \dfrac{\gamma}{2\pi}(B_0 + \mathrm{G_{ss}z_1}) \\ \Delta f_{RF} = \dfrac{\gamma}{2\pi} G_{ss}\Delta z \end{cases} \qquad [2.32]$$

The frequency encoding is performed by applying a frequency-encoding (readout) gradient orthogonal to the slice-selection gradient at the time of data acquisition. This gradient spatially encodes signals by making the Larmor frequency of the spins position-dependent as in the slice-selection process. An inverse Fourier transform of the time

domain signal reveals the frequency content. The strength of the frequency-encoding gradient (G_{R0}), total receiver bandwidth (BW_{rcv}), and readout field-of-view (FOV_{RO}) are related to each other as

$$\Delta k_x = \frac{\gamma}{2\pi\ BW_{rcv}} G_{RO} = \frac{1}{FOV_{RO}} \quad [2.33]$$

where Δk_x is the spacing between data points in k-space along the readout direction. The total receiver bandwidth is related to the sampling rate as $BW_{rcv} = 1/\Delta t_{rcv}$.

Phase encoding is accomplished in the Cartesian k-space sampling by creating a linear spatial variation in the phase of the magnetization. The phase-encoding gradient, which is applied orthogonal to both the slice- and frequency-ending gradients, creates a linear spatial variation in the phase of the magnetization. Different k-space lines are acquired with the different amounts of the spatial phase variation by varying the area under the phase-encoding gradient. An inverse Fourier transform of the signals reveals the spatial information of the object. The gradient strength increment (ΔG_p) between two adjacent k-space lines is related to the duration of the gradient (T) and phase field-of-view (FOV_{phase}) as

$$\Delta k_y = \frac{\gamma}{2\pi} \Delta G_p \mathrm{T} = \frac{1}{FOV_{phase}} \quad [2.34]$$

where Δk_y is the spacing between data points in k-space along the phase-encoding direction.

2.2.4 Imaging Hardware

Thus far, in the previous section 2.1 and subsections 2.2.1-2.2.3, we have discussed the essential principles of MRI. A static field is required to polarize the

randomly orientated magnetic moments, an oscillating magnetic field (RF pulse) is required to perturb the equilibrium longitudinal magnetization, and three orthogonal magnetic gradient fields are required for the spatial encoding of the signal. Either a superconducting, a permanent, or an electromagnet is used to generate the static magnetic field. A Helmholtz or Golay pair is used to creating a linear field gradient across the sample. There are various types of RF coils for transmission of the RF pulses and reception of the NMR signal. A diagram of a modern MR system equipped with all these components is depicted in Figure 2.3

Often, the RF coil equipped in the commercial MRI system does not provide good sensitivity during the signal receptions. Therefore, a custom made RF coil is used in most MRI experiments. Some description of the RF coil is presented in section 2.5 of this dissertation. When a custom coil is used for imaging, an addition circuitry, known as transmit/receive (T/R) switch, is also required. A basic circuit diagram of the T/R switch is shown in Figure 2.4. The details of the T/R switch are presented in (19).

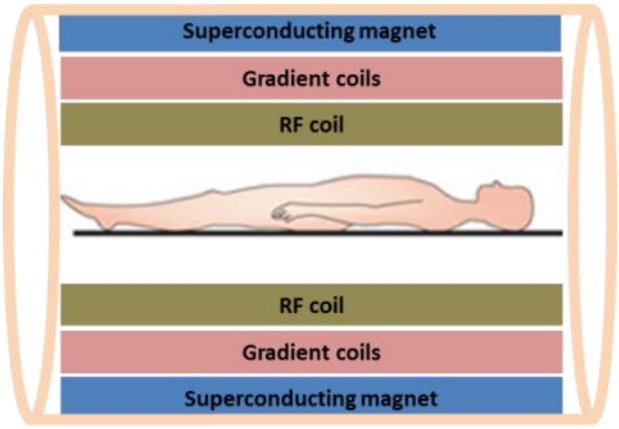

Figure 2.3: A diagram of MRI system.

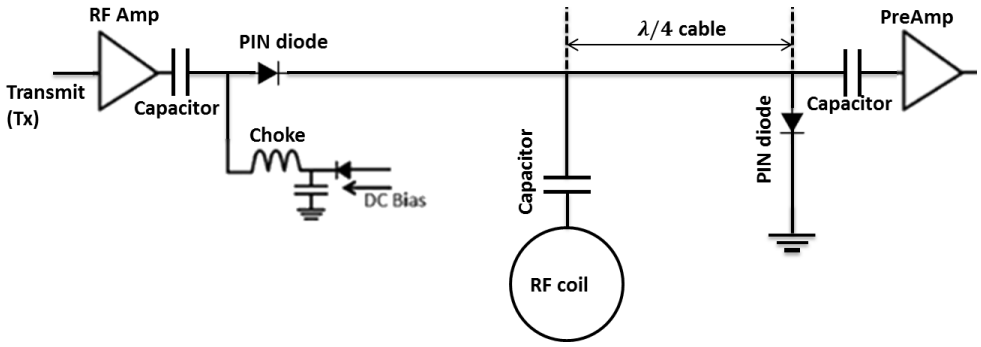

Figure 2.4: Basic circuit diagram of TR-switch.

2.3 Basic MRI Pulse Sequences

2.3.1 Historical Prospective

The concept of the free induction decay (FID) began with the discovery of the NMR phenomenon by Bloch (11). In 1950, spin echo (SE) also known as Hahn echo was described by Hahn (20). Thereafter, SE imaging became an indispensable acquisition technique in NMR and MRI. The stimulated echo (STE) was also described by Hahn (20) together with the SE. Later, STE was used for the NMR diffusion measurements (21). In 1975, Peter Mansfield developed an ultra-fast imaging method called EPI. Imaging of tissue, which requires fast imaging methods (i.e., cardiac imaging), was possible after the discovery of EPI. Applications of advanced imaging methods such as diffusion, perfusion, and functional MRI were speeded after the innovation of EPI.

2.3.2 Free Induction Decay

A FID is the NMR signal decay in the transverse plane following a single RF excitation pulse. An RF pulse excites the spins from an equilibrium state (longitudinal magnetization) to a nonequilibrium state (transverse and longitudinal magnetizations).

The precessing transverse magnetization induces an EMF (a few mV) in a properly oriented RF coil. The pulse sequence diagram of an FID sequence is shown in Figure 2.5. The signal equation of a FID resulting from a α pulse ($\alpha -$ flip angle) can be written as

$$S(t) = sin\alpha \int_{-\infty}^{\infty} \rho(\omega) e^{-\frac{t}{T_2(\omega)}} e^{-i\omega t}\, \mathrm{d}\omega \qquad [2.35]$$

where $\rho(\omega)$ is the spectral density function. $\rho(\omega)$ determines the characteristics of the FID signal. For a spin system with a single spectral component resonating at a frequency ω_0, one can rewrite the signal equation as

$$S(t) = M_z^0 sin\alpha\, e^{-\frac{t}{T_2}}\, e^{-i\omega_0 t} \qquad [2.36]$$

where $M_z^0 = \int_{-\infty}^{\infty} \rho(\omega)\, d\omega$ is the equilibrium longitudinal magnetization of the system. The FID signal (Eq. [2.36]) decays at a rate $1/T_2$. This happens only when both the sample and the static magnetic field (B_0) are homogeneous. When the magnetic field is

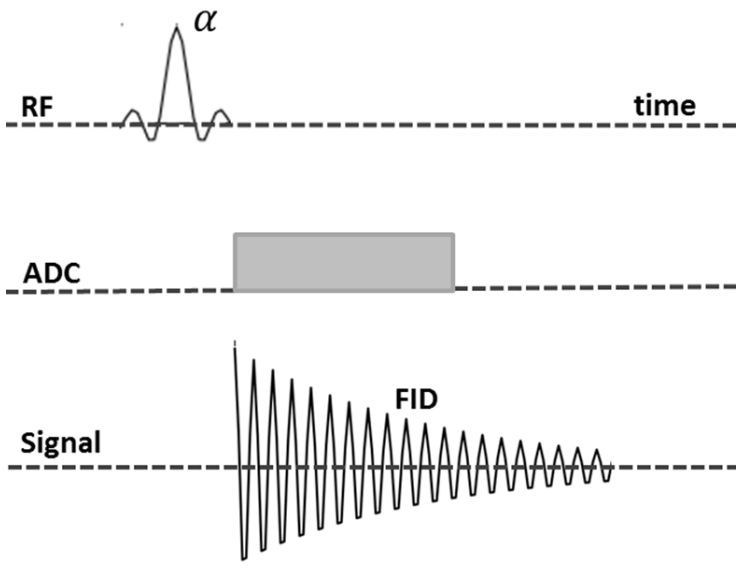

Figure 2.5: FID pulse sequence diagram

inhomogeneous, the FID signal decays at a faster rate $1/T_2^*$ where

$$\frac{1}{T_2^*} = \frac{1}{T_2} + \gamma \Delta B_0 \qquad [2.37]$$

where ΔB_0 is the full width at half maximum of the local field distribution.

2.3.3 Gradient Echo Imaging

Gradient echo (GRE) imaging is a basic imaging technique which uses a single RF pulse. An echo is formed by applying the dephasing and rephasing gradient lobes along the frequency-encoding (readout) direction. The GRE imaging technique can acquire the images in the very short time as it uses a single RF pulse with a small flip angle. This technique is widely used for imaging of the tissue that requires fast imaging, for instance, cardiac and abdominal imaging. The GRE signal decays at the same rate as the FID signal, i.e., the signal decays at a rate given by $1/T_2^*$.

When a magnetic field gradient is applied, spins at different x-positions accumulate different phases, and hence, the phase coherence among the spins is lost. As a result, the FID signal decays much faster than T_2^* decay. Phase accumulated by a spin located at a position x due to the application of gradient G_x is given by the equation

$$\phi(x,t) = \gamma \int_0^t G_x x dt \qquad [2.38]$$

Details of the GRE sequence are described elsewhere (22). A typical GRE pulse sequence diagram is shown in Figure 2.6. The first gradient lobe with the duration τ dephases spins, resulting in the rapid signal loss. However, the second gradient lobe with the same amplitude but an opposite polarity rephases the spins after time τ (center of the second lobe), producing a gradient echo.

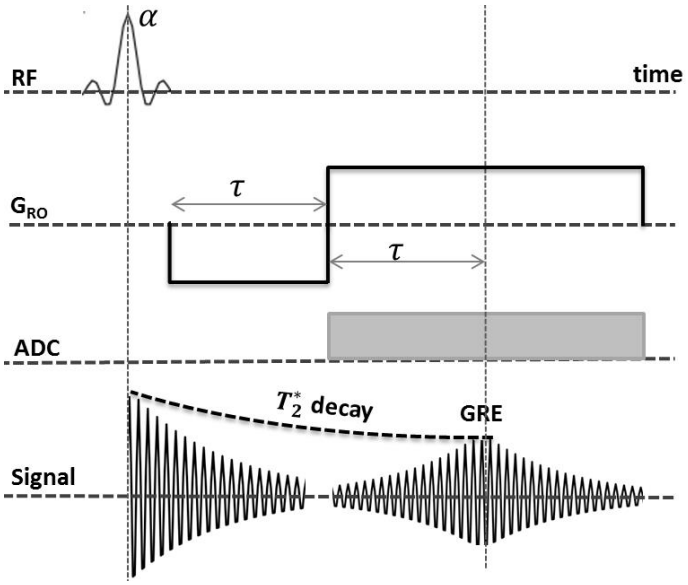

Figure 2.6: GRE pulse sequence diagram. All other gradients are not displayed for clarity.

2.3.4 Spin Echo Imaging

SE imaging is the most common and fundamental MR imaging method, which uses two or more RF pulses. A SE is formed by an excitation (usually 90°) and one or more refocusing pulses (usually 180°). A pulse sequence diagram for the SE sequence is shown in Figure 2.7. In FID and GRE, the signal decays at the faster rate (T_2^*) due to off-resonance effect caused by field inhomogeneity in the static magnetic field (B_0). The inhomogeneity in B_0 arises due to the magnetic susceptibility variations, chemical shift, nonuniformity in the applied field, and the spin-spin interactions. However, the effect of the field inhomogeneity related to the magnetic susceptibility, chemical shift, and nonuniformity in the applied field is removed at the peak of the Hahn echo. SE imaging is therefore only sensitive to signal loss due to spin-spin interaction (T_2 −decay). Thus, the SE imaging method is susceptible to fewer artefacts than the GRE imaging. Details of the SE sequence are described elsewhere (22).

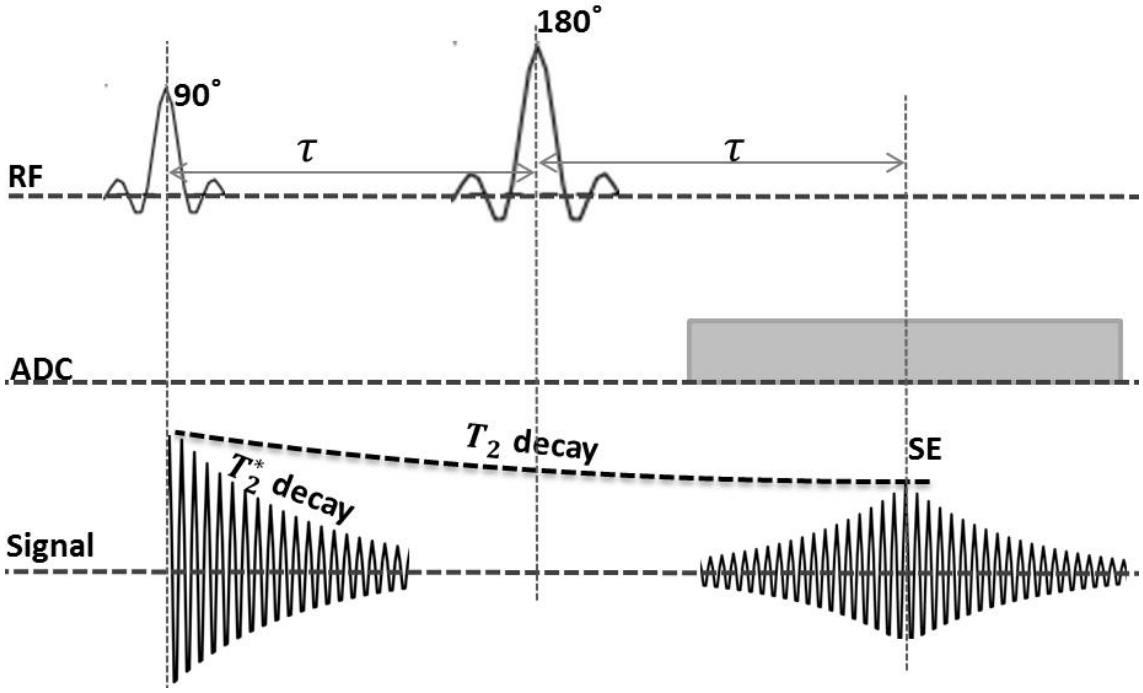

Figure 2.7: SE pulse sequence diagram. Imaging gradients are not shown for clarity.

2.3.5 Stimulated Echo Imaging

STE imaging, which uses three RF pulses, is the more complicated than the SE imaging and rarely used in conventional imaging. The STE signal decays due to both spin-spin and spin-lattice relaxation. The maximum amplitude of the STE is a half of that of the SE when all three RF pulses have flip angle 90° (23). A typical STE imaging sequence is shown in Figure 2.8. Three RF pulses generate three FIDs (FID_1-FID_3), three primary SEs (SE_{12}, SE_{23}, and SE_{13}), one secondary SE (SE_{123}), and one STE (STE_{123}) (24). FID_1-FID3 are generated by the α_1, α_2, and α_3 RF pulses, respectively. SE_{12} and SE_{13} are formed when FID_1 is refocused by the α_2 and α_3 RF pulses, respectively. SE_{23} is formed when the FID_2 is refocused by the α_3 RF pulse. Secondary SE (SE_{123}) is formed when FID_1 is refocused twice by the α_2 and α_3 RF pulses. The stimulated echo STE_{123} is

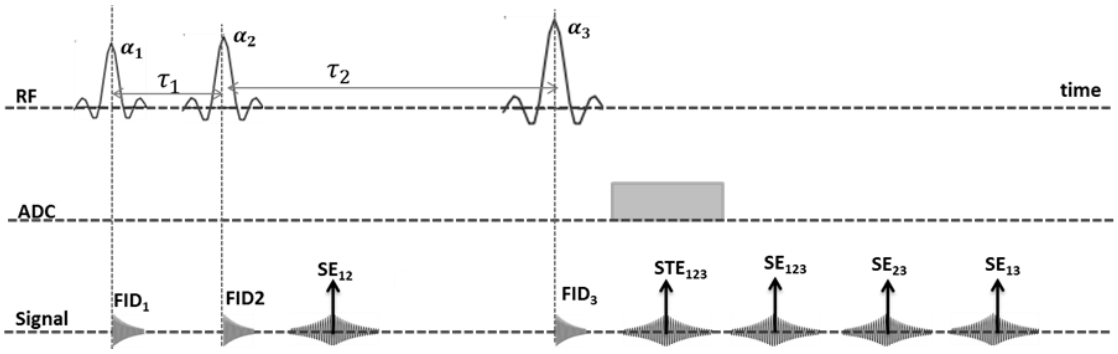

Figure 2.8: STE pulse sequence diagram. Three FIDs (FID_1-FID_3), three primary spin echoes (SE_{12}, SE_{23}, SE_{13}), one secondary spin echo (SE_{123}), and one stimulated echo (STE_{123}) can be measured with three RF pulses. Imaging gradients are not shown for clarity.

formed when a portion of transverse magnetization prepared by the α_1 pulse is flipped to the longitudinal direction by the α_2 pulse and the longitudinal magnetization prepared by the α_2 pulse is then flipped back to the transverse plane after time τ_2 by the α_3 pulse. The STE magnetization decays at a rate of T_2-deay in the transverse plane and at a rate of T_1-decay during τ_2 in the longitudinal plane. The amplitudes of all the echoes with echo times are presented in Table 2.2.

Table 2.2: Echo times and amplitudes of the echoes formed by three RF pulses (25).

Echo	Echo time	Echo amplitude
SE_{12}	$2\tau_1$	$M_z^0 sin\alpha_1 \sin^2\frac{\alpha_2}{2}\, e^{-2\tau_1/T_2}$
STE_{123}	$2\tau_1+\tau_2$	$\frac{1}{2}M_z^0\, sin\alpha_1 sin\alpha_2 sin\alpha_3 e^{-\tau_2/T_1} e^{-2\tau_1/T_2}$
SE_{123}	$2\tau_2$	$-M_z^0 sin\alpha_1 \sin^2\frac{\alpha_2}{2}\sin^2\frac{\alpha_3}{3} e^{-2\tau_1/T_2}$
SE_{23}	$\tau_1+2\tau_2$	$A sin\alpha_2 \sin^2\frac{\alpha_3}{3} e^{-(\tau_1+2\tau_2)/T_2}$
SE_{13}	$2(\tau_1+\tau_2)$	$M_z^0 sin\alpha_1 \cos^2\frac{\alpha_2}{2}\sin^2\frac{\alpha_3}{3} e^{-2(\tau_1+\tau_2)/T_2}$
$A = M_z^0[1-(1-\cos\alpha_1)e^{-\frac{\tau_1}{T_1}}]$		

2.3.6 Echo Planar Imaging

EPI is one of the fastest and most commonly used MR imaging methods to obtain the dynamic properties of tissue such as diffusion and perfusion. An EPI pulse sequence differs from the conventional pulse sequences mainly in the application of the readout and phase encoding gradients. In conventional pulse sequences, a single echo is measured in each excitation while multiple echoes are measured in EPI by periodically rewinding the readout gradient. A full set of k-space is measured in a single shot EPI from a FID using the gradient-echo trains, which results in a very fast imaging acquisition. Single-shot EPI is widely used for diffusion and perfusion MR imaging. However, chemical shift and Nyquist ghost artefacts are more severe in EPI sequences compared to conventional spin and gradient echo sequence. A gradient echo EPI pulse sequence is illustrated in Figure 2.9.

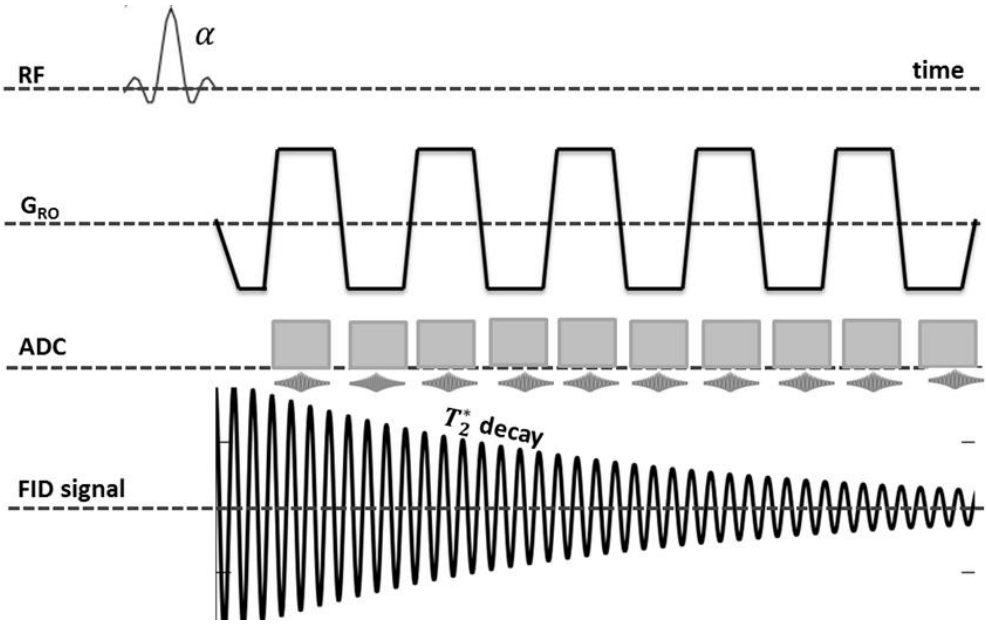

Figure 2.9: Gradient-based EPI pulse sequence diagram. Slice selection and phase encoding gradients are not displayed for clarity.

2.4 Diffusion MRI

2.4.1 Historical Perspective

Dynamic properties like self-diffusion, flow, and relaxations of matter can be studied using MRI. In the very early work of NMR (1950), the effect of molecular diffusion on the amplitude of the spin-echo in the presence of an inhomogeneous magnetic field was pointed out by Hahn (20). In 1965, the pulsed-field gradient spin echo (PGSE) method was first theoretically and experimentally demonstrated by Stejskal and Tanner (26) and is still one of the main NMR/MRI methods to measure a dynamic property of matter (tissue), the self-diffusion coefficient. In 1985, the first diffusion-weighted imaging (DWI) was introduced by Le Bihan et al. (27), Taylor et al. (28), and Merboldt et al. (29). DWI became a powerful MRI technique ever since Moseley demonstrated an early diagnosis of acute stroke in cats using DWI in the early 1990s (30).[5]

In 1976, anisotropic diffusion was first observed in muscle using diffusion NMR (31). After the advent of DWI, in the early 1990s, diffusion anisotropy was also detected in the spinal cord (32) and brain white matter (33). In 1994, the pioneering work on diffusion anisotropy really led to the introduction of the most rigorous formalism of the diffusion tensor by Basser[6] et al. (34). The diffusion anisotropy effects can be fully extracted and characterized with the diffusion tensor imaging (DTI). DTI may also provide details of tissue microstructure. Recently, various diffusion MRI methods such as q-space imaging which was originally introduced by Cory and Garroway (35) and

[5]Le Bihan and M. Moseley received the Gold Medal of the International Society for Magnetic Resonance in 2001 for their pioneering work on the DWI.
[6]Basser received the 2008 International Society for Magnetic Resonance in Medicine Gold Medal for his pioneering and innovative work on the DTI.

Callaghan et al. (36), and model-based AxCaliber (37) and NODDI (38) have been proposed and investigated in the research studies; however, their clinical applications remain to be validated.

2.4.2 Free and Restricted Diffusion

Self-diffusion, also known as Brownian motion, is the random translational motion of molecules driven by thermal energy. Transportation of matter can be observed in all forms of materials such as gas, liquid, and solid. The diffusive motion is more prominent in liquids and gases than in solids because the binding energy between atoms or molecules in a solid is higher than that in a fluid. In case of free diffusive motion, shown in Figure 2.10, the probability of finding a molecule from original position $\vec{r}_0$ to final position $\vec{r}_1$ after a time t is described by a Gaussian function (39)

$$P(\vec{r}, t) = (4\pi Dt)^{-\frac{3}{2}} \, \mathrm{e}^{-\frac{r^2}{4Dt}} \qquad [2.39]$$

where $\vec{r} = \vec{r}_1 - \vec{r}_0$ is the displacement of the molecule during time t and D is the diffusion coefficient. The probability distribution function is the Gaussian with zero mean displacement and standard deviation $\sigma^2 = 2Dt$. The mean square displacement of the molecule is given by

$$< r^2 >= 6Dt \qquad [2.40]$$

The mean square displacement of the molecule is linearly proportional to the diffusion time. The factors that affect the molecular diffusion are molecular mass, viscosity, and temperature. The measured diffusion coefficient in free solution is independent of diffusion time. However, the diffusion of molecules in a biological tissue is not free but is restricted by various cellular microstructures. The diffusion

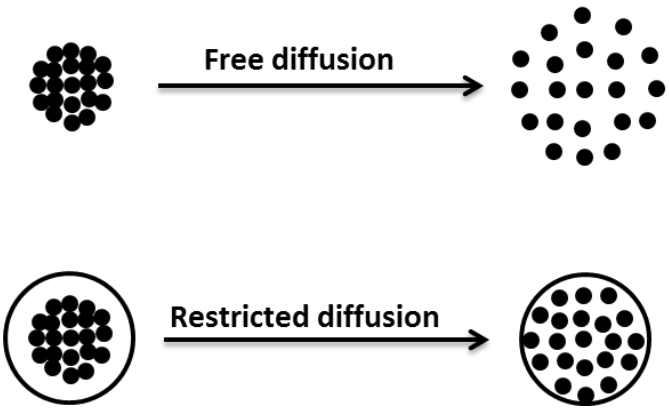

Figure 2.10: Diffusion of molecules in the free and restricted media.

phenomenon in a biological tissue is further complicated by the presence of various individual compartments such as intracellular, extracellular, neurons, glial cells, and axons. The displacement of a molecule in a restricted space depends on the diffusion time, diffusion coefficient, and shape and size of the restricting geometry. Therefore, the diffusion coefficient measured in a restricted space using the free diffusion model (Eq. [2.39] and Eq. [2.40]) may not represent the true diffusion coefficient rather it represents the apparent diffusion coefficient (ADC).

Price WS (40) described the effects of diffusion time, and shape and size of the restricting geometry on the displacement, and hence, the diffusion coefficient of the diffusing molecules. Price defined a degree of restriction of a hard sphere of radius R by defining a dimensionless variable

$$\xi = Dt/R^2 \qquad [2.41]$$

In the limit of short diffusion time ($\xi \ll 1$), most diffusing molecules cannot reach the boundary of the sphere to be restricted by it. Therefore, the calculated diffusion coefficient will be same as that for the freely diffusing molecules. As the diffusion time

becomes longer ($\xi \sim 1$), more molecules experience the effect of the boundary. The mean square displacement deviates from the linear relationship with diffusion time, i.e., the mean square displacement does not obey Eq. [2.40]. The calculated ADC will then be diffusion time dependent. For very long diffusion times ($\xi >> 1$), diffusing molecules experience the effect of boundary several times and the maximum displacement covered by the molecule is limited by the boundary, and thus, the mean square displacement becomes independent of diffusion time, i.e., the Eq. [2.40] is no longer valid.

2.4.3 Isotropic and Anisotropic Diffusion

In the previous subsection 2.4.2, we have discussed the molecular diffusion in free and restricted media. Isotropic diffusion has always been observed in free medium; however, the diffusion of molecules in a restricted medium can be either isotropic or anisotropic depending on the shape of the restricting geometry. If the distance traveled by a diffusing molecule is the same in all directions, for example, diffusion inside a sphere ($R \sim 1$ μm), the diffusion is isotropic. On the other hand, if the distance travelled by a diffusing molecule is longer in one direction than others, for example; diffusion inside a cylinder ($R \sim 1$ μm, $L = 1$ m) where a molecule travels a longer distance along the axial direction than the perpendicular direction as shown in Figure 2.11, the diffusion is anisotropic. Free diffusion can be observed in human cerebrospinal fluid. The diffusion in gray matter is restricted and almost isotropic as the cell membranes and other microorganelles interfere the free diffusion equally in all directions. Anisotropic diffusion can be observed in white matter and muscle because of the directional preference of their microscopic structure.

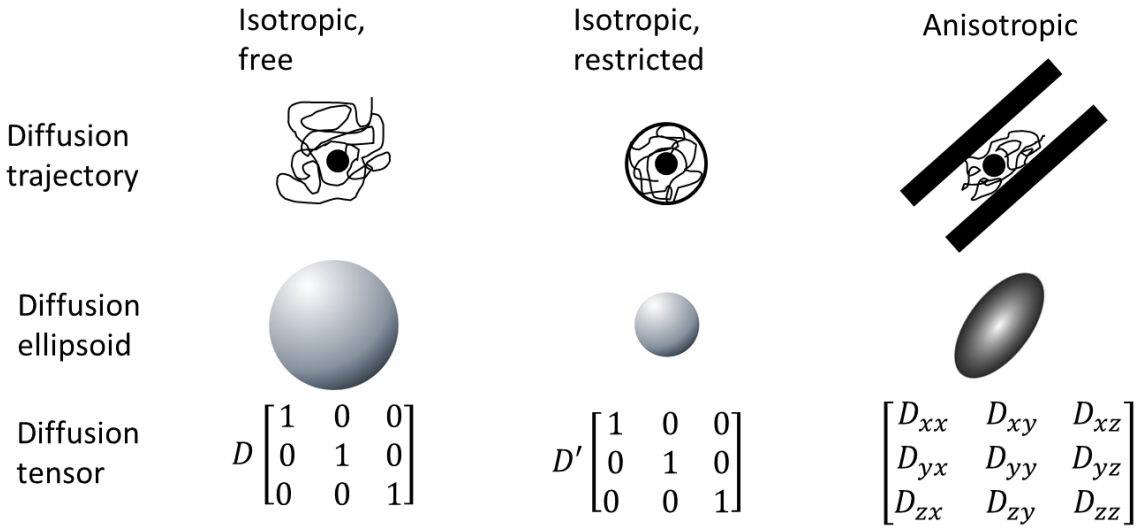

Figure 2.11: Isotropic and anisotropic diffusion.

In the case of isotropic diffusion, molecules diffuse equally in all directions and the diffusion can be described by a scalar diffusion coefficient, D. For restricted diffusion, molecules may travel different displacement along the different directions. Therefore, the scalar diffusion coefficient may not be sufficient to describe the diffusive motion. One should consider a tensor diffusion coefficient $\boldsymbol{D}$ to describe anisotropic diffusion. The tensor diffusion coefficient is a symmetric second rank tensor, i.e., 3 × 3 matrix

$$\mathbf{D} = \begin{bmatrix} D_{xx} & D_{xy} & D_{xz} \\ D_{yx} & D_{yy} & D_{yz} \\ D_{zx} & D_{zy} & D_{zz} \end{bmatrix} \qquad [2.42]$$

where upper and lower off-diagonal elements are identical, i.e., $D_{xy} = D_{yx}, D_{xz} = D_{zx}, D_{yz} = D_{zy}$. For a restricted medium, the components of the diffusion tensor may have different values for the different directions. Moreover, if the principal axis of a system is rotated with respect to the coordinate system, the tensor will be different for

different angles of rotations. Therefore, the information obtained from the tensor about the system is very minimal. To make the measurement rotationally invariant (i.e., independent of the angle of rotation), $\boldsymbol{D}$ should be diagonalized. The diagonalized tensor will be same for the same anatomical tissues regardless of their orientations with respect to the scanner.

Let us now look at an example of a diffusion tensor in restricted medium. First, let us start with an example of isotropic diffusion in a sphere as shown in Figure 2.12(a). The diffusion tensor in a sphere can be written as

$$\mathbf{D} = \lambda \begin{bmatrix} 1 & 0 & 0 \\ 0 & 1 & 0 \\ 0 & 0 & 1 \end{bmatrix} \qquad [2.43]$$

where λ is the diffusivity of the molecules, also known as eigenvalue of the diffusion tensor. For isotropic diffusion, the off-diagonal elements of $\boldsymbol{D}$ are all zero and the diagonal elements are equal. The diffusion tensor may be replaced by a scalar λ.

Second, let us consider an example of anisotropic diffusion in a cylinder shown in Figure 2.12(b) where the principal axis of the cylinder coincides with one axis of the coordinate system. The diffusion tensor in the cylinder can be written in the form

$$\mathbf{D} = \begin{bmatrix} \lambda_3 & 0 & 0 \\ 0 & \lambda_2 & 0 \\ 0 & 0 & \lambda_1 \end{bmatrix} = \lambda \begin{bmatrix} 1 & 0 & 0 \\ 0 & 1 & 0 \\ 0 & 0 & 2 \end{bmatrix} \qquad [2.44]$$

where λ_1 is the diffusivity along the cylindrical axis (axial diffusivity) and $\lambda_2 = \lambda_3$ is the diffusivity perpendicular to the cylindrical axis (radial diffusivity). For simplicity, the axial diffusivity is considered to be twice the radial diffusivity, i.e., $\lambda_1 = 2\lambda$ and $\lambda_2 = \lambda_3 = \lambda$. When the principal axis of a cylindrical symmetric medium coincides with an axis of the coordinate system, the off-diagonal elements of $\boldsymbol{D}$ are also zero.

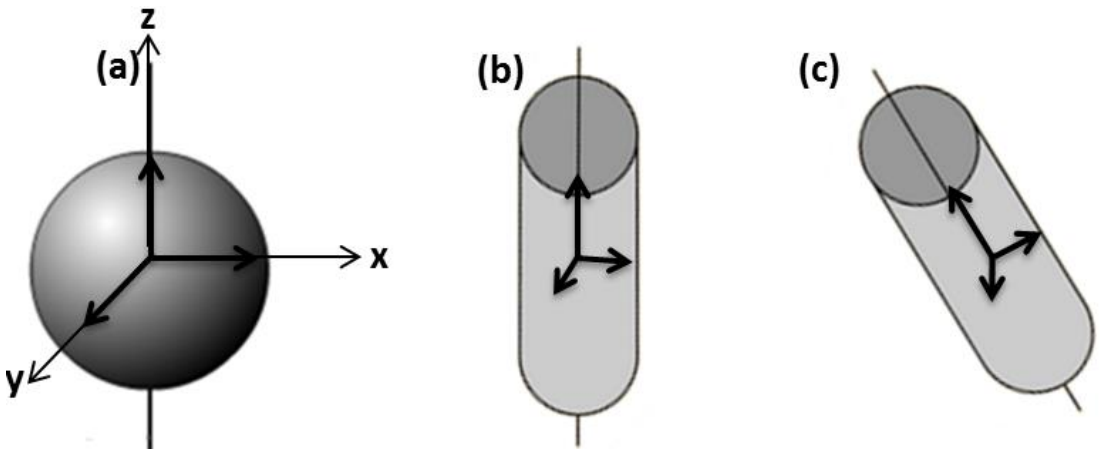

Figure 2.12: Diffusion of molecules in a (a) sphere (isotropic), (b) cylinder with the principal axis coincides with the z-axis of the coordinate system (anisotropic), and (c) cylinder with principal axis rotated with respect to the z-axis of the coordinate system by 45˚ about the y-axis (anisotropic).

In the third and last example, consider a diffusion phenomenon inside a cylinder whose principal axis does not coincide with the coordinate system as shown in Figure 2.12(c). The principal axis of the cylinder is rotated by 45˚ about the y-axis. The rotation matrix for a system rotated by 45˚ about the y-axis can be written as

$$\mathbf{R} = \begin{bmatrix} \cos(45^o) & 0 & -\sin(45^o) \\ 0 & 1 & 0 \\ \sin(45^o) & 0 & \cos(45^o) \end{bmatrix} \quad [2.45]$$

For simplicity, the rotated diffusion tensor for the cylinder can be written as

$$\mathbf{D} = \boldsymbol{R}\,\lambda \begin{bmatrix} 1 & 0 & 0 \\ 0 & 1 & 0 \\ 0 & 0 & 2 \end{bmatrix} \mathbf{R}^{\mathrm{T}} = \begin{bmatrix} 1.5 & 0 & -0.5 \\ 0 & 1 & 0 \\ -0.5 & 0 & 1.5 \end{bmatrix} \quad [2.46]$$

Two different diffusion tensors (Eq. [2.44] and Eq. [2.46]) have been calculated for the same cylinder with two different angles of rotation of the principal axis with respect to the coordinate system. This clearly demonstrated the need of diagonalization of the diffusion tensor.

2.4.4 Solution of Bloch Equation with Diffusion Term

The effect of diffusion on macroscopic magnetization was first added in the Bloch equation by the Torrey (6) in 1956. The Bloch equation for the macroscopic magnetization including the diffusion term, also known as Bloch-Torrey equation, is given by

$$\frac{d\vec{M}}{dt} = \gamma\vec{M} \times \vec{B} - \frac{M_x\vec{\imath} + M_y\vec{J}}{T_2} - \frac{(M_z - M_z^0)\,\vec{k}}{T_1} + D\boldsymbol{\nabla}^2\vec{M} \qquad [2.47]$$

Assume the $\vec{B}$ field is along the z-axis and a superimposed field vanishing at the origin with gradient $\vec{G}$ in the z-axis, then

$$B_x = 0,\ B_y = 0,\ B_z = B_0 + \vec{G}.\vec{r} \qquad [2.48]$$

For simplicity of calculation, T_1 and T_2 relaxations are neglected, Eq. [2.47] can be written in components form as

$$\begin{cases} \dfrac{dM_x}{dt} = \gamma B_z M_y + D\boldsymbol{\nabla}^2 M_x \\ \dfrac{dM_y}{dt} = -\gamma B_z M_x + D\boldsymbol{\nabla}^2 M_y \\ \dfrac{dM_z}{dt} = D\boldsymbol{\nabla}^2 M_z \end{cases} \qquad [2.49]$$

The transverse component of the Bloch equation with the diffusion term (Eq. [2.49]) can be rewritten as

$$\frac{dM_{xy}}{dt} = -i\omega_0 M_{xy} - i\gamma\vec{G}.\vec{r}M_{xy} + D\boldsymbol{\nabla}^2 M_{xy} \qquad [2.50]$$

where $M_{xy} = M_x + iM_y$ is the transverse component of the macroscopic magnetization. Stejskal and Tanner (26) solved the Bloch equation (Eq. [2.50]) for the PGSE and the solution is given by

$$\ln(E) = -\gamma^2 G^2 \delta^2 D(\Delta - \frac{\delta}{3}) \quad [2.51]$$

where $ln(E)$ is the natural logarithm of the echo attenuation resulting from diffusive motion of the molecules under the application of field gradients. δ is the duration of the applied gradient pulse and Δ the separation between the leading edge of the applied gradient pulse pair. The term $\delta/3$ accounts for the finite duration of the gradient pulses. For short gradient duration ($\delta/3 \ll \Delta$) and large gradient amplitude G, the Stejskal-Tanner solution (Eq. [2.51]) becomes

$$\ln(E) = -\gamma^2 G^2 \delta^2 D\Delta \quad [2.52]$$

For the case of a steady gradient throughout the echo sequence, i.e., $\Delta = \delta$, the Stejskal-Tanner solution (Eq. [2.51]) becomes

$$\ln(E) = -\frac{2}{3}\gamma^2 G^2 \delta^3 D \quad [2.53]$$

This is Hahn's (20) famous result for the spin echo intensity, and Car and Purcell (41) result in the echo attenuation due to the application of a field gradient in a diffusive medium.

Stejskal and Tanner's solution of the Bloch-Torrey equation is derived based on the assumption that molecules diffuse freely in the medium, i.e., molecules diffuse according to Fick's law (42). For anisotropic and restricted diffusion, Stejskal (43) modified Torrey's approach to include diffusion effects in the Bloch equation as

$$\frac{d\vec{M}}{dt} = \gamma\vec{M} \times \vec{B} - \frac{M_x\vec{\imath} + M_y\vec{\jmath}}{T_2} - \frac{(M_z - M_z^0)\,\vec{k}}{T_1} + \boldsymbol{\nabla}.\boldsymbol{D}.\boldsymbol{\nabla}\vec{M} \quad [2.54]$$

where $\boldsymbol{D}$ is a second rank diffusion tensor. Analytical solution of Eq. [2.54] is generally not possible for restricted diffusion. However, one can use various approximations to solve Eq. [2.54]. The most commonly used approximations are Gaussian phase

distribution (GPD) and short pulse gradient (SPG) approximations, which are discussed elsewhere (40). In the GPD approximation, phase distribution of spins is assumed as a Gaussian distribution. Gradient pulse is considered as a delta function ($\delta \to 0, G \to \infty$, and δG ~ finite) so that the spin motion during the gradient pulse is negligible in the SGP approximation. Biological cells are complex in shape and size, and the analytical solutions even using the above approximations are generally not possible. Thus, a numerical solution or Monte Carlo simulation must be performed for a deeper understanding of the signal behavior in the biological tissue under the presence of field gradients.

Let us study the echo attenuation in a restricted system composed of two parallel plates with a separation R in between where a homogeneous fluid is confined. The diffusive motion is free and unrestricted parallel to the plates, but restricted perpendicular to the plates. The SGP solution for the echo attenuation when a gradient field is applied perpendicular to the plates is given by (44)

$$E = \frac{2(1-\cos(2\pi qR))}{(2\pi qR)^2} + 4(2\pi \mathrm{qR})^2 \sum_{n=1}^{\infty} e^{-\frac{n^2\pi^2 D\Delta}{R^2}} \times \frac{1-(-1)^{\mathrm{n}}\cos(2\pi \mathrm{qR})}{((2\pi \mathrm{q})^2-(n\pi)^2)^2} \quad [2.55]$$

where $q = \gamma G\delta/2\pi$ is a wave vector. For the long diffusion time limit $\Delta \to \infty$, Eq. [2.55] reduces to

$$E = \frac{2(1-\cos(2\pi qR))}{(2\pi qR)^2} = |sinc(\pi qR)|^2 \quad [2.56]$$

Equation [2.56] is analogous to the intensity of a far-field single-slit diffraction pattern with diffraction minima at $q = n/R$, n = 1, 2, 3, 4.…The diffraction-like effect in the

echo attenuation clearly demonstrate the ability of diffusion MRI to detect the size of restrictions. For the details of the pulse gradient spin echo attenuation in free as well as restricted media, the reader is referred to the following articles (6,26,40,43).

2.4.5 Diffusion Weighted and Diffusion Tensor Imaging

Diffusive motion can be encoded by applying a pair of gradient lobes in MRI. Diffusion encoded MRI also known as DWI provides information not only about the molecules themselves but also about their background physical environment.

Spins precess at the rate proportional to the magnetic field strength. As the magnetic field is very uniform across the magnet, the precession rate is also very homogeneous and phase coherence is maintained across the sample. The coherent phase of the spins can be dispersed by applying a magnetic gradient field across the sample as shown in Figure 2.13. During application of the first gradient lobe along the y-axis, spins located at the different y-positions experience different magnetic fields, and hence, precess at different frequencies. The dispersed phase can be refocused by applying a second gradient lobe of the same duration and amplitude (the polarity required depends on whether the spin-echo or gradient-echo measurement is performed) as shown in Figure 2.14. For stationary spins, the second gradient lobe completely refocuses spins dephased by the first gradient lobe resulting in no signal loss due to the application of the gradient pair. On the other hand, diffusing spins are only partially refocused by the second gradient lobe and the signal is attenuated. The first gradient lobe dephases spins and is termed dephasing gradient and the second gradient lobe rephases spins and is termed as rephrasing gradient. The phase accumulated by a spin in the presence of gradient field is given by

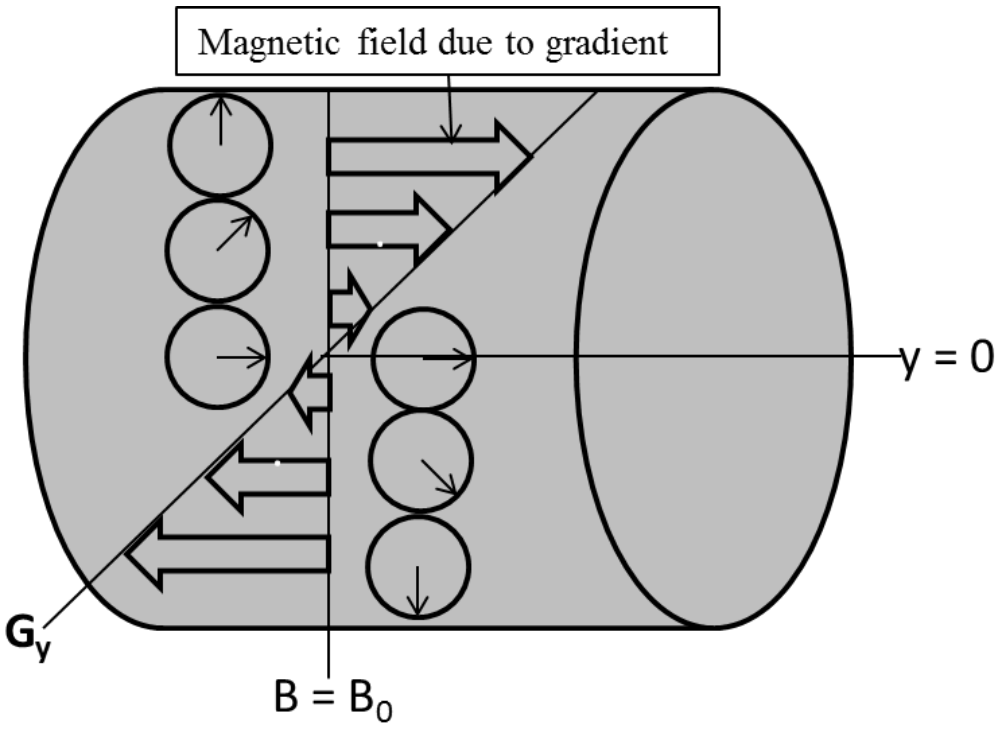

Figure 2.13: Phase dispersion in the presence of the field gradient (Gy) along y-axis on top of static magnetic field B_0, i.e., $\vec{B} = (B_0 + G_y y)\vec{k}$.

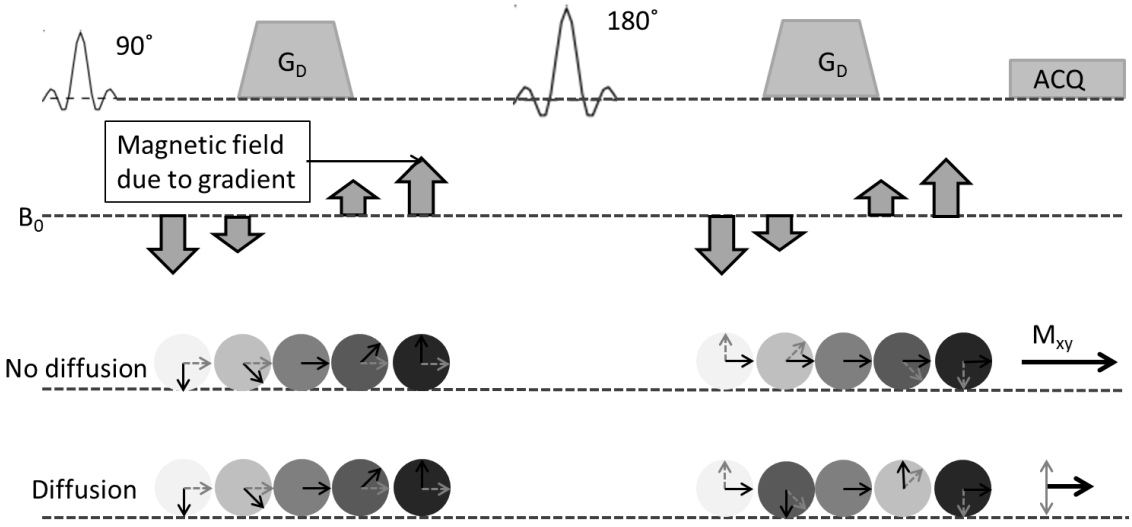

Figure 2.14: Loss of the transverse magnetization of the diffusing spins in the presence of diffusion-weighted gradient lobes. Gray-dashed and black solid arrows represent, respectively, the phase of the spin before and after each gradient lobe applied. M_{xy} is the transverse magnetization at the peak of the spin-echo.

$$\phi(t) = \phi_0(t) + \gamma \int_0^t G_y(\tau) y d\tau \quad [2.57]$$

where $\phi_0(t)$ is the phase accumulated due to static magnetic field B_0.

The most common diffusion-weighted (DW) imaging scheme is the Stejskal-Tanner (26) PGSE scheme. It consists of a pair of gradient lobes. The first gradient pulse is applied after the 90˚ excitation RF pulse and the second gradient pulse after the 180˚ refocusing RF pulse as shown in Figure 2.15.

In 1965, Stejskal-Tanner (26) proposed the solution for PGSE as given by Eq. [2.51]. Later in 1985, the Stejskal-Tanner solution was generalized by Le Bihan (27) as

$$S(b) = S_0 e^{-bD} \quad [2.58]$$

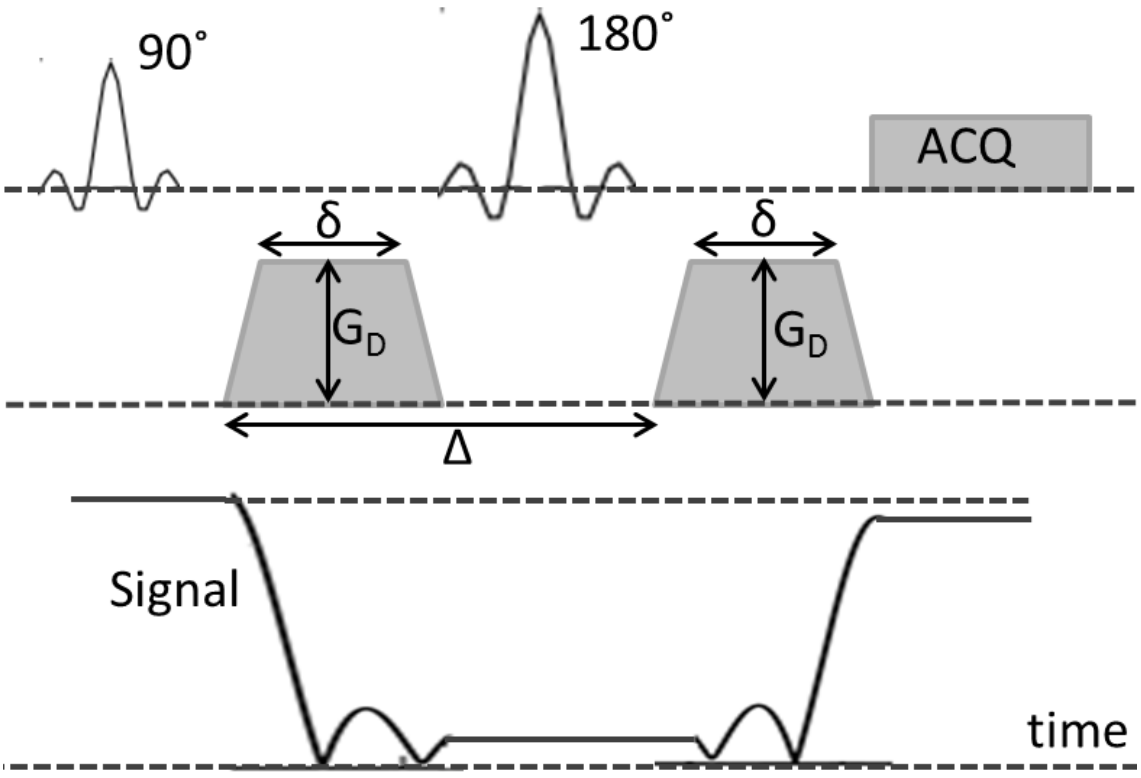

Figure 2.15: Stejskal-Tanner PGSE scheme for DW imaging. For the clarity, all other imaging gradients are not shown in the figure.

where $S(b)$ is the signal measured with the diffusion gradient and S_0 is the signal measured when diffusion gradient is turned off ($b = 0$ s/mm^2). D is the diffusion coefficient of the molecules along the direction of the applied diffusion gradient. The b is termed as "b-value" and is an attenuation factor depends on the sets of gradient lobes. For rectangular gradient pulse pairs, the b-value can be calculated to be

$$b = \gamma^2 G_D^2 \delta^2 (\Delta - \frac{\delta}{3}) \quad [2.59]$$

where δ is the duration of the applied gradient pulse and Δ is the separation between two gradient pulses (Figure 2.15). The diffusion coefficient D can be estimated from Eq. [2.58] by measuring signals for two different b-values as

$$D = -\ln(\frac{S(b)}{S_0})/b \quad [2.60]$$

Diffusion of water molecules in most biological tissue is either hindered or restricted. Therefore, D measured in most biological issues using DWI may not represent true or intrinsic diffusion coefficient but rather it represents the ADC. The DW images (b = 0, and b = 500 s/mm^2) and ADC map of the human cervical spinal cord is shown in Figure 2.16.

For isotropic diffusion, the diffusion tensor reduces to a scalar, and the ADC map can be obtained from two DWI images acquired using two different b-values. However, for the anisotropic diffusion, the diffusivity measured along one direction may differ from that measured along other directions. Therefore, a scalar diffusion coefficient does not describe the diffusivity of molecules and their surrounding adequately. To better describe the diffusion of molecules in a restricted medium, one needs to obtain the diffusion coefficient $\boldsymbol{D}$ as a tensor not a scalar. The diffusion tensor is a symmetric

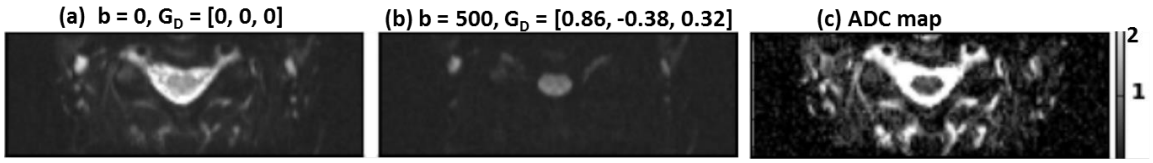

Figure 2.16: DW images with (a) b = 0 s/mm^2, (b) $b = 500$ s/mm^2, and (c) ADC map at C4 vertebra level.

second rank tensor. Therefore, at least six DWI images for six different directions and one b_0 ($b = 0$ s/mm^2) image must be acquired to calculate the full diffusion tensor. In order to make the diffusion tensor rotationally invariant, the diffusion tensor must be diagonalized. The diagonalized diffusion tensor is represented as

$$\mathbf{D} = \begin{bmatrix} \lambda_3 & 0 & 0 \\ 0 & \lambda_2 & 0 \\ 0 & 0 & \lambda_1 \end{bmatrix} \text{ and } \epsilon = \begin{bmatrix} \epsilon_3 \\ \epsilon_2 \\ \epsilon_1 \end{bmatrix} \quad [2.61]$$

where λ_1 and ϵ_1 are eigenvalue and eigenvector along the major axis and $\lambda_{2,3}$ and $\epsilon_{2,3}$ are eigenvalues and eigenvectors along the minor axes of the tensor ellipsoid. The degree of anisotropy of a medium is represented by a number called fractional anisotropy (FA). FA $\rightarrow 0$ represents a nearly isotropic medium and FA $\rightarrow 1$ represents a very highly restricted medium. FA is calculated from the diffusion tensor $\boldsymbol{D}$ as

$$FA = \frac{\sqrt{(\lambda_1 - \lambda_2)^2 + (\lambda_2 - \lambda_3)^2 + (\lambda_3 - \lambda_1)^2}}{\sqrt{2}\sqrt{\lambda_1^2 + \lambda_2^2 + \lambda_3^2}} \quad [2.62]$$

Other DTI metrics are axial or parallel diffusivity ($D_{\parallel}$), radial or perpendicular diffusivity ($D_{\perp}$), mean diffusivity (MD), and color coded orientation of principal eigenvector (EV).

$$\begin{cases} D_{\parallel} = \lambda_1 \\ D_{\perp} = (\lambda_2 + \lambda_3)/2 \\ MD = (\lambda_1 + \lambda_2 + \lambda_3)/3 \end{cases} \quad [2.63]$$

A DTI of a 4 mm thick slice of the human cervical spinal cord at C4-C5 vertebra level is shown in Figure 2.17.

2.4.6 Monte Carlo Simulation of Water Diffusion in White Matter

An analytical solution of the Bloch equation with the diffusion term (Bloch-Torrey equation) exists only for free diffusive motion where the displacement of the water molecules is a Gaussian distribution. When the diffusive motion is restricted, an exact solution of Bloch-Torrey equation is not possible. However, one can consider approximations such as the GPD and SPG to obtain the solution of Bloch-Torrey equation. Approximate solutions of Bloch-Torrey equation are possible only for simple and known geometries, such as an impermeable sphere (45) or cylinder (46). However, the structure of the neural tissue is very complex and an analytic solution of Bloch-Torrey equation even with GPD or SPG approximation is generally not possible. A commonly adopted method to study the diffusive motion in biological tissue is the Monte Carlo simulation (MCS)(47–49). In order to study water diffusion in white matter, and hence, the DW signal, MCSs have been performed with different white matter models; axons are modeled by square and hexagonal arrays of cylinders (50,51), prolate ellipsoids (52), hexagonal arrays of cylinders with myelin (49), and cylinders with radii distributed with gamma variate function (48). Although MCSs do not provide the same level of mathematical insight as analytic solutions do, MCSs are capable of investigating the diffusion phenomena in biological tissue for which analytical solutions do not exist (48).

In Monte-Carlo simulations of water diffusion, the position of each water molecule is updated in small time increments δt using a random walk method. The details

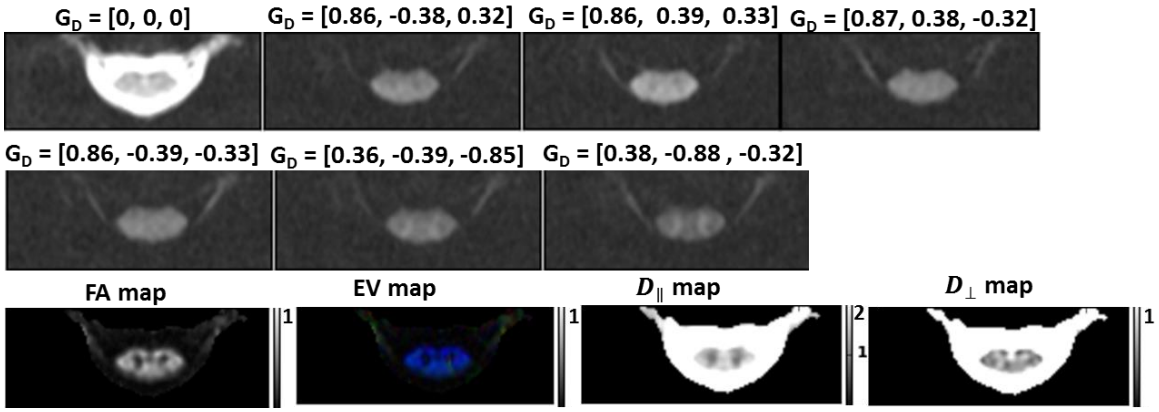

Figure 2.17: DTI of the human CSC. Six DW images with diffusion-weighted gradient applied in six different directions and one image without diffusion weighting. FA, EV, $D_{\parallel}$ and $D_{\perp}$ are derived from the DTI calculation. FA and EV are unit less and $D_{\parallel}$ and $D_{\perp}$ are in the unit of 10^{-3} mm^2/s.

of the assumptions and procedures incorporated in the MCS have been described in the literature (47–50,52–54). The MCS proceeds by initially distributing the molecules in the input geometry as described below:

2.4.6.1 Input geometry. The input geometry is a microscopic tissue structure in which diffusive motion of the molecules is being simulated. An image of a WM model or picture of a section of white matter provides the input geometry. The input geometry can be two-dimensional (2D), but three-dimensional diffusive motion can be simulated by assuming the diffusive motion perpendicular to the image plane (along axons) is free diffusion.

2.4.6.2 Initial distribution. At time t = 0, N molecules are uniformly distributed into intra-axonal (IA) and extra-axonal (EA) spaces of a voxel with dimension L × W × H. No water molecules are assigned into the myelin space because the water protons in myelin space do not contribute to the total signal because of their short T_2 for the

relatively long TE of the diffusion MRI experiments, particularly in whole body human MRI system. A three-dimensional diffusive motion is incorporated by updating the position of each molecule in every δt for a diffusion time T_{diff}.

2.4.6.3 Position update. The new position $\vec{r}'$ of a molecule is calculated to be $\vec{r}' = \vec{r} + \vec{l}$, where $\vec{r}$ represents the current position and $\vec{l}$ is a step vector with a constant length and random direction in 3D space. The constant step length is calculated as $r = \sqrt{6D\delta t}$ (48), where D is the free diffusion coefficient of the molecules. A random uniform direction is given by the spherical polar coordinates $\phi = 2\pi u$ and $\theta = \cos^{-1}(2v - 1)$, where u and v are uniformly distributed random numbers in the range [0, 1].

2.4.6.4 Exchange of molecules. A molecule is either transmitted or reflected at the boundary with a probability that is determined by the permeability P. The transmission probability for the molecules from one space to another ($p_{1\to2}$) is given by $P = (1/4)v_1 p_{1\to2}$, where $v_1 = \sqrt{(6D_1/\delta t)}$ is the velocity of the molecules in space 1 (47).

2.4.6.5 Local and voxel boundaries. A molecule diffuses freely along the fiber direction and possibly encounters a local boundary such as the membrane or myelin sheath perpendicular to the fibers. Xing et al. (54) studied the effect of a local boundary on the diffusive motion using four different position updating methods: elastic boundary reflection, nonelastic boundary reflection, equal-step-length random leap, and nonelastic boundary reflection with Gaussian sampling. In their study, the authors concluded that when the step length is relatively small in comparison to the size of the restriction, the result of the four different methods are not noticeably different. Therefore, for simplicity

of the calculation, when a molecule crosses a local barrier and the permeability of the membrane (barrier) does not allow the molecule to cross it, the last position can be abandoned and a new position can be generated using the equal-step-length random leap method until it finds a position belonging to the same space. A periodic boundary (arrays of identical voxels) can be considered for the voxel boundary. When a molecule crosses the voxel boundary, then the molecule can be translated into the other side of the voxel with the same step length.

2.4.6.6 DW signal calculation. The successful position of each water molecule can be recorded for every 10−100 μs time step. The pulsed-gradient spin-echo (26) signal is then obtained by computing the phase accumulated by each molecule during the position–recording steps and summing the contributions from all water molecules as $S = \sum_k \exp(-i\gamma \sum_j \vec{r}_{jk}.\vec{G}_D^{\,j})\ \delta t$,where $\vec{r}_{jk}$ is the position vector of kth molecule in jth time step, $\vec{G}_D^{\,j}$ is the applied gradient in jth time step. Variation in the b-value is achieved by varying the gradient amplitude. The values of T_2 for IA and EA spaces are assumed to be the same. Thus, the effect of T_2 is ignored in the signal calculation.

2.5 Phased Array Coil

2.5.1 Historical Perspective

The first single-channel surface coils were available in the 1980s. The coil had to be moved for imaging of a large field-of-view (FOV) because the high SNR localized single-channel surface coils were limited to the dimension of the surface coil. The requirement of changing the position of the coil not only brought inconvenience to the patients and technologist involved in the imaging, but also took a long scan time because

the scan had to be repeated over and over. By early 1990, switchable arrays were invented. The switchable arrays solved the problem that the coil had to be moved from one region to another; however, most MR scanners at that time were not capable to receive the signals from the multiple channels simultaneously. As a result, only one of the multiple channels could be used at a time for imaging. In 1990, Roemer et al. (55) introduced a phased array coil composed of multiple surface coils. The phase array coil provides high SNR from a surface of a large FOV. Almost immediately, a phased array volume coil was introduced by Hayes et al. (56). The phased array volume coil provides high SNR at the surface as well as the center of the coil. Since then, phased array coils have been routinely used in clinical MRI.

2.5.2 Surface Coil

A radio frequency coil consists of one or more loops of a conductive wire and is used to detect the signal generated in MRI experiments. RF coils are broadly classified into three categories depending on their functionality: transmit-receive, receive-only, and transmit-only. When a receive-only coil is used for signal reception, either the body coil or separate transmit-only coil is used for the transmission of RF pulses.

A surface coil, shown in Figure 2.18, is simply a single loop placed directly over the region of interest and provides a very high sensitivity. A surface coil can be used as a receive-only or transmit-receive coil; however, it provides higher sensitivity during the receive mode and suffers from RF field inhomogeneity during the transmit mode. Therefore, a surface coil is often used as a receive-only coil with the body coil as a transmit coil.

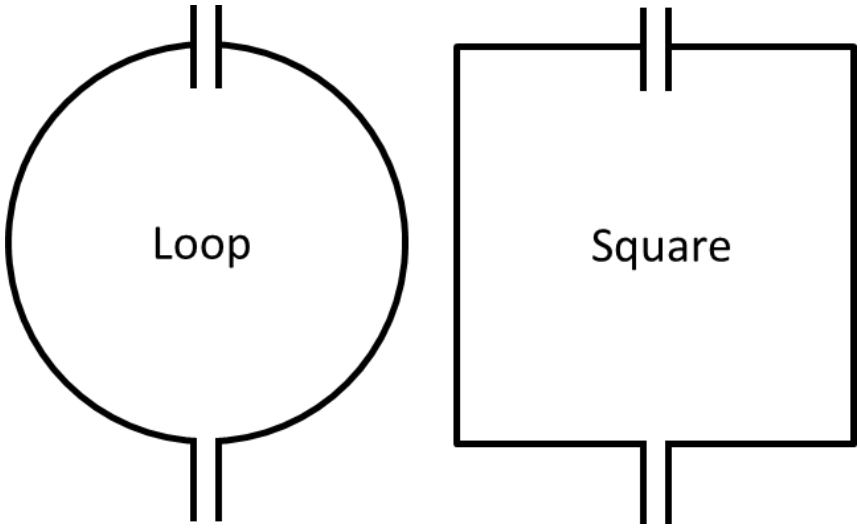

Figure 2.18: Schematic of surface coils: circular and square coils.

An equivalent circuit model of a surface coil is shown in Figure 2.19 (57). In this diagram, L_{loop} denotes the inductance of a loop and depends on the shape of the loop. L_{wire} denotes the self-inductance of a wire and depends on the diameter (width) and length of the wire. C_{loop} denotes the capacitance of the loop and is chosen in such a way that the loop resonates at a target frequency. V_{sig} represents a voltage induced (NMR signal) in a surface coil by the precessing transverse magnetization of a sample. V_{noise} represents thermally generated noise associated with the coil resistance R_{coil} (an AC resistance of a coil), and the sample resistance R_{sample}.

Noise (V_{noise}) is mainly generated in a surface coil because of the coil losses (resistive losses) and the sample losses. The coil losses are due to the skin effect which can be diminished by choosing a wire with bigger cross-section and smaller resistivity (58). The sample losses are caused by two different mechanisms: magnetic and dielectric losses. The magnetic losses are caused by the eddy current generated on a conductive

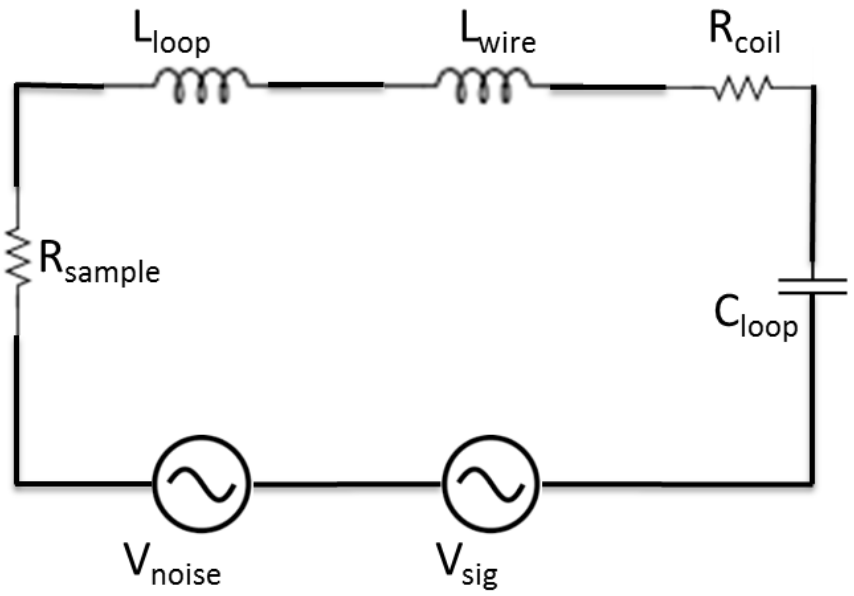

Figure 2.19: Equivalent circuit model of a surface coil.

sample due to a time varying current induced in the RF coil by the precessessing sample magnetization. The magnetic losses cannot be diminished. The dielectric losses are caused by currents induced in a conductive sample by the electric fields of the RF coils (59). The dielectric losses can be mitigated by minimizing the electric filed at the sample, for example, by balancing the RF coil and by distributing the tuning capacitors along the coil (60). The lines of the electric field generated around the coils with different numbers of capacitors are shown in Figure 2.20. The values of the capacitors in two- and four-capacitor loops are twice and four times larger than that of the single-capacitor loop. As a result, the voltage across each capacitor of the two- and four-capacitor loops is a half and quarter, respectively, of the voltage developed across the capacitor of the single-capacitor loop (61). The smaller the voltage developed across the capacitor is, the smaller the induced current in the conducting sample will be, and thus, the smaller the dielectric losses of the two- and four-capacitor loops will be compared to the single-capacitor loop.

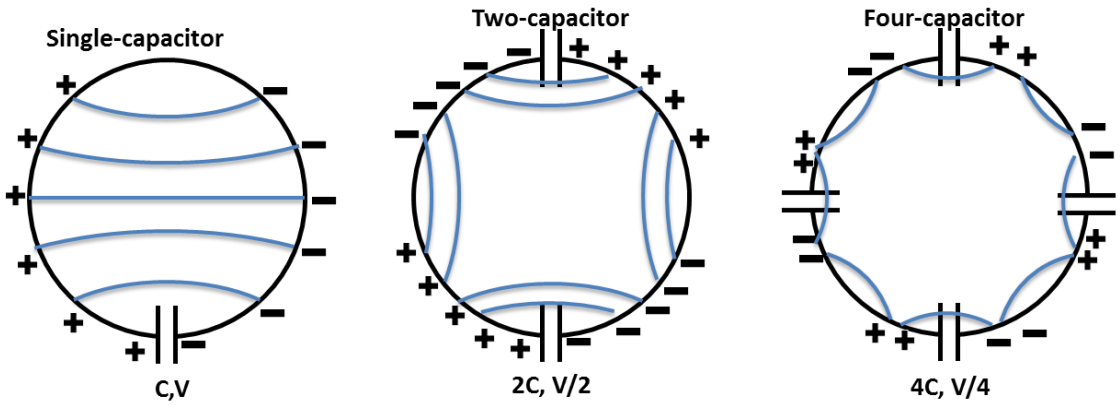

Figure 2.20: Distributions of the electric field lines (blue lines) for the single-, two-, and four-capacitor loops. Adapted from (61).

The merit of a surface coil is measured by calculating the signal-to-noise ratio (SNR) of the coil, which is defined as

$$SNR = \frac{V_{sig}}{V_{noise}} \quad [2.64]$$

According to the Principle of Reciprocity (62), the signal induced in a coil by the precessing magnetic moment of a sample is proportional to the imaginary transverse component of the magnetic field produced on the sample by the coil with unit DC current on it. An amplitude of the signal voltage, which is picked up by a coil from a voxel of volume V containing the magnetization per unit volume M_0, is given by (63)

$$V_{sig} = \omega_0 b_{1r} V M_0 \quad [2.65]$$

where ω_0 is the Larmor frequency of spin precession and b_{1r} is the transverse component of the rotating magnetic field produced at the voxel of volume V by the unit DC current in the coil.

According to the fluctuation-dissipation theorem, any dissipative medium generates thermally activated random fluctuation, which contributes to the noise. In MRI,

there are two dissipative elements, which are the major sources of the noise. One is the coil resistance R_{coil} due to conductive losses of the wire and another is the sample resistance R_{sample} due to magnetically induced eddy current losses in the sample (64). The coil resistance is dominant or comparable with the sample resistance at a lower static field B_0 ($\leq$ 0.3 T) whereas the sample resistance dominates the coil resistance at a higher field 1.5 T or greater (65). The sample resistance is six or more times larger than the coil resistance for whole-body imaging at 1.5 T (64). The noise voltage at the terminal of the coil due to the Johnson noise is

$$V_{noise} = \sqrt{4k_B T \Delta f R} \qquad [2.66]$$

where $R = R_{coil} + R_{sample} \approx R_{sample}$ at the field of 3 T, k_B =1.38× 10^{-23} J/K is Boltzmann's constant, T is the temperature of the sample and coil in Kelvin, and Δf is the observational bandwidth in Hz.

Substituting Eqs. [2.65] and [2.66], into the Eq. [2.64], the SNR expression becomes

$$SNR \propto \omega_0^2 b_{1r} / \sqrt{R_{coil} + R_{sample}} \qquad [2.67]$$

From the Eq. [2.67], it is clear that the SNR of a coil is directly proportional to the b_{1r} field and square of the Larmor frequency, and inversely to the square-root of the sum of the coil and sample resistances. The b_{1r} field can be maximized by putting the coil close to the sample, R_{coil} can be minimized by making the unloaded Q-factor high, and the R_{sample} can be minimized by choosing the size of a coil that matches the target FOV.

A quasistatic expression for the SNR of a lossless circular coil, a coil in which the sample resistance dominates the coil resistance, of radius R placed on a conductive half-space with conductivity σ is given by (66)

$$SNR = \frac{M_0 V\sqrt{3R}}{\sqrt{16k_B T\Delta f\sigma(R^2+z^2)^3}} \quad [2.68]$$

where z is a distance from the coil at which SNR is calculated. At a depth of z, a circular coil with the radius $R = z/\sqrt{5}$ yields the optimal SNR.

The coil SNR and losses discussed above are based on an ideal circuit model shown in Figure 2.19, and ignore various effects that appear in actual coil construction. Stray capacitances arise between nearby conductors, shown in Figure 2.21, shift the resonance frequency of the coil, and hence, degrade the performance of the coil. There will be additional resistive losses of a coil due to the effective series resistances of the passive components (capacitors, inductors, and diodes) and the connections such as solder joints (57). The effective resistance of a wire may also be increased at high frequencies by running a parallel wire in its close proximity, also known as proximity effect. The proximity effect arises when parallel wires induce eddy current in each other. The stray capacitances and the proximity effect may be minimized using proper orientation of wires and cables. The resistive losses in a coil may be mitigated by making the conduction path shorter and by avoiding unnecessary passive components and joints.

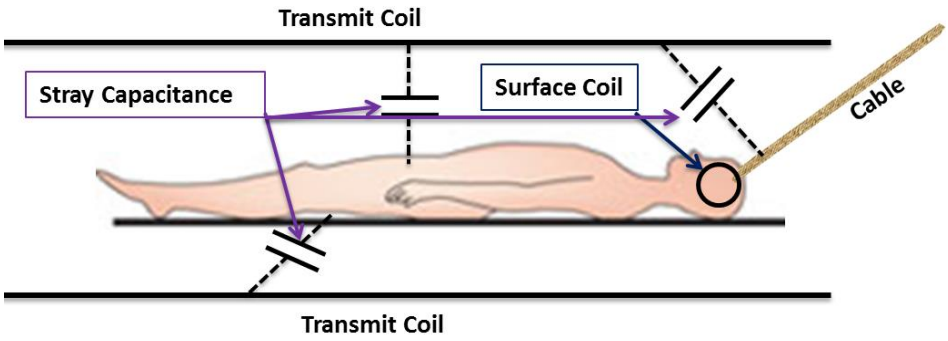

Figure 2.21: Stray capacitances between a human body and a conductor inside the MRI scanner.

Furthermore, the performance (or SNR) of a coil depends on the various other factors such as wire gauge, capacitive splits, Q-factor, and coil size. These factors are discussed in more detail below.

2.5.2.1 Wire gauge. A thinner wire has a higher AC resistance (R_{coil}) than a thicker wire because of its smaller cross-section area, which results in higher signal loss. Conversely, a thicker wire is more difficult to form into a desired shape, and could introduce additional proximity effects. Therefore, wire gauge should be chosen carefully with a reasonable tradeoff between low AC resistance and ease of manufacturing. Wire with $14-18$ gauges is considered a good compromise.

2.5.2.2 Capacitive splits. Having too few capacitive splits (breakpoint) effectively increases the length of the conductor (wire) between the breakpoints. When the length of the conductor between the breakpoints reaches approximately $\lambda/10$, transmission line effects become significant. Furthermore, the large electric field penetrates a larger sample volume, which results in increased dielectric losses. The transmission line effects and dielectric losses can be diminished by having many breakpoints. However, having too many break points effectively increases the coil resistance (R_{coil}) by increasing the resistance of the solder joints and the series resistance of the capacitor itself, causing higher resistive losses and a lower Q of the circuit (67).

2.5.2.3 Q-factor. The quality factor Q is used in many areas of physics and engineering to measure the energy storage efficiency of a resonant circuit. It also refers to the speed with which an oscillation of a resonant circuit dies out. For example, a bell with a very high Q rings for very long after being struck. The Q-factor is the ratio of energy stored in a circuit to the energy dissipated per cycle. Mathematically, Q is defined as

$$Q = \frac{2\pi \times maximum\ energy\ stored\ in\ a\ circuit}{energy\ dissipated\ per\ cycle} = \frac{\omega_0 \mathrm{L}}{R_{coil}} \quad [2.69]$$

where ω_0 is the resonance frequency and L ($L_{coil} + L_{wire}$) is the inductor of the coil. Alternatively, the Q-factor is defined as the ratio of the center frequency to the full width half maxima ($\Delta\omega$) of a resonator

$$Q = \frac{f_0}{\Delta f} = \frac{\omega_0}{\Delta\omega} \quad [2.70]$$

In MRI, a higher value of Q describes a surface coil with a smaller coil resistance which resonates with a large amplitude over a small bandwidth. Conversely, a coil with low Q resonates with small amplitude over a large range of frequencies. The Q value of a surface coil will be different when it is measured with or without a sample or load. An empty coil (unloaded) has relatively higher Q (Q_{unload}) as R_{coil} is only the resistance acting in the circuit. In contrast, a loaded coil has relatively lower Q (Q_{load}) because the various fields of the coil interact with the conducting sample which increase the resistance of the circuit (R_{sample} plus R_{coil}). Mathematically, Q_{unload} and Q_{load} are expressed as

$$Q_{unload} = \frac{\omega_0 L}{\mathrm{R_{coil}}} \quad [2.71]$$

$$Q_{load} = \frac{\omega_0 L}{\mathrm{R_{coil}} + R_{sample}} \quad [2.72]$$

The sensitivity of a surface coil is given by the ratio of Q_{unload} to Q_{load}

$$sensitivity = \frac{Q_{unload}}{\mathrm{Q_{load}}} = \frac{\mathrm{R_{coil}} + R_{sample}}{\mathrm{R_{coil}}} \quad [2.73]$$

For a reasonable sensitivity of a surface coil, the Q_{unload}/Q_{load} ratio should be 5 or higher.

2.5.2.4 Coil size. The sensitivity of a surface coil decreases with increasing depth z from the coil plane. The SNR of a circular coil with 6 cm radius calculated with respect to the distance from the coil using a quasistatic expression (Eq. [2.68]) is shown in Figure 2.22. Thus, a surface coil provides the best SNR at the surface as SNR decreases with increasing distance from the coil.

To optimize SNR at a particular depth one needs to consider the dependence of SNR at such depth as a function of coil radius. For different depths of interest, there will be different sizes of coils that offer the optimal SNR. Based on the quasistatic expression Eq. [2.68], a lossless circular coil of radius $z/\sqrt{5}$ yields the optimal SNR at a depth z, as shown in Figure 2.23. For example, to get optimal SNR at a depth of 6 cm, a circular coil of radius 2.68 cm is best.

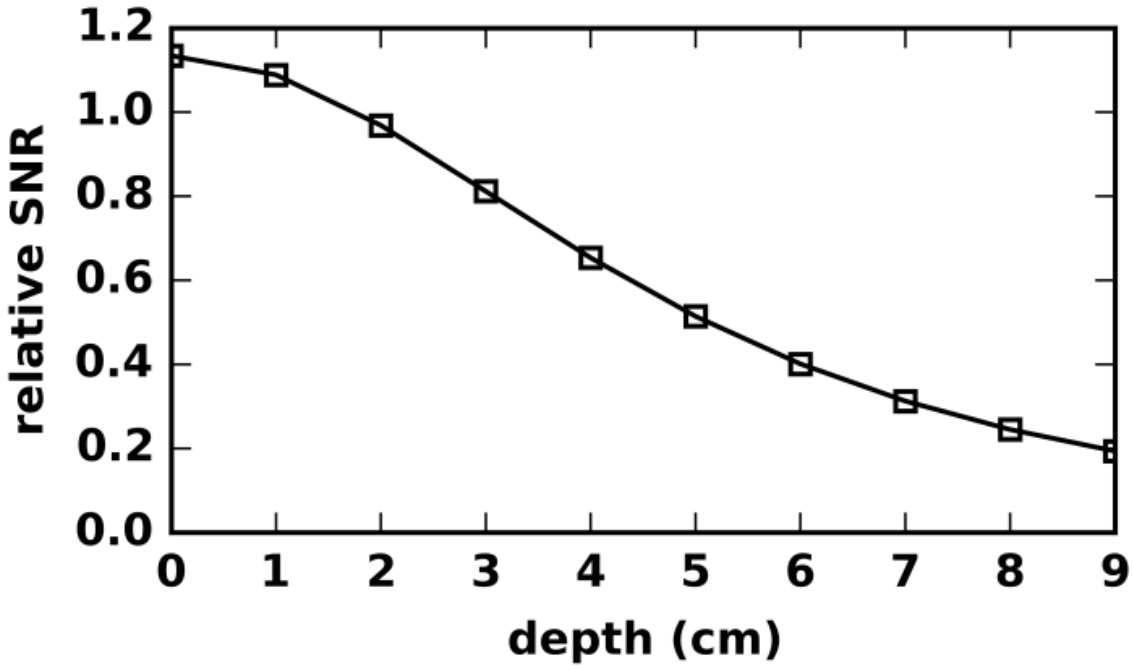

Figure 2.22: Relative SNR of a circular coil of radius 6 cm calculated at various depths from the surface of the coil.

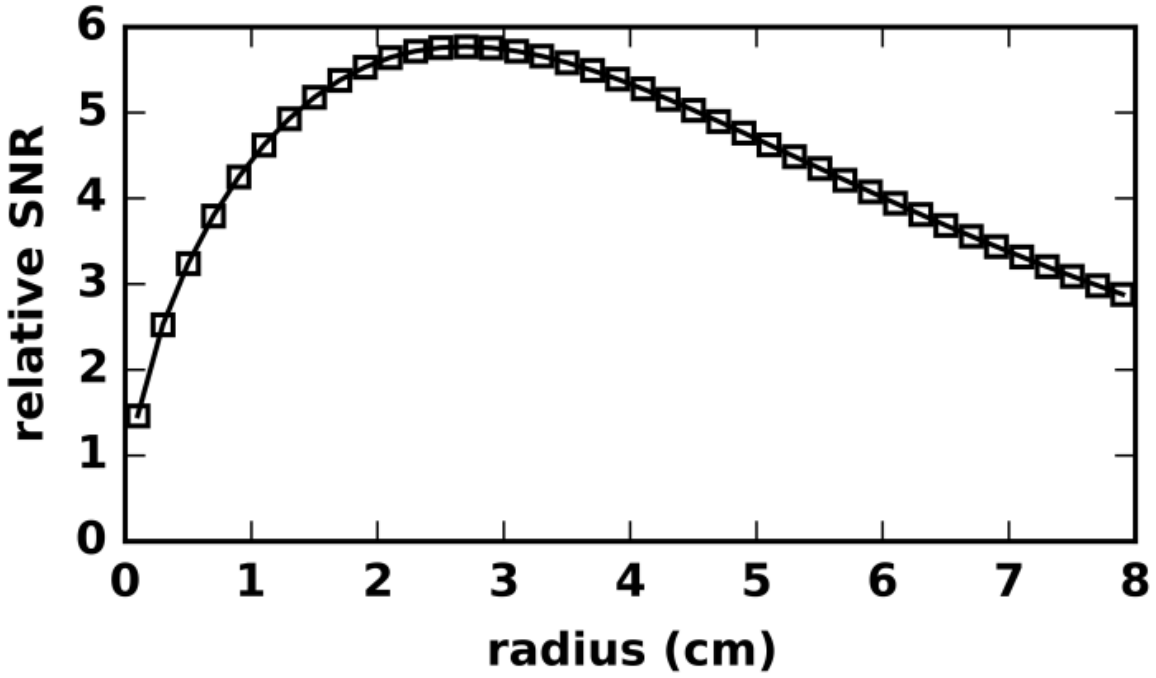

Figure 2.23: Relative SNR of circular coils of different radii at a depth of 6 cm from the surface of the coils. A circular coil of radius 2.68 cm offers the optimal SNR at a depth of 6 cm from the surface of the coil.

The quasistatic expression was derived based on the assumption that coils are lossless. In the case of a small surface coil, the assumption that the coil is lossless may not be valid because the coil losses are generally not negligible compared to the sample losses. Kumar et al. (57) calculated the sizes of the lossy circular coils, which yield optimal SNR at various depths, using the full-wave electromagnetic numerical method-of-moment (MoM) analysis. In the MoM analysis, a circular coil is considered a lossy conductor and the coil resistance is also included in the noise calculation. Three different kinds of resistances, the conductive resistance of the wire, the effective series resistance of the capacitors, and the RF resistance of the solder joints, are included in the MoM analysis. The sizes of the optimal coils calculated using the MoM and quasistatic

expression are listed in Table 2.3 (57). For a shallow depth (≤1 cm), the optimized radius of a lossy circular coil calculated using MoM differs significantly from that calculated for the lossless circular coils using the Bio-Savart's law (quasistatic expression). However, for a target depth of 2−10 cm, the optimized radii of the coils differ very minimal between two methods. Therefore, to some approximation, the quasistaic expression can be used to optimize the radius of a coil for a target depth of 2−10 cm (57), which is the depth of most tissue being imaged routinely in the human MRI.

2.5.3 Receive-Only Surface Coil Construction

A well-constructed receive-only surface coil should be tuned to the desired frequency, matched with a characteristic impedance of the coaxial cable, and detuned during the transmission of RF pulses using active and passive detuning circuits. A cable trap must also be placed between the coil and preamplifier to block the common mode currents. A preamplifier is used to amplify the signal picked up by a coil. A schematic diagram of a surface coil including all above circuitries is shown Figure 2.24. Details of each circuitry are described below.

Table 2.3: Optimal coil radii calculated using two different methods quasistatic and MoM for 3 T.

Target depth in cm	Optimal coil radii in cm (Quasistaic expression)	Optimal coil radii in cm (MoM)
0.5	0.2	0.5
1.0	0.4	0.8
2.0	0.9	1.4
5.0	2.2	2.3
7.5	3.4	3.4
10.0	4.5	4.8
15.0	6.7	7.8

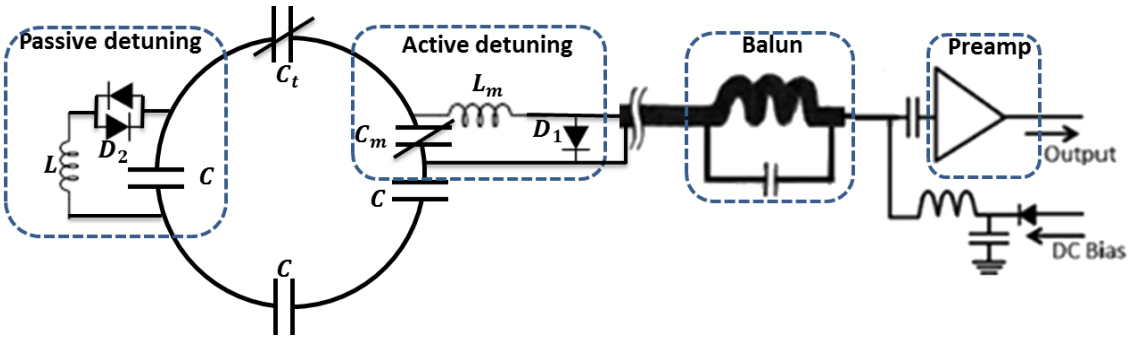

Figure 2.24: A complete circuit schematic of a surface coil with 50 Ohm preamplifier. For a low input impedance preamplifier, a phase shifter (not shown in the figure) should be placed between the balun and the preamplifier to make the effective electric distance between coil and preamplifier a half-wave.

2.5.3.1 Tuning and matching. For the optimal performance of a surface coil, a coil should be tuned (resonate) at the desired frequency (128 MHz at 3 T) and matched to the characteristic impedance of the coaxial cable (usually 50 Ω). Tuning of a coil is carried out by adjusting a variable tuning capacitor C_t, and matching is performed by a adjusting a variable matching capacitor C_m and matching inductor L_m (see Figure 2.24). A good matching of a coil is obtained by adjusting C_m and L_m in such a way that the reflection parameter ($S11$), which is measured using a network analyzer, is below -20 dB as shown in Figure 2.25.

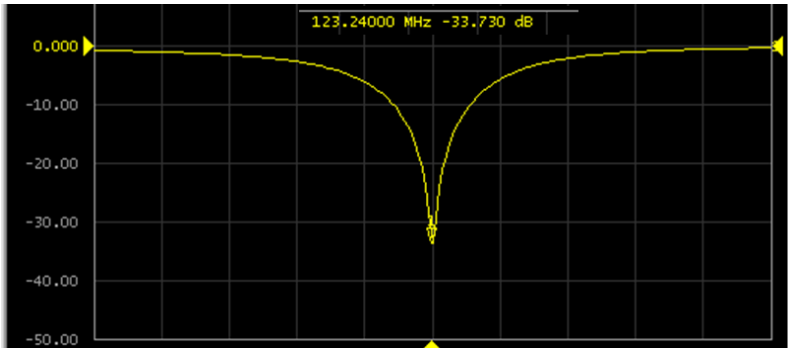

Figure 2.25: S11 curve during coil tuning and matching.

2.5.3.2 Active and passive detuning. The receive-only coil should be detuned or deactivated during the transmission of RF pulses, otherwise, the coil picks up high RF power, which could cause several adverse effects such as local burning of patient's skin adjacent to the coil, damaging the preamplifier, and increasing the B_1 field inhomogeneity. The parallel LC circuit shown in Figure 2.26 is used for both active and passive detuning. The frequency response of a parallel LC circuit to the impedance and current is shown in Figure 2.27. At the resonance frequency, a parallel LC-circuit ideally poses infinite input impedance and the circuit is equivalent to an open-circuit.

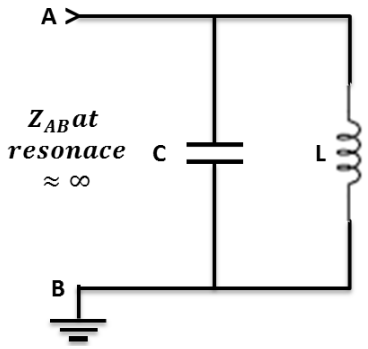

Figure 2.26: A parallel LC circuit. At resonance, the circuit is equivalent to open circuit between terminals A and B.

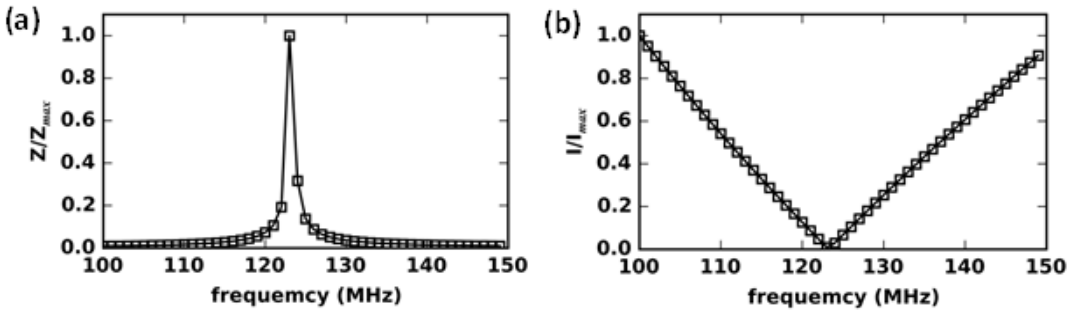

Figure 2.27: Frequency response curves for (a) impedance and (b) current of a parallel LC circuit (C= 20 pF and L = 83.4 nH) at a frequency range of 100-150 MHz.

The active and passive detuning circuitries embedded into a surface coil are shown in Figure 2.28. A parallel LC circuit made of an inductor L and a capacitor C (inside blue-dashed line) resonates at a desired frequency (128 MHz at 3 T). The active trap will be activated by forward-biasing the PIN diode D_1 supplying a 100 mA DC current from the MRI system. During the RF transmission, the diode D_1 is shorted by supplying a 100 mA DC current and L and C of the active trap formed a parallel LC circuit. A parallel LC circuit provides infinite impedance at L and C junctions, which deactivates the coil. In contrast, the passive trap, which is composed of crossed-switching diodes (D_2), will be activated by high power AC current. The passive trap is a supplement to the active trap. When an active trap fails to deactivate a coil during the RF transmission, the coil picks up very high power current, which shorts the crossed-diode pair D_2. Then, the L and C of the passive trap form a parallel LC circuit, which creates a virtual open circuit at the L and C junctions. During the NMR signal reception, the PIN diode D_1 is reverse-biased with -30 V and the NMR signal is not large enough to short the diode D_2. Both diodes D_1 and D_2 act as an open circuit at the time of the signal reception, thus, no parallel LC circuit is formed. The coil remains tuned at the desired frequency and picks up the NMR signal.

Using a network analyzer, the performance of the active and passive traps can be evaluated on the bench by measuring the decrease in the transmission parameter ($S21$) before and after a 100 mA DC current supplied to a coil. Typical $S21$ curves before and after a 100 mA DC current supplied to a coil are shown in Figure 2.29. For the acceptable performance of the traps, the $S21$ parameter should decrease approximately by $25-30$ dB when the DC current is supplied to the coil.

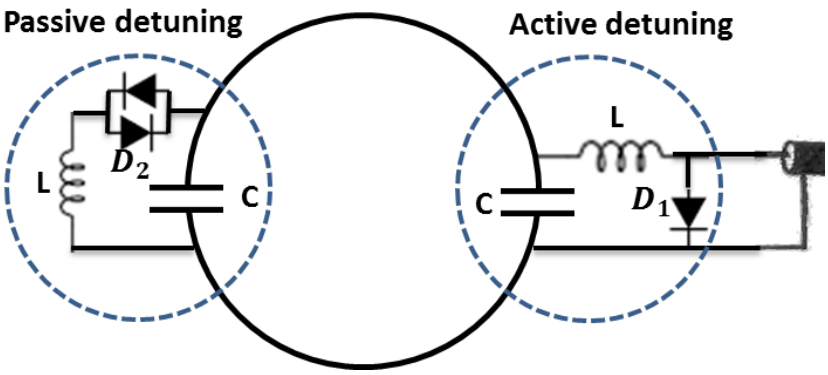

Figure 2.28: A schematic of a surface coil with active and passive detuning circuits (enclosed in the blue-dashed line).

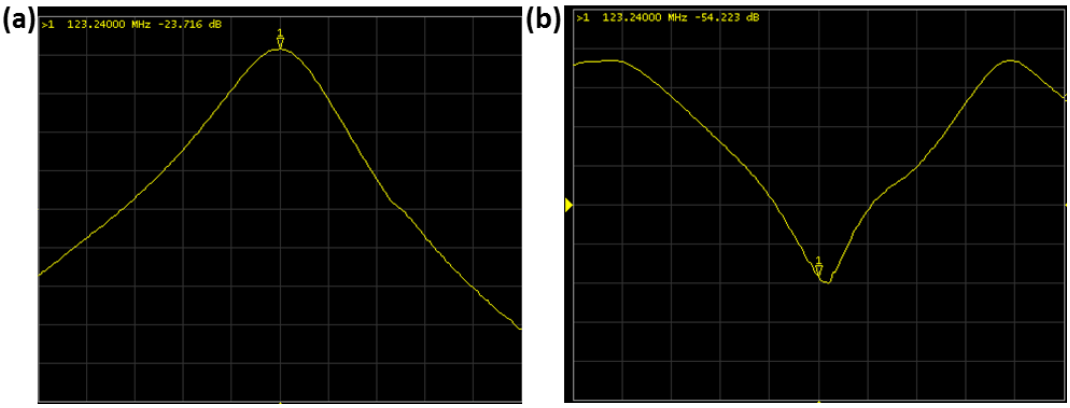

Figure 2.29: $S21$ measurements (a) before and (b) after a 100 mA DC current supplied to a coil during active/passive detuning. The $S21$ parameter is decreased by 30 dB at the resonance frequency during the detuning.

2.5.3.3 Cable trap (balun). A coaxial cable generally carries two types of currents: differential and common modes. A differential mode has exactly equal and opposite current in the central and shield conductors of a coaxial cable. Currents in differential mode neither radiate energy outside nor respond to the outside signals. Conversely, common mode currents flowing along the shield of the coaxial cable are not matched by exactly opposite and equal magnitude currents flowing along the central line.

The current in a common mode generates unnecessary coupling and heating of the RF coils and cables (68). A balun provides a large amount of impedance to the common mode current without affecting the differential mode current. An RF coil without a balun has the higher coil losses, and hence, the lower SNR.

Generally, a balun (cable trap) is constructed using an inductor (L) made of the cable shield and a capacitor (C) of appropriate capacitance in a parallel combination as shown in Figure 2.30, so that the parallel LC circuit resonates at the desired frequency. Since a parallel LC circuit provides infinite input impedance at the resonance frequency, the cable trap blocks the common mode currents, which flow through the outer cable shield, without affecting the differential mode currents.

2.5.3.4 Preamplifier. A preamplifier is one of the important devices from the viewpoint of SNR of a surface coil. Generally, the signal induced and the noise generated in a coil are of the order of a few mV and μV, respectively, thus, the intrinsic SNR of a coil measured at the coil output terminals is about 1000. However, as the signal travels from the coil to the receiver, noise is continuously added along the pathway, resulting in poorer SNR. Therefore, a low noise high gain preamplifier is placed next to the coil, which amplifies both the intrinsic signal and noise of the coil. A simple model of the preamplifier is depicted in Figure 2.31. Preamplifiers have a typical gain of 20−30 dB, i.e., a preampfier amplifies a signal 100-1000 times in power (10-31 times in voltage). However, a preamplifier is a power device, which adds an extra noise at the time of amplification. The quality of a preamplifier with gain G is described by the noise figure (NF) and is defined as (69)

$$NF = \frac{SNR_{input}}{SNR_{output}} = \frac{S_i/N_i}{S_o/N_o} = 10\log_{10}(1 + \frac{N_p}{GN_i}) \qquad [2.74]$$

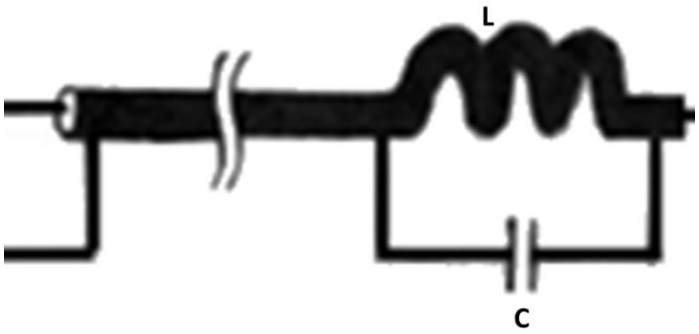

Figure 2.30: A cable trap (balun) constructed using a parallel combination of a cable shield inductor and a capacitor.

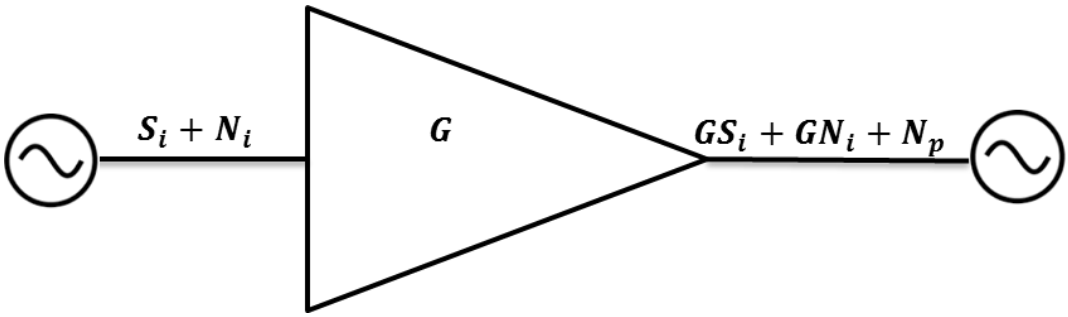

Figure 2.31: Depiction of a preamplifier with gain G. S_i and N_i denote the input signal and noise, respectively, and N_p denotes the noise generated inside the preamplifier.

where SNR_{input} and SNR_{output} represent the SNR in terms of the power at an input and output terminals of a preamplifier. S_i, S_o, N_i, $N_o = GN_i + N_P$, and N_p denote, respectively, input signal, output signal, input noise, output noise, and noise generated by the preamplifier. Eq. [2.74] describes that preamplifiers with the same NF but different gain will have the same N_p/G ratio, which results in the same output SNR, $SNR_{out} = S_i/(N_i + (N_p/G))$, of the preamplifier. However, as the signal travels through the cable and other RF components, noise is continuously added up, thus, a preamplifier with higher gain is desired.

2.5.4 Phased Array Coil

Generally, a surface coil is optimized for a target depth, for instance, a circular coil of radius 2.68 cm has the optimal SNR for a depth of 6 cm. For a shallower depth, a smaller surface coil yields the optimal SNR. In contrast, a bigger coil is required to obtain the optimal SNR from a deeper depth. Therefore, the optimal size of a surface coil depends on the target depth which necessarily limits the imaging FOV to a smaller region (70). In most cases, the imaging FOV of a surface coil does not cover the anatomy of interest, thus, a bigger imaging FOV is required, which can be achieved using the multiple surface coils. An RF coil composed of multiple surface coils is called a "phased array". The term 'phased array' has been derived from antenna theory. Phased array coils offer high SNR images over a large FOV and have advantages over volume coils at least in two ways: first, the SNR and quality of the images can be improved; second, imaging time can be reduced significantly (71). A schematic of a 7-channel phased array coil composed of seven circular coils is shown in Figure 2.32. Each element of an array is equipped with all the necessary RF components such as a tuning, matching, active and passive detuning, balun, and preamplifiers which were discussed in the previous sub-section. Each element receives signal independently and simultaneously. A composite image is formed by combining the signals received from all elements using the square root of the sum-of-squares method (55).

In a phased array coil design, an extension of a FOV is achieved by using multiple surface coils. However, it is also desirable to maintain each surface coils' optimal SNR, which is generally reduced by mutual interactions with other surface coils. A major challenge in an array design is to eliminate the interactions between neighboring

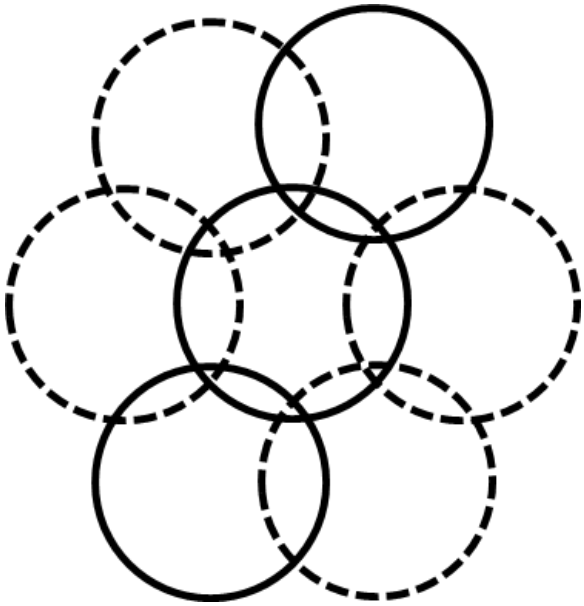

Figure 2.32: Schematic of a 7-channel phased array coil.

elements. The mutual coupling between two elements has been modeled and described elsewhere (67). A model of a two elements system is depicted in Figure 2.33. $R_{1(2)}$, $L_{1(2)}$, and $C_{1(2)}$ denote resistance, self-inductance, and capacitance of the coil 1(2), respectively. V_{signal} represents a signal voltage induced in coil 1 and V_{out} denotes an output voltage of the coil 1. The mutual inductance between coil 1 and coil 2 is represented by M_{12}. I_1 is an AC current induced in coil 1 due to precessing magnetization and I_2 is an AC current induced in coil 2 due to current I_1 flowing in coil 1, i.e., the mutual induction (M_{12}) between two elements. The output voltage of coil 1 can be expressed as (67)

$$V_{out} = V_{signal} + \left(R_1 + i\left(\omega L_1 - \frac{1}{\omega C_1}\right)\right) I_1 + i\omega M_{12} I_2 \qquad [2.75]$$

The second and third terms in Eq. [2.75] are the noise generated in coil 1 associated with the currents I_1 and I_2, respectively. At resonance, the imaginary part of the second term

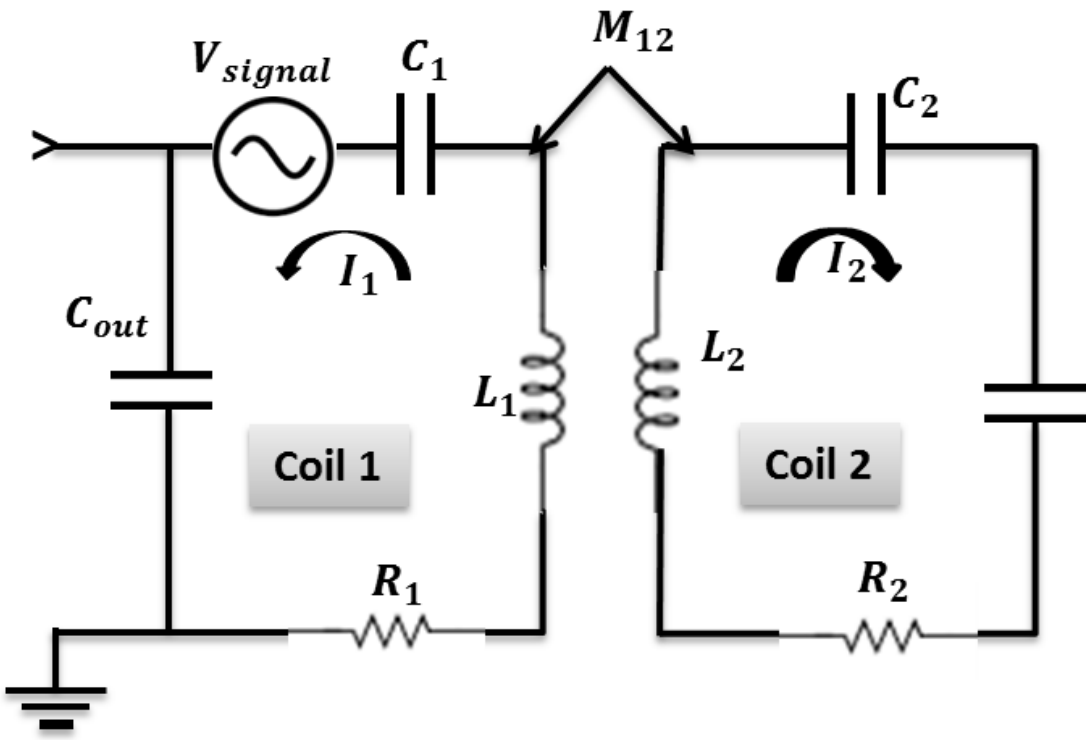

Figure 2.33: Mutual induction between two elements in an array (67).

vanishes; leaving only the unavoidable resistive term, thus, only the resistive term contributes to the noise. The third term arises due to the mutual induction M_{12} between coils 1 and 2, and vanishes in two cases: either $M_{12} = 0$ or $I_2 = 0$.

$M_{12} = 0$ corresponds to the case where the mutual induction between coil 1 and coil 2 is zero. This represents a situation in which two coils are overlapped in such a way that the magnetic flux linkage in one coil due to another coil is completely nullified. The mutual induction between two elements will be zero when circular elements are separated by about 0.75 × diameter, or square elements are separated by about 0.90 × diameter (55). The coupling between two elements can also be eliminated ($M_{12} = 0$) by choosing an appropriate geometry of the elements, for example, a butterfly element and a co-axial

circular element, shown in Figure 2.34, poses a negligible mutual induction between them because the magnetic fields produced by them are orthogonal to each other (72).

$I_2 = 0$ corresponds to the case where the current flowing in coil 2 due to the AC current in coil 1 is zero. This condition is achieved using a preamplifier decoupling technique. The details of this technique are described elsewhere (55,67). A circuitry for the preamplifier decoupling technique is depicted in Figure 2.35. The matching inductor (L_m) and capacitor (C_M) are used for the decoupling circuitry. When the input impedance of the preamplifier is very low, ideally 0, the matching inductor L_m and capacitor C_M form a parallel LC circuit. The values of L_m and C_M are chosen in such a way that the parallel LC circuit formed by L_m and C_M resonates at a target frequency, providing a high impedance (open circuit in the theoretical limit) to a target frequency. As a result, there is no current flow, i.e., I_2 =0, in coil 2.

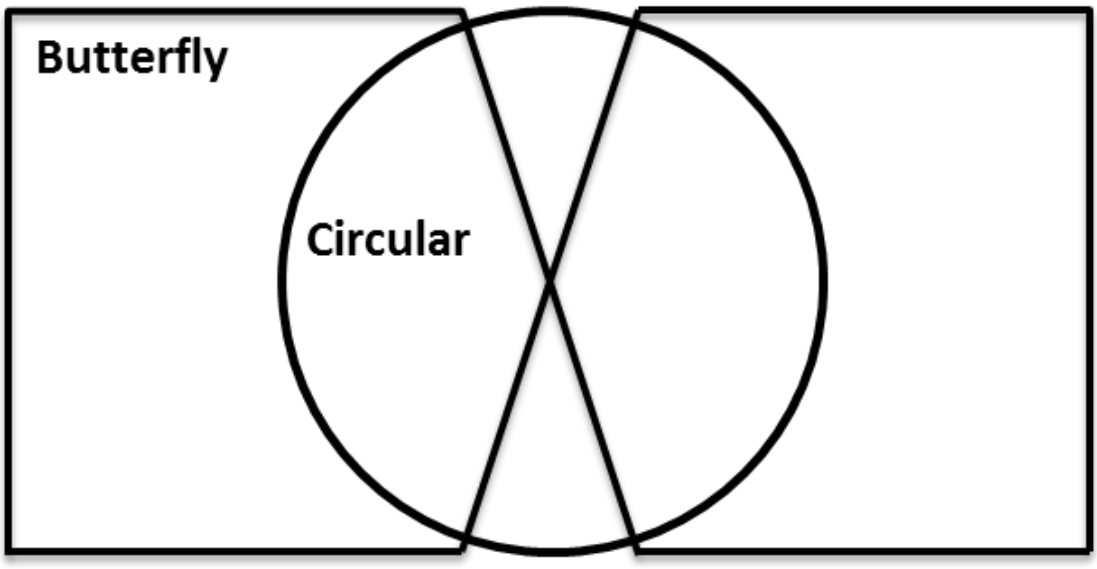

Figure 2.34: A co-axial pair of butterfly-circular elements. The mutual induction between two elements is negligible because of the orthogonal nature of the magnetic fields produced by them.

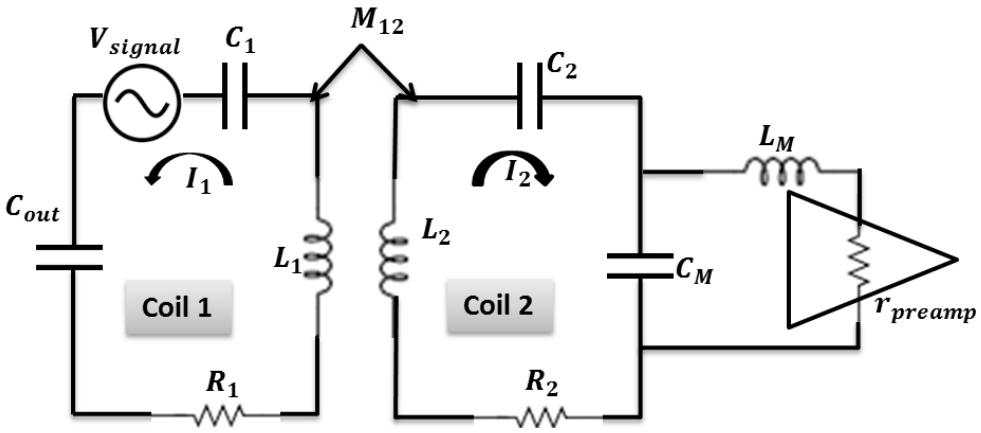

Figure 2.35: A circuitry of preamplifier decoupling technique. A low input impedance ($r_{preamp} < 5\ \Omega$) preamplifier is connected to the coil 2.

The performance of preamplifier decoupling can be evaluated by measuring the decrease in $S21$ parameter before and after the low input impedance preamplifier inserted into the preamplifier board. Usually, the preamplifier decoupling provides $20-25$ dB decrease in the $S21$ parameter when it is measured with the preamplifier inserted into the board compared to that measured without the preamplifier inserted into the board. Typical $S21$ curves with and without preamplifier inserted into the board are shown in Figure 2.36.

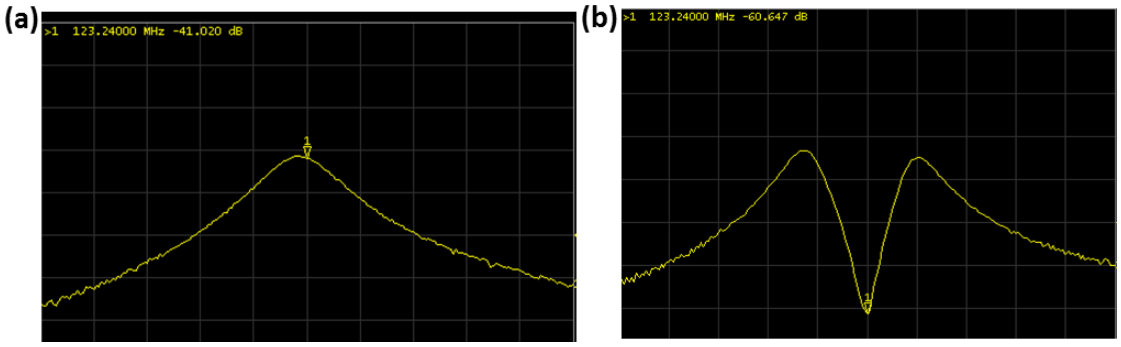

Figure 2.36: $S21$ curves of an isolated element (a) without preamplifier decoupling and (b) with preamplifier decoupling. The difference of $S21$ before and after the preamplifier decoupling is found to be -20 dB.

If a nonzero mutual induction between two elements exists (either $M_{12} \neq 0$ or $I_2 \neq 0$), the resonance peak ($S11$ curve) will be splited and distorted, which degrades the performance of the elements, and hence, the phased array coil composed of them. Effects on the $S11$ curve due to two elements keeping close to each other are shown in Figure 2.37. The resonance peak starts to split when two elements are not overlapped critically. At a critical overlapping, for example, circular elements are separated by about 0.75 × diameter, or square elements are separated by about 0.90 × diameter (55), the mutual induction between two elements is zero, and hence, the single resonance peak is reestablished.

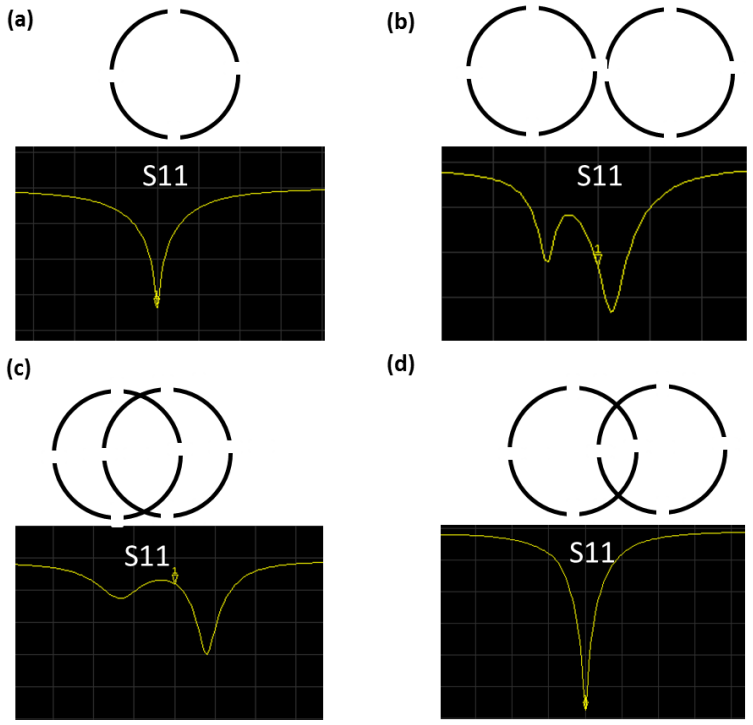

Figure 2.37: Effects of the mutual induction between elements on the resonance peak (S11). (a) Individual element, (b) two elements close to each other (not enough overlapped), (c) elements are overlapped too much, and (d) elements overlapped appropriately.

A complete circuit schematic for an element of a phased array is depicted in Figure 2.38. A pi-network phase shifter is added into the circuit to make an electrical distance half-wave from the coil to the preamplifier. A co-axial cable of length equal to half-wave may also be equivalently used between the coil and the preamplifier instead of the phase shifter. The half-wave electric length between coil and preamplifier effectively transfers the low input impedance of the preamplifier across the diode D_1 of the detuning trap.

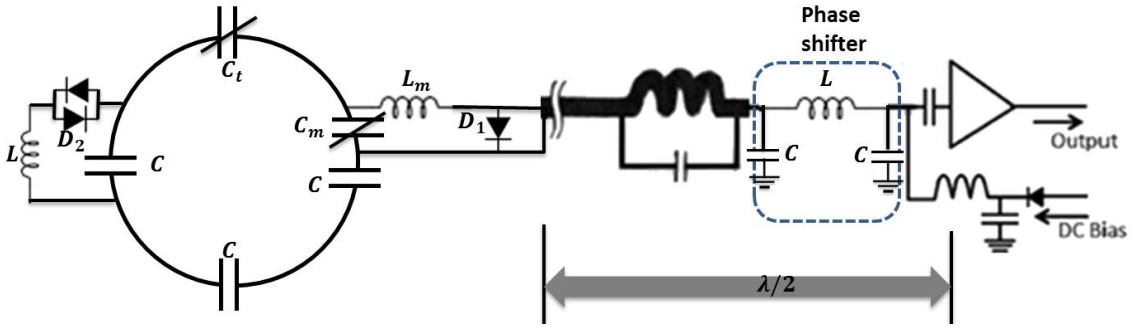

Figure 2.38: Circuit schematic of an element of a phased array. A pi-network phase shifter is incorporated into the circuit to make an electric distance half-wave ($\lambda/2$) from coil to the preamplifier.

CHAPTER 3

CHARACTERIZATION OF SPINAL CORD WHITE MATTER BY SUPPRESSING SIGNAL FROM HINDERED SPACE: A MONTE CARLO SIMULATION AND AN EX VIVO ULTRAHIGH-B DIFFUSION-WEIGHTED IMAGING STUDY

This chapter is adapted from a paper entitled "Characterization of spinal cord white matter by suppressing signal from hindered space: a Monte Carlo simulation and an ex vivo ultrahigh-b diffusion-weighted imaging study "authored by Nabraj Sapkota, Sook Yoon, Bijaya Thapa, YouJung Lee, Erica F. Bisson, Beth M. Bowman, Scott C. Miller, Lubdha M. Shah, John W. Rose, and Eun-Kee Jeong. The paper has been published online in the Journal of Magnetic Resonance (JMR) in September 2016.

3.1 Abstract

Signal measured from white matter in diffusion-weighted imaging is difficult to interpret because of the heterogeneous structure of white matter. Characterization of the white matter will be straightforward if the signal contributed from the hindered space is suppressed and purely restricted signal is analyzed. In this study, a Monte Carlo simulation (MCS) of water diffusion in white matter was performed to understand the behavior of the diffusion-weighted signal in white matter. The signal originating from the

hindered space of an excised pig cervical spinal cord white matter was suppressed using the ultrahigh-b radial diffusion-weighted imaging. A light microscopy image of a section of white matter was obtained from an excised pig cervical spinal cord for the MCS. The radial diffusion-weighted signals originating from each of the intra-axonal, extra-axonal, and total spaces were studied using the MCS. The MCS predicted that the radial diffusion-weighted signal remains almost constant in the intra-axonal space and decreases gradually to about 2% of its initial value in the extra-axonal space when the b-value is increased to 30,000 s/mm^2. The MCS also revealed that the diffusion-weighted signal for a b-value greater than 20,000 s/mm2 is mostly from the intra-axonal space. The decaying behavior of the signal-b curve obtained from ultrahigh-b diffusion-weighted imaging (b_{max} ~ 30,000 s/mm^2) of excised pig cord was very similar to the decaying behavior of the total signal-b curve synthesized in the MCS. A monoexponential plus constant fitting of the signal-b curve obtained from a white matter pixel estimated the values of constant fraction and apparent diffusion coefficient of decaying fraction as 0.32 $\pm$0.05 and (0.16 $\pm$0.01) $\times$ 10^{-3} mm^2/s, respectively, which agreed well with the results of the MCS. The signal measured in the ultrahigh-b region (b > 20,000 s/mm^2) is mostly from the restricted (intra-axonal) space. Integrity and intactness of the axons can be evaluated by assessing the remaining signal in the ultrahigh-b region.

3.2 Introduction

An advanced magnetic resonance imaging (MRI) technique, high-b diffusion-weighted imaging (DWI), has been evolving for neural tissue imaging because it provides enhanced contrast between white matter (WM) and gray matter (GM) (73), and higher

sensitivity in gliomas grading (74). The high-b DWI may also be beneficial in detecting additional subtle WM lesions (75,76). Restricted compartment in WM can be estimated using ultrahigh-b radial DWI (UHB-rDWI, the DWI with the applied field gradient perpendicular to the fibers), which can be a biomarker for the characterization of the WM (77,78). An understanding of the relationship between the behavior of diffusion-weighted (DW) signal with respect to b-value and fiber microstructure may elucidate the physiologic processes underlying both the loss and recovery of neural function in disease states and with therapy (79).

Recently, various DWI methods such as q-space imaging originally introduced by Cory and Garroway (35) and Callaghan et al. (36), AxCaliber (37), and NODDI (38) have been proposed to characterize neural tissue. However, current clinical MRI systems have been facing difficulties to meet the requirements and assumptions proposed in the models (37,38). Fitting of the signal versus b (signal-b) curve obtained from UHB-rDWI is the conventional DWI method that has been considered a potential technique to characterize neural tissues (49,52,77,78,80–84); however, because of the complex structure of the WM, its characterization is not straightforward.

DW signal measured in the WM is mostly dominated from the intra-axonal (IA) and extra-axonal (EA) spaces. The contribution of myelin water to the DW signal is negligible because the water molecules in myelin have short T_2 (~10 ms) for a relatively long echo-time (TE ~ 100 ms) (85–87). The diffusive motion perpendicular to the fibers is restricted (diffusive motion is confined inside the boundary) in the IA space and hindered (molecules can diffusive around but the diffusive motion deviates from the Gaussian diffusion due to the presence of hindrance on the path) in the EA space (88).

Because axons are almost cylindrical in structure, the restricted diffusion inside the axons may be modeled with the diffusion inside an impermeable cylinder. The analytical expressions for the DW signal attenuation in an impermeable cylinder have previously been reported in (46,89–91); however, because of the complicated structure of the WM, including a restricted space formed by the heterogeneous distribution of axons and a hindered space with indefinite hindrance provided by the axons and other microorganelles, an analytical solution of the diffusion equation in WM is not possible.

The signal attenuation in the DWI can be expressed using the cumulant expansion (92,93), which is a Taylor expansion of the logarithm of the signal in power of b in the vicinity of b =0:

$$\ln(S_b/S_0) = -b.ADC + \frac{1}{6} K_{app}(b.ADC)^2 + \cdots, \quad [3.1]$$

where S_b and S_0 are the signal intensities with and without diffusion-weighting, respectively. ADC is the apparent diffusion coefficient and K_{app} is the apparent excess diffusional kurtosis. The parameter b is defined by the expression $b = (\gamma\delta G_D)^2 \times (\Delta - \delta/3)$, where γ is the gyromagnetic ratio, and δ, Δ, and G_D are, respectively, the duration, separation of leading edge, and amplitude of the DW gradient. For free diffusion, the distribution of the molecular displacement is Gaussian. The second and other higher terms of Eq. [3.1] vanish, and hence, the signal decays monoexponentially with the b-value as described in the Stejskal-Tanner equation (26). For restricted diffusion, such as the diffusion in WM, the distribution of the molecular displacement in not Gaussian, thus, the higher order terms of the cumulant expansion (Eq. [3.1]) should be considered to describe the signal behavior. However, the cumulant expansion has a finite radius of convergence at $b = 0$, therefore, it is useful only at intermediate and low b-values (92).

The DW signal decays nonmonoexponentially with the b-value in WM. A bi-exponential signal decay has been reported in rat brain ex vivo (80), rat brain in vivo (83), and human brain in vivo (77,81,82). A monoexponential with a constant baseline model has been used to fit the signal-b curve in human brain in vivo (49) and spinal cord in vivo (78,94). A tri-exponential model has been used as a better fitting model than bi-exponential in rat brain in vitro (95) and bovine optic nerve ex vivo (52). Multiexponential decay has been reported in rat brain in vivo (96) and rat brain and bovine optic nerve in vitro (97).

In this project, Monte Carlo simulation (MCS) was performed for the intensive study of the water diffusion in WM. The MCS provides the detailed behavior of the signal-b curve in the IA and EA spaces separately. Previous MCS studies of water diffusion in WM with different WM models (49,77,98) did not clearly explain the behavior of the signal-b curve in the ultrahigh-b (UHB) region and the potential application of the UHB-rDWI to characterize the WM. The focus of this work was to evaluate the DW signal originating from each of the IA, EA, and total spaces of WM using the MCS, and suppress the DW signal originating from the hindered space of the excised pig cervical spinal cord (CSC) WM using the diffusion parameters (diffusion duration, gradient amplitude, and diffusion time) guided by the MCS.

3.3 Methods

3.3.1 Light Microscopy Image of a Section of White Matter

The excised healthy pig cord (C2-C6) was fixed for 2 days in buffered formalin and then stored at 4°C in phosphate-buffered saline (PBS) for 8 months. Sections of the pig cord (C2-C3) that had been fixed for 2 days in buffered formalin were post-fixed in

osmium tetroxide, dehydrated in ascending concentrations of ethanol, and embedded in epoxy resin. Cross-sections of the cord were cut to 1 μm in thickness, mounted on glass slides, and stained with toluidine blue prior to observation by light microscopy. A light microscopy image (LMI) of a section of cervical spinal cord WM (CSC-WM) obtained with a light microscope (magnification ×60) is shown in Figure 3.1a.

3.3.2 MCS of Water Diffusion in Cervical Spinal Cord White Matter

The MCS of water diffusion was performed by uniformly distributing N water molecules into the IA and EA spaces of the LMI obtained from the excised pig CSC-WM (Figure 3.1b). No water molecules were assigned into the myelin space because the short T_2 (~ 10 ms) water protons in myelin space do not contribute to the total signal in the DWI with a relatively long TE ~100 ms (85,86).

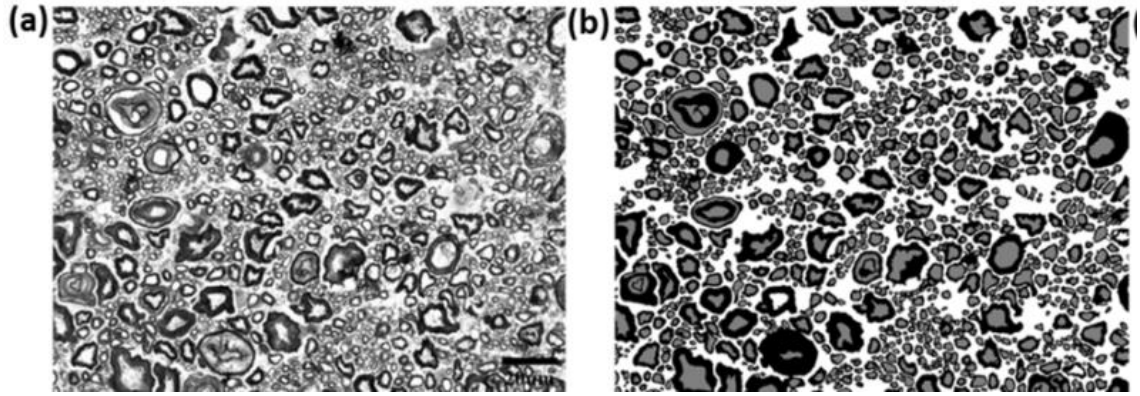

Figure 3.1: LMI- (a) a 2D cross-section view of a section of pig CSC-WM (187 × 140 μm^2) and (b) segmentation of the LMI shown in (a) into IA, EA, and myelin spaces. Scale bar in (a) is equal to 20 μm. In (b), the gray is IA space, white is EA space, and black is myelin space. The image was digitally segmented into three spaces: intra-axonal, extra-axonal, and myelin as shown in Figure 3.1b, using the ImageJ program available in the NIH public domain. Boundaries for the ambiguous sections, which were not successfully segmented by automatic thresholding, were manually drawn and assigned into either one of three spaces.

A three-dimensional diffusive motion was incorporated by updating the position of each molecule in every δt during a diffusion time T_{diff} as described in the literature (47–50,52–54). A new position of a molecule was calculated by adding a constant length, $(6D\delta t)^{1/2}$, and a random direction step vector to the current position. D is an intrinsic diffusion coefficient of a water molecule, and a random uniform direction is given by the spherical polar coordinates $\phi = 2\pi u$ and $\theta = cos^{-1}(2v - 1)$, where u and v are uniformly distributed random number in the range [0, 1]. The value of D was chosen based on the value of axial diffusivity, i.e., the diffusivity calculated with the DW gradient parallel to the fibers, measured as 0.50 $\times 10^{-3}$ mm^2/s in our specimen. Previously reported values of axial diffusivity, such as 0.47 $\times 10^{-3}$ mm^2/s from the five excised CSC of normal control subjects (99) and 0.62 $\times 10^{-3}$ mm^2/s from the three sections of a post-fixed excised pig CSC (100), also support the value of D chosen in the present study. Because the axial DW signal decays monoexponentially with b-value in our specimen, it does not violate common sense to choose the same value of D for both the IA and EA spaces as in (77). The details of the simulation parameters for the different sets of the simulations (S1, S2, S3, S4, and S5) are given in Table 3.1.

Table 3.1: The MCS parameters (units: D_{IA}, D_{EA} = mm^2/s; δt – μm; δ, Δ, T_{diff} – ms; b_{max} – s/mm^2)

$D_{IA} = 0.5 \times 10^{-3}$, $D_{EA} = 0.5 \times 10^{-3}$	- Diffusivities in IA and EA spaces
$\delta t = 0.1, T_{diff} = 600$	- Update time and diffusion time
$N = 18{,}000$ (IA – 32%, EA – 68%)	- Total molecules distributed
$S1: \delta = 25, \Delta = 100, b_{max} = 7{,}232$	
$S2: \delta = 45, \Delta = 75, b_{max} = 10{,}650$	
$S3: \delta = 50, \Delta = 100, b_{max} = 18{,}261$	
$S4: \delta = 30, \Delta = 450, b_{max} = 29{,}380$	
$S5: \delta = 45, \Delta = 225, b_{max} = 31{,}550$	

In this simulation, axons were considered as nonpermeable unless otherwise stated. When a molecule crossed a local barrier (IA or EA space to myelin space), the last position was abandoned and a new position was generated in a random direction until it finds a position belonging to the same space as described by Xing et al. (54). A molecule was either transmitted or reflected at the boundary with a probability that is determined by the permeability, P, as discussed by Szafer et al. (47), when the axons were considered as permeable. The P = 5 μm/s was chosen based on the previously reported value of permeability 2.7 μm/s in Xenopus oocytes (101) and 7.0-9.0 μm/s in bovine optic nerve (52). The successful positions of all molecules were recorded for every 100 μs time step. The DW signal was then obtained by computing the phase accumulated by each molecule during the position–recording steps and summing the contributions from all water molecules as $S = \sum_k \mathrm{S_k}(0)\exp(-i\gamma \sum_j (\boldsymbol{r_{jk}} \cdot \boldsymbol{G_D^j})\delta t)$, where $\mathrm{S_k}(0) = 1$ is the signal from the k^{th} molecule without diffusion-weighting, $\boldsymbol{r_{jk}}$ is the position vector of k^{th} molecule in j^{th} time step, and $\boldsymbol{G_D^j}$ is the applied gradient in j^{th} time step. Variation in the b-value was achieved by varying the gradient amplitude. The signals for IA, EA, and total (IA plus EA) spaces were calculated using the molecules distributed only in the IA, EA, and total spaces, respectively. The signal-b curve, which is obtained with the DW gradient applied perpendicular to the fibers, can be much more informative than that applied parallel to the fibers. Therefore, the MCS is performed with radial DW gradient unless otherwise stated. The T_2 values for the water molecules in IA and EA spaces are assumed to be the same, and the effect of T_2 is ignored in the signal calculation.

The MCS software was programmed using Message Passing Interface (MPI) C++ to utilize parallel processors available at the Center for High-Performance Computing

(CHPC) of the University of Utah. The computation time was 20−25 min for T_{diff} = 600 ms with 24 processing elements.

3.3.3 MRI Experiment

The axial DW images were obtained using three-dimensional multishot DW stimulated echo planar imaging (ms-DWSTEPI) (102) with echo train length 9 on a Siemens 3T MRI system (Trio, Siemens Medical Solutions, Erlangen, Germany). The system was equipped with the maximum gradient strength and gradient slew rate as 40 mT/m and 200 mT/m/s, respectively. A homebuilt birdcage coil (1.27 cm inner diameter, 2.54 cm in length) was used as a transmit-receive coil. The specimen was immersed into a tube filled with a thick gel of corn starch to remove the susceptibility artefact at the surface of the tissue. The details of imaging parameters for the different sets of measurements (M1, M2, and M3) are given in Table 3.2. The repetition times (TRs) were chosen in such a way that each measurement would have similar recovery time for the longitudinal magnetization. The DW gradient was applied in the left-right direction while the spinal cord was parallel to the B_0 (static field) direction. The post-processing of the DICOM images was performed using software written in Python. Variation in the b-value was obtained by varying the gradient amplitude.

3.3.4 Curve Fitting

The total signal-b curve was fitted to a monoexponential plus constant fitting (MCF) model $S_b/S_0 = f_{decay}\ \exp(-b.ADC) + f_{const}$ using nonlinear curve-fitting sub-routine included in SciPy (Python), where S_b and S_0 are signals at a given b-value and b_0

Table 3.2: The MRI parameters (units: $\delta, \Delta, \mathrm{TE}, \mathrm{TR}, \mathrm{TM} - \mathrm{ms}$ and $\mathrm{b_{max}} - \mathrm{s/mm^2}$)

FOV = 96×24 mm^2	In-planner resolution = 0.75×0.75 mm^2
Acquisition matrix = $128 \times 32 \times 16$	Slice thickness = 2 mm
Bandwidth = 500 Hz/Pxl	Scan time = 30– 60 min for 2 averages
$M1$: $\delta = 30, TE = 90, TR = 1050, TM = 450,$ $\boldsymbol{b_{max}} = 30{,}082$	
$M2$: $\delta = 30, TE = 120, TR = 1050, TM = 450,$ $\boldsymbol{b_{max}} = 30{,}017$	
$M3$: $\delta = 45, TE = 120, TR = 825, TM = 225,$ $\boldsymbol{b_{max}} = 28{,}226$	

($b = 0$ s/mm^2), respectively. f_{decay} and f_{const} are the fractions of decaying and constant signals, respectively. ADC is the apparent diffusivity of the decaying signal.

3.4 Results

3.4.1 Monte-Carlo Simulation

The MCS of water diffusion, which was performed with LMI (Figure 3.1b) obtained from a section of pig CSC-WM as an input geometry, predicted that the signal-b curve remains almost constant (decay rate 0.22×10^{-5} mm^2/s) for the IA space; however, the signal-b curve for the EA space decays approximately monoexponentially (decay rate 0.15×10^{-3} mm^2/s) to about 2% of its initial value when the b-value is increased to 30,000 s/mm2 as shown in Figure 3.2, under the condition that the maximum gradient strength is in the range of gradient strength available in most clinical scanners (< 40 mT/m). The total WM signal synthesized in the simulation decreases in the low-b region and remains constant in the UHB region because the total signal is the sum of decaying signal from EA space and almost constant signal from IA space. Therefore, the total signal-b curve in the MCS can be fitted with a monoexponential plus constant function (49,78). The MCF of the total signal-b curve estimated the values of f_{const} and ADC as 0.34 ± 0.03 and $(0.17 \pm 0.03) \times 10^{-3}$ mm^2/s, respectively.

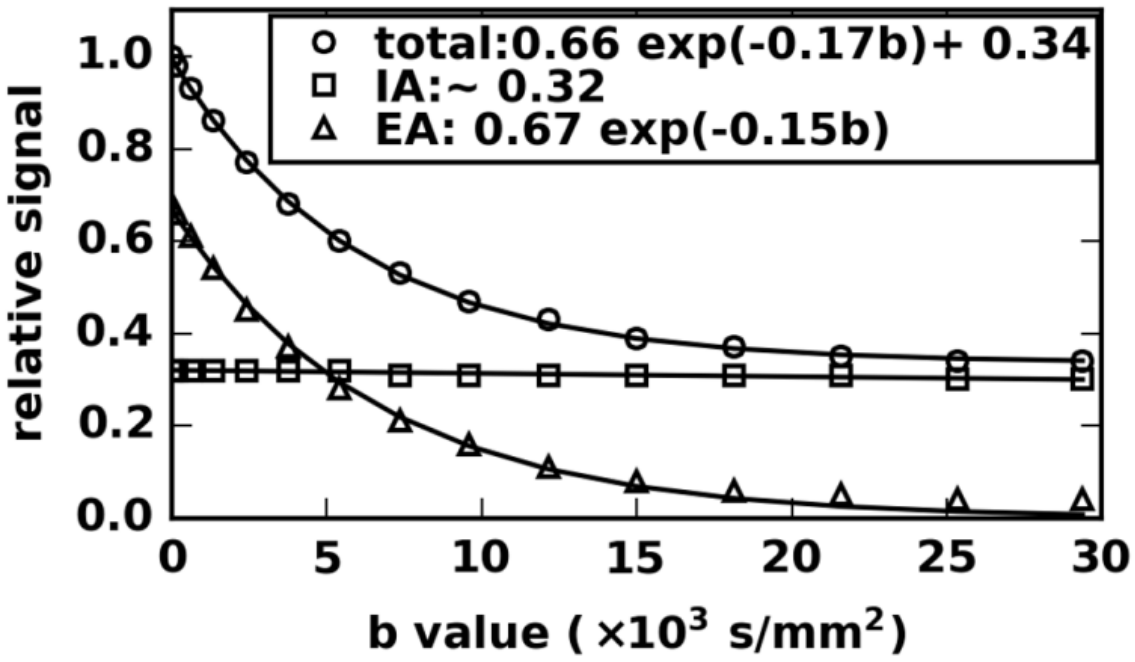

Figure 3.2: MCS- signal-b curves obtained from the MCS of water diffusion in a section of WM shown in Figure 3.1b. Solid lines are the MCF of the total signal and monoexponential fitting of the signals from the IA and EA spaces. S4 set (δ = 30 ms, Δ = 450 ms, and G_D = 0−40 mT/m) was chosen for the simulation.

Based on the MCS, the behavior of the signal-b curve is affected by various factors such as deviation of the direction of DW gradient from the actual radial direction of fibers and the existence of exchange of water molecules (permeability) between IA and EA spaces. It can be seen from Figure 3.3 that the total signal no longer remains constant in the UHB region when the direction of the DW gradient is not perfectly perpendicular to the fibers (Figure 3.3a) or exchange occurs between the molecules in the IA and EA spaces (Figure 3.3b). On the other hand, the signal-b curves decay in a similar fashion (Figure 3.3c) for all the simulation sets (S1-S5) independent of the imaging parameters, which indicates that the signal behavior does not depend on the chosen imaging parameters.

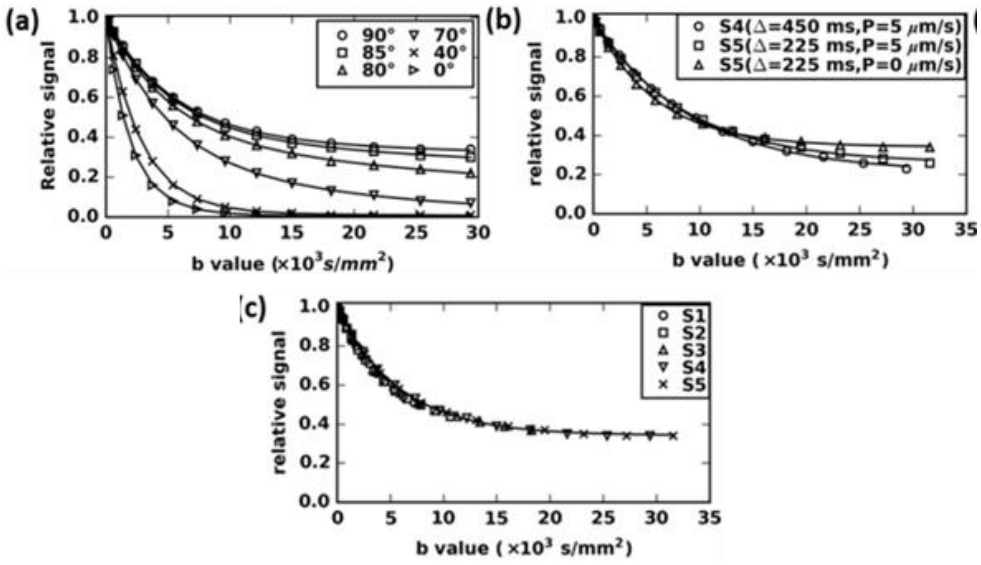

Figure 3.3. MCS- signal-b curves for (a) the various angles between DW gradient and fiber directions, (b) different diffusion times with exchange of molecules between IA and EA spaces, and (c) different sets of diffusion parameters given in Table 3.1. The solid lines are the MCF of the total signal-b curves.

3.4.2 Ex Vivo UHB-rDWI Experiments

The presence of noise in a measurement degrades the accuracy of fitting parameters obtained from the MCF of the signal-b curve. In our study, the signal-to-noise ratio (SNR) > 100 was measured in b_0 images. The signal-b curve of each pixel was fitted with the MCF function, and f_{const} and ADC maps were obtained from a 2-mm-thick slice at the level of the C3-C4 vertebrae. The DW images (b_0 and b_{max}) and MCF parameter maps (f_{const} and ADC) obtained in the UHB-rDWI are shown in Figure 3.4a. Typical signal-b curves obtained from a pixel of WM for three sets measurements are shown in Figure 3.4b. The MCF of the signal-b curves obtained from the WM pixel (Figure 3.4b) estimated the values of the f_{const} as 0.32 ± 0.05, 0.29 ± 0.05, and 0.32 ± 0.06 and the values of ADC as $(0.16 \pm 0.01) \times 10^{-3}$ mm^2/s, $(0.16 \pm 0.01) \times 10^{-3}$ mm^2/s, and $(0.17 \pm 0.01) \times 10^{-3}$ mm^2/s for the M1, M2, and M3 measurements, respectively.

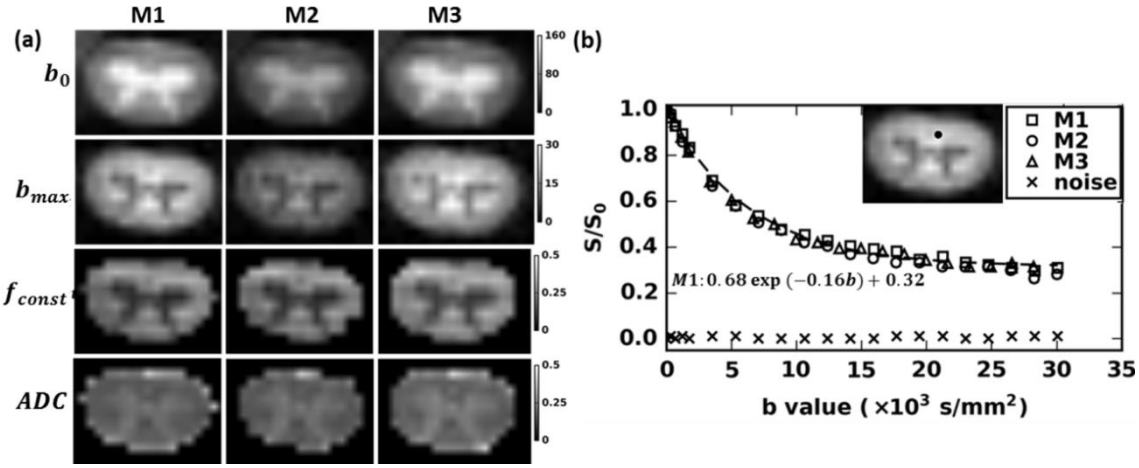

Figure 3.4: Ex vivo UHB-rDWI: (a) DW images with b_0 (first row), DW images with b_{max} (second row), f_{const} maps (third row), and ADC maps (fourth row) for three different measurements M1 (first column), M2 (second column), and M3 (third column). (b) Typical signal-b curves from a pixel of WM for the different sets of the imaging parameters given in Table 3.2. The dashed line in (b) is the MCF of the signal-b curve obtained for the measurement M1.

3.5 Discussion

The MCS predicted that the radial DW signal remains almost constant (monoexponential decay rate 0.22 $\times 10^{-5}$ mm^2/s) for the IA space. The signal decay rate for the IA space is negligible compared to the signal decay rate 0.15 $\times 10^{-3}$ mm^2/s for the EA space. Therefore, the signal from the IA space has been considered as almost constant with respect to the b-value. In a region where the b-value is greater than 20,000 s/mm^2 (the UHB region), the total signal is mainly from the IA space and is almost constant. The maximum radial displacement of molecules in the IA space is limited by the diameters of the axons, no matter how long the diffusion time is allowed. As a result, the applied radial DW gradient (strength < 40 mT/m) does not create enough phased dispersion between spins confined inside a smaller axon (diameter < 4 μm), which is required for the signal loss in DWI. For the limit of a long time ($\delta D >> R$), and $G_D = 40$ mT/m, $\delta = 30$

ms, and $D = 0.5 \times 10^{-3}$ mm^2/s, approximately 2% radial DW signal loss has been calculated for an impermeable cylinder of diameter ($2R$) 4 μm using Neuman's formula (89): $\ln(S/S_0) \cong 7(\gamma G_D)^2 R^4 \times 2\delta/96D$. In the MCS, nearly 7% signal loss was observed from the IA space, which may be due to the presence of bigger axons in the LMI (Figure 3.1b). Most axons in the LMI are not circular in cross-section; therefore, the diameter of the axon measured only along the DW field gradient direction (left-right) represents the size of the restriction. The signal from the IA space may decay with b-value when a very high DW gradient strength (~1,000 mT/m) is used. This is because even a small molecular displacement will be sufficient to create enough phase dispersion in the presence of very high DW gradient strength. Use of the very high DW gradient strength (1,000 −1,400 mT/m) can be found in a bovine optic nerve experiment (52) and in a simulation of water diffusion inside a cylinder (40). Therefore, higher b-value with lower gradient strength and shorter δ (longer Δ) is preferred to get a constant signal from the IA space. The MCF of a signal-b curve obtained in the MCS estimated the values of f_{const} and ADC as 0.33 ± 0.03 and $(0.17 \pm 0.03) \times 10^{-3}$ mm^2/s, respectively. The estimated constant fraction agreed well with the fraction of the IA space (0.32) measured from the LMI (Figure 3.1b) when the myelin space is neglected. In the UHB-rDWI measurements, a MCF of the signal-b curve obtained from a WM pixel estimated the values of f_{const} and ADC of decaying fraction as 0.32 ± 0.05 and $(0.16 \pm 0.01) \times 10^{-3}$ mm^2/s, respectively, for the set M1, which agreed well with the results of the MCS. Almost similar decaying patterns of the signal-b curves were observed in all three measurements (M1, M2, and M3, Figure 3.4b), which agreed well with the findings of the MCS (Figure 3.3c).

The physical environment within a biological sample is very heterogeneous, and a two- compartment model is too simplified; however, it does not violate common sense if the WM space is divided into two compartments for the radial diffusion: (i) “restricted space” mainly composed of the IA space and (ii) “hindered space” composed of EA space, astrocytes, oligodendrocytes, and immune cells in pathologic cord. The validity of this model is that axons are surrounded by several tens of lipid bilayers (myelin), of which one side of this bilayer is hydrophobic. The lipid bilayers completely block the exchange of water molecules between the IA space and myelin/EA space. The majority of the hindered space is covered by the EA space, and the diffusion in all hindered spaces is assumed to be same as in the EA space. If there were a restricted space other than IA space, for instance, a restricted space formed by astrocytes and oligodendrocytes, the signal measured in the UHB region should have similar values for both the radial and axial DWI as the restricted space formed by the astrocytes and oligodendrocytes provides equal restriction in both radial and axial diffusive motion. The axial and radial signal-b curves measured from a WM and GM pixels are shown in Figure 3.5. Anisotropic diffusion observed in WM in the UHB region supports the argument that the restricted signal is mainly from the IA space. Isotropic diffusion observed in GM shows the presence of similar restrictions both in radial and axial directions.

Since the hindered space, which is composed of EA space, astrocytes, and oligodendrocytes, is too complicated to be modeled by a simple geometry, it is convenient to interpret the DW signal after suppressing the signal from the hindered space by applying a sufficiently high diffusion-weighting. After the suppression of the signal from the hindered space, the remaining signal is solely from the restricted space

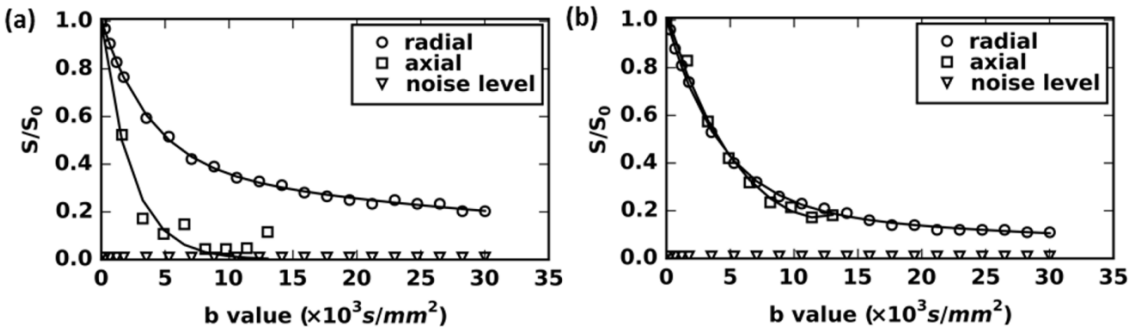

Figure 3.5: Experimental signal-b curves for axial and radial DWI in (a) WM and (b) GM. The axial DW signal in WM quickly decays to noise level, indicating almost no barrier, but in the GM, the slow-decaying axial signal indicates the existence of some restrictions even along the axial direction.

(IA space). The integrity and intactness of the axons may be characterized by assessing the signal purely from the IA space. The restricted signal (f_{const}) may represent the intra-axonal fraction (IAF); however, the value of f_{const} may deviate from the actual IAF if different values of T_2 exist in two different spaces: restricted and hindered spaces.

The signal behavior in the UHB region may be affected by the application of imperfect radial DW gradients with respect to fibers, the presence of the orientational (angular) fiber dispersion within a voxel, and the existence of the exchange of water molecules between IA, EA, and myelin spaces. The effect of an imperfect radial DW gradient may be corrected by measuring the angle between fibers and the applied gradient field using conventional diffusion tensor imaging (DTI). To our knowledge, the value of angular fiber dispersion in the CSC-WM has not been reported in the literature; however, the value of the orientation dispersion index (ODI) has been reported as 0.03 using the NODDI model (103), which is much smaller than the ODI value 0.14 reported for a corpus callosum-body (104). The ODI has been considered as a measure of the angular dispersion of the fibers within a voxel. The angular fiber dispersion in the corpus

callosum-body has been reported as 18.1° (105). Since the ODI of CSC-WM is nearly one-fifth of the ODI of corpus callosum-body, the angular fiber dispersion of the CSC-WM may be estimated as 3−4°, one-fifth of the angular dispersion of the corpus callosum. The effect of such a smaller angular dispersion may not be significant in the UHB region. The exchange effect may also be evaluated by assessing the remaining signal in the UHB region for different diffusion times (~TMs) as described in (106–109). These previous studies applied the "diffusion filter" to attenuate the signal from the fast-diffusing compartment (EA space), which is not required in the present study as the signal from the EA space is almost suppressed in the UHB region. In the present study, the angle between fibers and applied DW gradient was measured using conventional DTI. The DW gradient was found to be perpendicular to the fibers within the range of 5°, which does not significantly change the value of restricted fraction and decaying pattern of the signal-b curve in the UHB region (see Figure 3.3a). If there were an exchange of water molecules between IA and EA spaces, a lower value of f_{const} would be anticipated in M2 (TM = 450 ms) compared with M3 (TM = 225 ms), as predicted by the MCS. The UHB-rDWI estimated a 9% smaller value of f_{const} in M2 than in M3. Minor effects of exchange may be observed due to exchange of molecules via the nodes of Ranvier. The fitting parameters of the signal-b curves were not significantly different for different values of TM (TM = 27−219 ms and $b_{max} = 28{,}000$ s/mm^2) in the DWI study of the human brain in vivo (77), this finding also supports the fact that the exchange of molecules between IA and EA spaces in WM is not significantly high.

In vivo application of this technique is feasible but not as easy as ex vivo application because the DW images suffer from low SNR due to the short scan time and

deeper location of the CSC from the skin. The diffusion coefficient is generally three times faster in the in vivo tissue than in the ex vivo, which greatly reduced the high b-value to 10,000 s/mm^2 needed to suppress the signal from hindered space (110). In vivo human spinal cord imaging with the maximum b-value of 14,000 s/mm^2 (78) and 7,300 s/mm^2 (94) have already been reported, which demonstrates the possibility of the in vivo application of this technique.

3.6 Conclusions

Based on the MCS, we conclude that the radial DW signal from the hindered space can be suppressed when b-value is sufficiently high (~ 20,000 s/mm^2 in our specimen), and the radial DW signal from the IA space remains almost constant independent of the b-value provided that the water molecules do not exchange between IA, myelin, and EA spaces. Axial and radial DWI of the ex vivo spinal cord excluded the possibility of restricted space in WM other than IA space. The signal measured in the UHB region is mostly from the restricted space, i.e., IA space. Integrity and intactness of the axons in WM can be evaluated by assessing the signal in the UHB region. The fraction of restricted water and the decay rate of the signal-b curve in the UHB region are the two essential biomarkers for the characterization of the WM. Both biomarkers can be affected by the application of a nonperfect radial diffusion gradient, the presence of the angular dispersion within a voxel, and the existence of the exchange of molecules between the IA and EA spaces.

CHAPTER 4

EIGHT-CHANNEL DECOUPLED ARRAY FOR CERVICAL SPINAL CORD IMAGING AT 3T: SIX-CHANNEL POSTERIOR AND TWO-CHANNEL ANTERIOR ARRAY COIL

This chapter is adapted from a pper entitled "Eight-channel decoupled array for cervical spinal cord imaging at 3T: six-channel posterior and two-channel anterior array coil"authored by Nabraj Sapkota, Bijaya Thapa, YouJung Lee, Taeho Kim, Erica F. Bisson, Lubdha M. Shah, John W. Rose, and Eun-Kee Jeong. The paper has been published online in the journal Concepts in Magnetic Resonance Part B in August 2016.

4.1 Abstract

The purpose of this study was to develop a dedicated high signal-to-noise ratio (SNR) radio frequency coil for cervical spinal cord (CSC) imaging without using the preamp decoupling technique. A novel eight-channel CSC array was constructed using a butterfly, loop (circular), and rectangular elements. The adjacent elements were decoupled by critical geometrical overlapping, and most nonadjacent elements were decoupled using loop and butterfly elements. The performance of the proposed CSC coil was compared with the performance of the standard manufacturer's coil (Siemens' head,

neck and spine array) at 3T MRI system in T_2-weighted images, diffusion tensor images, and ultrahigh-b diffusion-weighted images. In T_2-weighted images, the SNR improvement of the eight-channel CSC coil was $1.4-2.0$ times over the manufacturer's coil at the different levels of the CSC vertebrae. Higher contrast between white matter and gray matter was observed in the diffusion-weighted ($b = 500$ s/mm^2) images and the fractional anisotropy maps obtained using the eight-channel CSC coil compared with the manufacturer's coil. The eight-channel CSC coil yielded 2.0 times higher SNR compared with the manufacturer's coil from the white matter region of the ultrahigh-b ($b = 7348$ s/mm^2) radial diffusion-weighted images.

4.2 Introduction

Magnetic resonance imaging (MRI) is routinely used for cervical spinal cord (CSC) imaging because of its high soft-tissue contrast and noninvasiveness; however, the conventional MRI techniques such as T_1- and T_2-weighted imaging, in general, do not detect the pathologic changes in early stages (111). It is also almost impossible to distinguish between neuronal structures and interstitial parenchymal tissues using conventional MRI techniques (5). Advanced MR imaging techniques such as diffusion-weighted imaging (DWI) (112) and diffusion tensor imaging (DTI) (113,114) have been emerging as potential techniques to detect the subtle lesions of the CSC in the earliest stages. The technical challenge for imaging of the CSC using advanced MRI methods is the low signal-to-noise ratio (SNR) from the small cross-section of the cord (115).

The receive-only array has been used since its development by Roemer et al. (55) to increase the SNR from the localized region and to reduce the acquisition time using

parallel imaging (116,117). The imaging field-of-view (FOV) can be enlarged by increasing the number of coil elements. However, an increase in the number of elements will increase the complexities in the design and construction of an array (55). One of the most difficult tasks in an array design is to eliminate the coupling between elements. The commonly used methods to reduce the coupling between the elements are geometrical and electrical decoupling (118,119). Two adjacent elements in an array are decoupled by the critical geometrical overlapping, while the decoupling of nonadjacent elements is challenging. The widely used technique to minimize the coupling between nonadjacent elements is preamp decoupling using low-input impedance preamplifiers (55,67). However, the preamp decoupling technique increases the complexities in array design because the low-input impedance preamplifiers are not ubiquitous (120). This technique also requires a special deactivation circuit at the desired frequency formed by a parallel capacitor and a series inductor as a matching network, which always adds extra complexity in matching. In addition, the preamp decoupling technique complicates the parallel transmission, which is usually required in ultrahigh-field MRI systems (≥ 7T) (121). Another problem associated with a multielements array is that the number of elements in an array is, in general, increased by decreasing the size of the elements from their optimal size. The SNR of superficial tissues increases with increase in a number of elements but not necessarily of the deeper tissues (122), such as a CSC, which is located at about $5-7$ cm depth from the skin in a typical adult neck.

Although the receive-only array was first developed for CSC imaging, not much work has been done for the design and development of the CSC dedicated array. Recently, some array designs have been proposed for the CSC imaging at 3T MRI

systems (123–128). These include a 4-channel planar array for T- and L-spine (127), an 8-channel array for CSC (126), a 16-channel array for the head and neck (124), a 16-channel SENSE optimized array for CSC (125), a 32-channel array optimized for brain and CSC (128), and a 64-channel array for head/neck/CSC (123). With the increasing interest in the higher field, in the past few years, there have been a few CSC array designs proposed for the 7T MRI systems as well (129–133). The coil designs for the higher field include a 4-channel array for the CSC (131), an 8-channel array for the entire vertebral column (132), a 19-channel array for the CSC (133), and a 22-channel array with the elements wrapping around the neck (129). All these previous designs rely on the preamp decoupling to reduce the coupling between nonadjacent elements. Keren (120) has patented an array design composed of periodically arranged two square elements followed by two butterfly elements so that the coupling between nonadjacent elements (square-butterfly) was negligible. The disadvantage of this design is that the butterfly element has less penetration depth compared with the similar-sized circular/square element and, hence, the array may suffer from low SNR.

In this work, we present a novel array design for CSC imaging in which the couplings between adjacent as well as nonadjacent elements are reduced by overlapping the elements critically and by choosing the circular and butterfly-shaped elements, respectively. The number of elements in the proposed array is increased by maintaining the optimal size of each element. The proposed decoupled array is constructed based on the naturally decoupled array designs (134,135). Because most nonadjacent elements are decoupled using the loop and butterfly elements, the preamp decoupling technique is not required in the new CSC array, which enables us to use 50 Ω preamplifiers.

4.3 Methods

4.3.1 Mutual Induction and Decoupling

The coupling (flux linkage) between two elements is determined by the mutual induction between them. The mutual induction M_{ij} between the coils i and j can be calculated using the equation (55)

$$M_{ij} = \frac{\mu_0}{4\pi} \iint \frac{d\boldsymbol{s_i} . d\boldsymbol{s_j}}{|\boldsymbol{r_i} - \boldsymbol{r_j}|}, \quad [4.1]$$

where $d\boldsymbol{s_i}$ and $d\boldsymbol{s_j}$ are the vector length elements of the coils i and j, respectively. $|\boldsymbol{r}_i - \boldsymbol{r}_j|$ is the distance between the length elements $d\boldsymbol{s_i}$ on coil i and $d\boldsymbol{s_j}$ on coil j.

The loop and butterfly elements used in the proposed array are depicted in Figure 4.1a. These elements are in the xz-plane at y = 0. The loop element of diameter $D = 10$ cm and the butterfly element of size 10 cm × 20 cm (the long axis of the butterfly element is perpendicular to the static field B_0) are chosen for the mutual induction calculation. The magnetic couplings (M_{ij}) of loop-loop, butterfly-butterfly, and loop-butterfly pairs, which were calculated using Eq. [4.1], are shown in Figure 4.1b. For the two loop elements of diameter 10 cm, the coupling is found to be minimum when their centers are separated by 7.6 cm, which agrees well with the reported value of 7.5 cm (55). Similarly, the mutual inductance between two butterfly elements of size 10 cm × 20 cm becomes minimal when their centers are 9.2 cm apart. The mutual inductance between the loop and butterfly elements is almost negligible and is independent of the distance between their centers along z-axis provided that the x-coordinate for the center of both elements is same. The negligible coupling between a loop and butterfly element enables us to design an array with negligible coupling between nonadjacent elements.

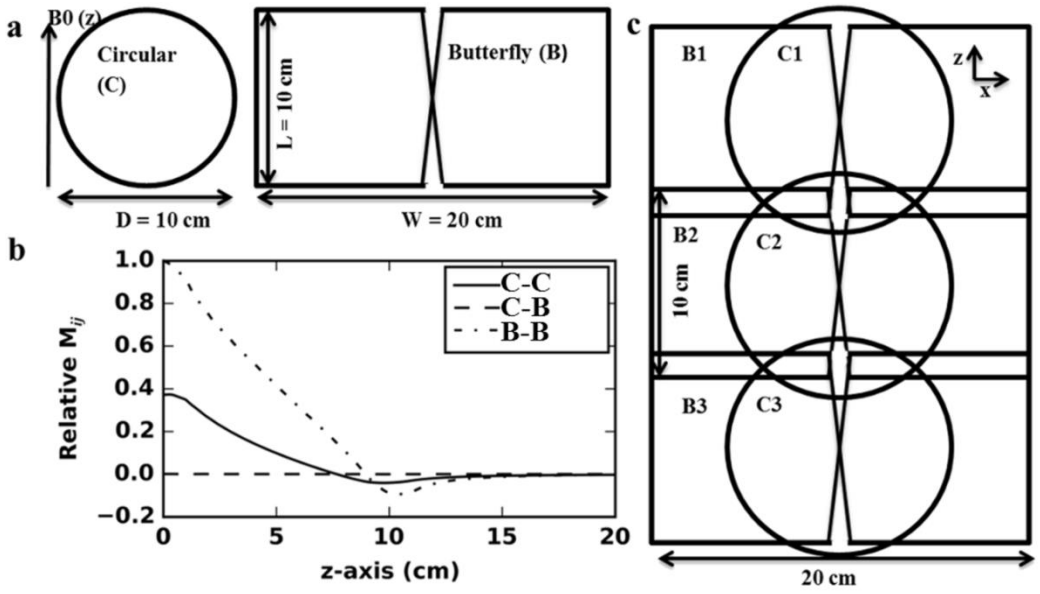

Figure 4.1: (a) Outline of a loop and butterfly elements. (b) Mutual induction (M_{ij}) between two elements of a butterfly-butterfly (B-B), loop-butterfly (C-B), and loop-loop (C-C) pairs with respect to the distance between their centers along z-axis (B_0 direction). (c) Outline of a six-channel posterior array made of three loop-butterfly pairs.

An outline of a six-channel posterior array proposed in this work is shown in Figure 4.1c. The coupling of the adjacent loop-loop and butterfly-butterfly pairs is minimized by the critical geometrical overlapping. The adjacent and nonadjacent loop-butterfly pairs couple very lightly because of the orthogonal nature of the magnetic field between them (72). The coupling of the nonadjacent loop-loop ($C1 - C3$) and butterfly-butterfly pairs ($B1 - B3$) is also negligible because the elements of each pair are far away from each other. The two-channel anterior array (not shown in figure) is simply made of a butterfly and coaxial rectangular elements and their coupling is also minimal because of the orthogonal nature of the magnetic field between them.

The preamp decoupling is required when the coupling between the nonadjacent elements is significant. In the proposed array design, the coupling between the nonadjacent elements is negligible, which eliminates the requirement of the preamp

decoupling technique and allows us to use the 50 Ω preamplifiers. The array can be extended to any number of channels to increase SNR as well as FOV; however, the extension must be applied along the B_0 direction (z-axis of the Figure 4.1c).

4.3.2 Coil Sensitivity

A pair of coaxial loop and butterfly elements, shown in Figure 4.2a, can be considered as a unit block in the proposed array design. In a conventional CSC array design, two loop/rectangular elements, shown in Figure 4.2b, are overlapped sidewise (126,127,131). Therefore, a loop-loop pair overlapped sidewise can be considered as a unit block in the conventional design. To compare the sensitivity of the proposed design with the conventional design, it is fair to compare the sensitivity of the unit block from both designs, i.e., a pair of coaxial loop-butterfly elements in the proposed design and a pair of loop-loop elements overlapped sidewise in the conventional design.

The signal induced in a coil by the precessing transverse magnetization of a sample is proportional to the imaginary transverse component (B_1) of the magnetic field produced on the sample by the coil with unit DC current (136). Therefore, the sensitivity of each element is determined by the strength of the B_1-field generated on the sample by the element with unit DC current. The B_1-field is calculated using the Biot-Savart's law (66). The array sensitivity is obtained by combining the sensitives of all the elements using the square root of the sum-of-squares (SOS) method (55). The sensitivities of the unit blocks of the proposed and conventional designs are shown Figure 4.2c and d, respectively. Similar coil sensitivities were observed between the conventional loop-loop pair and the proposed coaxial loop-butterfly pair.

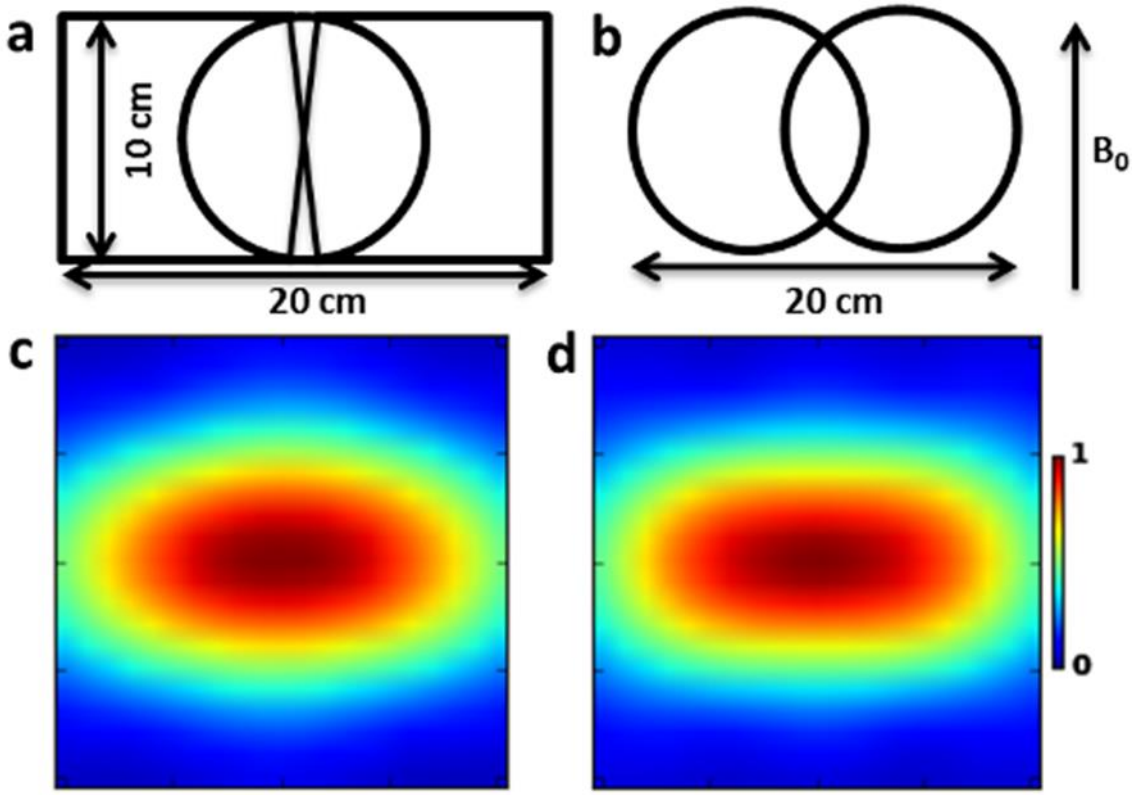

Figure 4.2: Outline of a unit block of the (a) proposed array shown in Figure 4.1c and (b) conventional array (15,20,19). (c)- (d) B_1-field maps (FOV = 20 cm × 20 cm) at a distance of 6 cm from the plane of the unit blocks (a) and (b), respectively. The loop element of diameter 10 cm and the butterfly element of size 10 cm × 20 cm were used for the B_1-field calculation. The same scale is used in both (c) and (d).

4.3.3 Coil Former

Anterior and posterior formers with the coil elements on each former are shown in Figure 4.3a and b. The formers were modeled on average-sized human-neck mold to increase the filling factor by minimizing the distance between the coil and CSC. The formers were made of fiberglass cloth (917, Evercoat, OH, USA), epoxy (105 part 1, West System, MI, USA), and hardener (206 part 2, West System, MI, USA). The interior surface of each former was covered with a $2-$mm thick foam layer to comfort the subject.

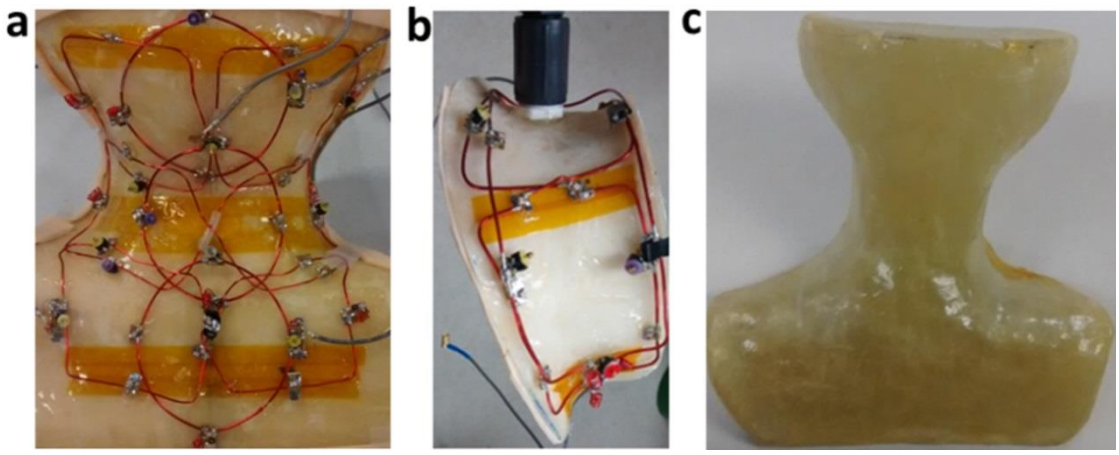

Figure 4.3: Photographs- Layout of the (a) six-channel posterior array and (b) two-channel anterior array. (c) Neck-shaped phantom. The coil former fits well to the average-sized human neck.

4.3.4 Phantom Construction

A neck-shaped phantom, shown in Figure 4.3c, was constructed from the fiberglass, epoxy, and hardener using the same posterior human-neck mold that was used to construct the posterior coil former. The phantom was filled with saline, doped with 0.1 mM $MnCl_2$.

4.3.5 Coil Construction

The human CSC runs along the middle of the neck ($5 - 7$ cm deep from the surface) between the C1-C7 vertebrae. A layout of the posterior array, which mainly covers the CSC, and consists of six elements (three loop and three butterfly elements) arranged on the curved surface of the posterior former is shown in Figure 4.3a. In a planar geometry, a loop element with diameter and square butterfly element with square side length equal to the depth of interest are considered as optimal sizes (57,66,72,126). However, a numerical simulation using Biot-Savart's law indicates that the optimal

diameter of the loop element increases on a cylindrical surface, compared with that on a planar surface (126). Therefore, loop elements of diameter about 10 cm and butterfly elements of size about 10 cm × 20 cm were chosen to contruct the elements of the CSC coil. Magnet wires of 14- and 16-gauges were chosen for the loop and butterfly elements, respectively. Thicker wire (smaller gauge) was chosen for the loop elements because it provides lower AC resistance compared with thinner wire (higher gauge); however, thinner wire was the choice for the butterfly elements to facilitate easy bending at the time of geometrical decoupling. The long axis of the butterfly element was wrapped around the former and the short axis was parallel to the B_0 field. The adjacent loop-loop and butterfly–butterfly pairs were overlapped in such a way that their coupling was minimal. The loop and butterfly elements were placed in such a way that their centers were collinear along the z-axis. The anterior array consists of a 7 cm × 25 cm butterfly and 7 cm × 20 cm rectangular elements, arranged co-axially on the curved surface of the anterior former as shown in Figure 4.3b. The smaller width of the anterior former and coil elements were chosen to fit the former on the human front neck. Both elements of the anterior array were made of 16-gauge magnet wire. The posterior array covers the spinal cord from the brain stem down to the T3 vertebra and the anterior array covers C3-C7 vertebrae. The critical overlapping area of the adjacent elements on the curved surface slightly deviates from that calculated on the planar layout. As a result, the shape and size of the elements arranged on the curved former (Figure 4.3a) are slightly deformed from the shape and size of the elements arranged on the planar surface (Figure 4.1c).

A circuit schematic diagram for an individual element of the CSC array is shown in Figure 4.4. The coil element was symmetrically divided into 4 segments for the loop

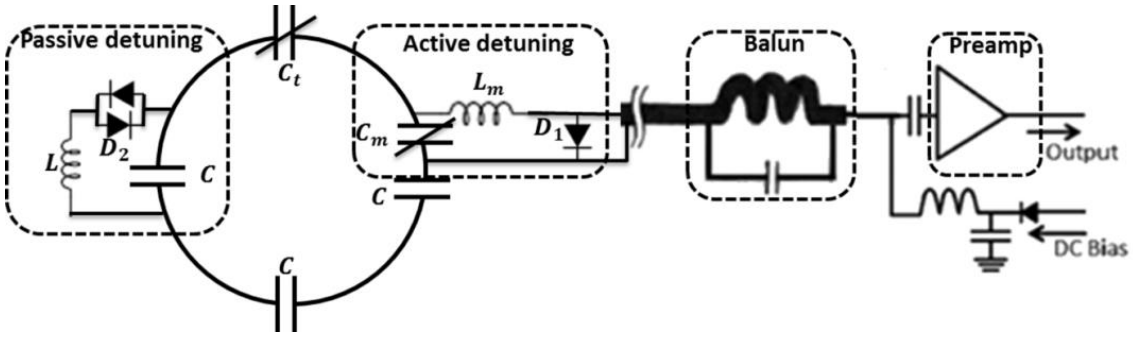

Figure 4.4: Circuit schematic diagram for an element of the CSC coil.

elements, 6−8 segments for the butterfly and rectangular elements, and 12 segments for the anterior butterfly element. The tuning of each element was carried out by adjusting a variable tuning capacitor C_t (20−40 pF); a parallel combination of a fixed capacitor (American Technical Ceramics, NY, USA) and a trimmer capacitor (Sprague-Goodman Electronics, NY, USA). The matching of each element was performed by adjusting a matching capacitor C_m (30−60 pF); a parallel combination of a fixed and trimmer capacitors; and a matching hand-wound inductor L_m (3−4 turns). Each individual element was equipped with the active and passive detuning circuits composed of standard parallel LC resonant circuit. At the resonance frequency, the parallel LC-circuit ideally poses infinite input impedance and the circuit is equivalent to an open-circuit (19). When the active trap is activated by forward biasing the PIN diode D_1 (MA4P7104F, MACOM Technology Solutions Inc., CA, USA) using 100 mA DC current from the MRI scanner, the L_m and C_m of the trap would form a parallel LC circuit, which deactivates the element by creating an equivalent open circuit at the coil input terminals. In contrast, the passive trap, composed of crossed-switching diodes D_2 (MX51363-145, Voltronics, MD, USA), is activated only by the high-power AC current. When the active trap fails to

deactivate a coil during the transmission of radiofrequency (RF) pulses, the coil picks up very high transmit power and high current flows through the coil, which shorts the crossed-diode D_2. As a result, the hand-wound inductor L (5-7 turns) and the fixed capacitor C (20−30 pF) of the passive trap form a parallel LC circuit, which creates a virtual open circuit across the capacitor C (137). A cable trap (balun) consisting of a parallel capacitor (fixed, 27 pF) and a series hand-wound inductor made of semi-rigid coaxial cable (4 turns; UT-070, Microstock, PA, USA) was placed between the coil element and the preamplifier to reduce common mode current. The balun, a parallel LC circuit resonating at the proton frequency, provides very high impedance for the common mode current flowing through the outer cable shield and negligible impedance to the signal current flowing in the differential mode (68). Each coil element in the array was connected to a 50 Ω preamplifier (24 dB gain, 0.5 dB noise figures; P123VDG NMR, Advanced Receiver Research, CT, USA) with 20-30 cm cables (B7805R, type RG-174, Belden, MO, USA). The DC bias path, which allows the DC current to flow but blocks signal current, is composed of several series inductors (820 nH; CW252016-R82J, Bourns, CA, USA) and a PIN diode.

4.3.6 Coil Testing on Bench

The ratio of the unloaded and loaded (with phantom) quality factor Q-ratio was measured by connecting lightly coupled double loop probes to the two ports of a network analyzer (Agilent Technologies, CO, USA). The tuning, matching, active and passive detuning, and adjacent elements decoupling of each coil element was performed with the phantom loaded into the coil. The tuning and matching performances of the CSC coil

elements were evaluated by looking into each coil element via the network analyzer with all other coils overlapping. The performance of the active and passive detuning circuits was evaluated by measuring the decrease in transmission parameter ($S21$) using a lightly coupled double loop probe before and after the 100 mA DC current supplied into the coil element. The coupling between two elements was measured by connecting two elements to the two ports of the network analyzer, and by measuring the $S21$ parameter. All measurements were carried out by actively detuning the unused elements by supplying 100 mA DC current from the DC power supply (HY 3005F-3, Mastech, CA, USA).

4.3.7 Imaging Experiments

The CSC coil was tested on a Siemens 3T MRI system (Trio, Siemens Medical Solutions, Erlangen, Germany). Initial evaluation of the CSC coil was performed on a neck-shaped phantom using a gradient-echo (GRE) sequence with $TR = 400$ ms, $TE = 10$ ms, flip angle $= 25°$, in-plane resolution $= 2$ mm $\times 2$ mm, slice thickness $= 2$ mm, FOV read $= 256$ mm, FOV phase $= 192$ mm, acquisition matrix $= 128 \times 96$, number of average $= 2$, and acquisition time = 3 min 15 s. The noise only data were also obtained by setting RF pulse amplitude to zero for the calculation of the noise correlation matrix and the SNR map. After obtaining approval from the Institutional Review Board and informed consent from a healthy volunteer, in vivo imaging of a volunteer was conducted. T_2-weighted images were acquired in the axial plane ($TR/TE = 4$ s/95 ms, FOV read/phase $= 140$ mm/140 mm, scan time $= 4$ min 10 s, number of slice $= 30$, and acquisition resolution $= 0.68$ mm $\times$ 0.55 mm $\times$ 4.0 mm) and in the sagittal plane ($TR/TE = 4$ s/112 ms, FOV read/phase $= 220$ mm/220 mm, scan time $= 3$ min 34 s,

number of slice = 12, number of average = 2, and acquisition resolution = 0.92 mm × 0.69 mm × 3.0 mm) using a turbo spin-echo (TSE). Axial diffusion tensor images (TR/TE = 4 s/85 ms, FOV read/phase = 128 mm/44 mm, scan time = 3 min 32 s, number of slice = 12, number of average = 4, and acquisition resolution = 1.0 mm × 1.0 mm × 4.0 mm) were acquired using two-dimensional reduced-FOV single-shot diffusion-weighted EPI (2D ss-rFOV-DWEPI) sequence (138) with 12 diffusion-encoding directions and b-value 500 s/mm^2. Axial ultrahigh-b radial diffusion-weighted (DW) images (TR/TE = 3 s/64 ms, FOV read/phase = 128 mm/44 mm, scan time = 6 min 19 s, number of slice = 21, number of average = 6, and acquisition resolution = 1.0 mm × 1.0 mm × 4.0 mm), i.e., the DW images with the diffusion-weighting perpendicular to the fiber axis, were acquired using two-dimensional single-shot diffusion-weighted stimulated EPI with reduced-FOV (2D ss-DWSTEPI-rFOV) technique (94). The noise only data for the in vivo SNR calculation were also acquired with turbo spin-echo in the sagittal plane.

4.3.8 Noise Correlation Matrix and SNR Calculations

Raw measurement data from the imaging and separate noise only experiments were retrieved from the raw data database for the SNR calculation and noise correlation matrix calculation. The noise correlation matrix was calculated from the noise only data as described by Hayes et al. (139). The SNR of an individual channel was calculated by dividing the complex imaging data by the standard deviation of the noise only data. The array SNR was obtained by combining the SNR of all the channels using the square root of the SOS method (140,141).

The SNR of an array depends on the distance of the tissue being imaged from the array. Generally, the closer the tissue is to the coil the better the SNR is. Therefore, in the present study, a region of interest (ROI) was carefully chosen so that the SNR value best reflects the performance of the coil at the level of the CSC. In the phantom sagittal imaging, the ROI was drawn at a distance of $5-6$ cm from the surface of the coil, which is similar to the distance of the average human CSC from the surface of the skin. The performance of the CSC coil was compared with the manufacturer's coil by assessing the SNR from the ROIs drawn at the center of the CSC in the axial T_2-weighted images.

4.4 Results

4.4.1 Coil Testing on Bench

The ratio of unloaded and loaded Q (Q-ratio) was approximately 5 for all elements of the six-channel posterior array and approximately 3 for both elements of the two-channel anterior array. The active and passive detuning provided similar isolation less than -25 dB between resonating and detuned (100 mA DC current supplied) states for all channels. The coupling between elements of the six-channel posterior array is presented in Table 4.1. The $S21$ values of the adjacent loop-loop and butterfly-butterfly pairs were measured within the range $-20 \sim -16$ dB and the $S21$ measurements were -16 dB, -35 dB, and -26 dB for the nonadjacent $C1-C3$, $C1-B3$, and $B1-B3$ pairs, respectively. As predicted by the mutual inductance calculation, the coupling between the loop-butterfly pair was negligible ($S21$ value was in the range $-19 \sim -36$ dB with average value -28 ± 3 dB). The isolation between butterfly and rectangular elements of the two-channel anterior array was -15 dB.

Table 4.1: Isolation ($S21$) in dB between a pair of elements in the CSC array.

Coil	$\boldsymbol{C2}$	$\boldsymbol{C3}$	$\boldsymbol{B1}$	$\boldsymbol{B2}$	$\boldsymbol{B3}$
$\boldsymbol{C1}$	-20	-16	-36	-29	-35
$\boldsymbol{C2}$		-19	-22	-25	-20
$\boldsymbol{C3}$			-26	-26	-22
$\boldsymbol{B1}$				-20	-28
$\boldsymbol{B2}$					-16

4.4.2 Phantom Experiments

The CSC coil was first evaluated on a neck-shaped phantom with GRE sequence. The noise correlation matrix and SNR map, which were calculated on the phantom using the CSC coil, are shown in Figure 4.5a and b. The maximum and average off-diagonal noise correlation values were calculated, respectively, as 9.5% and 2.0%. The mean value of the SNR measured in the ROI located around the depth of the spinal cord (Figure 4.5b) was found as 81 ± 19.

4.4.3 In Vivo T_2-Weighted Imaging Experiments

After the successful testing of the coil on the phantom, the CSC coil was used to acquire the axial and sagittal T_2-weighted images of the human CSC. The sagittal and axial T_2-weighted images and the SNR maps obtained from a healthy volunteer are, respectively, shown in Figure 4.6 and Figure 4.7, using both the CSC and manufacturer's coils. The values of SNR from the ROIs, which are shown in axial images of Figure 4.6a, were measured as 17.5 ± 2.0, 20.0 ± 3.0, 18.3 ± 2.1, 19.8 ± 2.2, and 22.4 ± 1.8 at C1-C2, C3, C4, C5, and C6 vertebrae, respectively, using the CSC coil. Corresponding SNR values were measured as 11.1 ± 1.5, 13.6 ± 1.7, 9.8 ± 1.2, 12.3 ± 1.3, and 16.0 ± 1.4 using the manufacturer's coil.

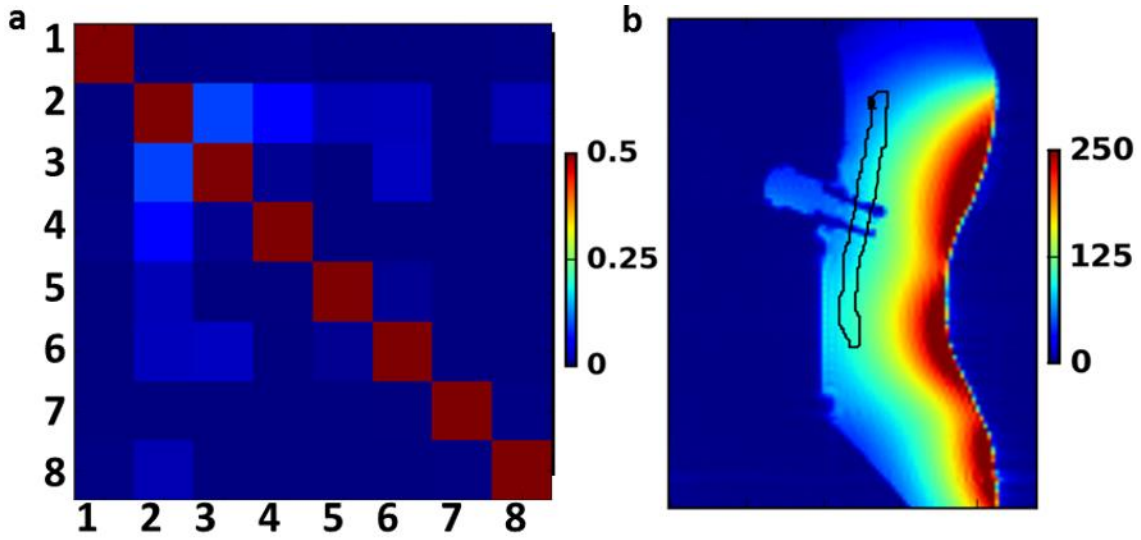

Figure 4.5: Phantom imaging: (a) noise correlation matrix and (b) SNR map of the saline phantom obtained using the CSC coil. The average off-diagonal of the noise matrix was calculated as 2.0%.

Figure 4.6: T_2-weighted imaging: sagittal and axial images of the spinal cord from a volunteer using (a) the CSC coil and (b) the manufacturer's coil (Siemens head, neck, and spine arrays). The locations of the axial slices are shown by the arrows of (a). The black circles in the axial images of (a) are the ROIs drawn for the SNR measurements. The same scale is used for all the images.

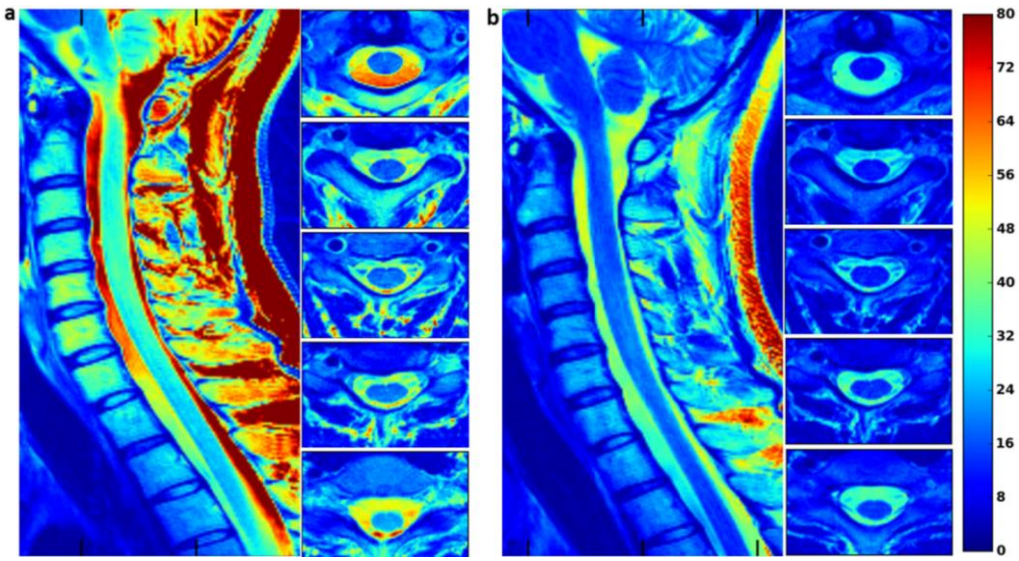

Figure 4.7: T_2-weighted imaging: sagittal and axial SNR maps of the spinal cord from a volunteer using (a) the CSC coil and (b) the manufacturer's coil array (Siemens' head, neck, and spine array). The locations of the axial slices are shown by the arrows in the Figure 4.6(a). The same scale is used for all the images.

4.4.4 In Vivo DTI and Ultrahigh-b Radial DWI Experiments

The source images of DTI with b = 0 s/mm^2 and b = 500 s/mm^2 and the fractional anisotropy (FA) maps calculated from the DW images with 12 diffusion-encoding directions using both the CSC and manufacturer's coils are shown in Figure 4.8a and b. Higher contrast between the white matter and gray matter was observed in the DW images ($b = 500$ s/mm^2) and the FA maps obtained using the CSC coil compared with the manufacturer's coil.

The ultrahigh-b (b = 573, 1702, 2832, 7348 s/mm^2) radial DWI images of the CSC at C4 vertebra obtained using both the CSC and manufacturer's coils are shown in Figure 4.9. The values of the SNR in the white matter region of the DW image (b = 7348 s/mm^2) were measured as 6.2 ± 2.5 and 3.2 ± 1.1, respectively, using the CSC and manufacturer's coils.

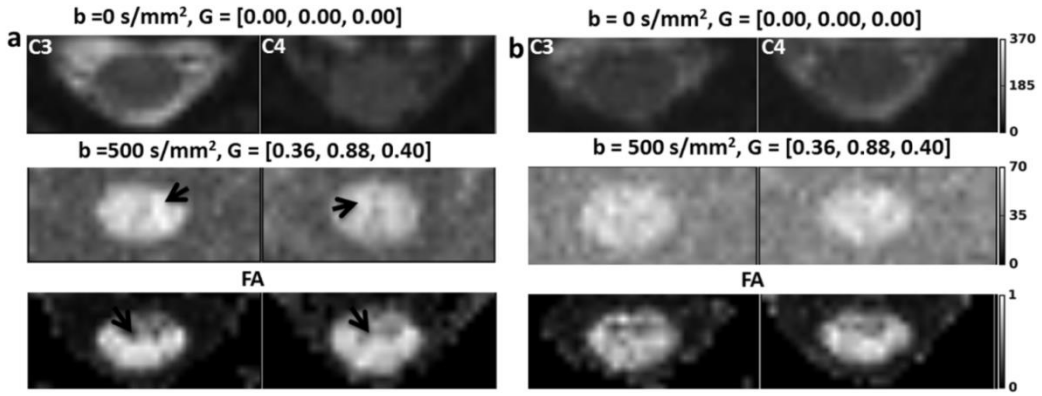

Figure 4.8: DTI: source images with $b = 0$ s/mm^2 and $b = 500$ s/mm^2, and FA maps using (a) the CSC coil and (b) the manufacturer's coil. Black arrow in (a) is pointing to the gray matter structure. Axial slices correspond to C3 and C4 vertebrae. The same scale is used in each row.

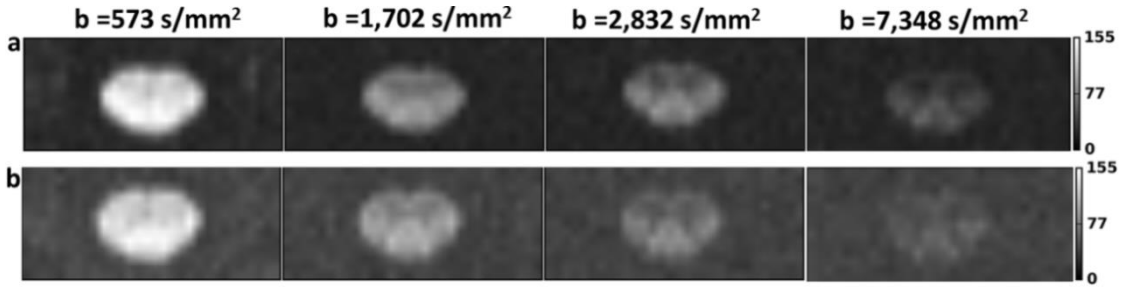

Figure 4.9: Ultrahigh-b radial DWI: Images for different b-values using (a) the CSC coil and (b) the manufacturer's coil. The same scale is used in each row.

4.5 Discussion

We presented an eight-channel CSC coil, which does not require preamp decoupling, for the imaging of the human cervical spinal cord. The adjacent elements of the six-channel posterior array were geometrically decoupled and most nonadjacent elements were decoupled using the loop and butterfly elements. The largest coupling between the nonadjacent elements of the posterior array was -16 dB ($C1 - C3$). The isolation less than -12 dB has been considered as an acceptable isolation between two

elements in a receive-only array (67). The similar sensitivity map between the conventional loop-loop pair and the proposed loop-butterfly pair suggests the comparable performance of the proposed design compared with the conventional design. However, the conventional design requires a complicated matching circuit and an extra phase shifting circuit. The Q-ratio of the anterior elements was lower than posterior elements because the anterior elements do not fit closely to the anterior part of the neck, and hence, there is less loading effect. The anterior frame was intentionally kept a little far away (~ $2-4$ cm) for the subject's comfort. The elements of the noise correlation matrix are smaller than 9.5% in the phantom experiment, which demonstrated that the elements in the CSC coil are lightly coupled. In-vivo SNR improvement of the CSC coil was $1.4-2.0$ times over the manufacturer's coil in the T_2-weighted images at the different levels of the CSC vertebrae.

DTI has emerged as a robust technique for the evaluation of a variety of spinal cord diseases; however, DTI of the spinal cord is problematic because of the small size of the cord and the large nonlinear local magnetic field inhomogeneity induced by the vertebrae (138). The recently developed acquisition techniques (94,138) reduce the distortion induced on the image caused by the local field inhomogeneity; however, these techniques always suffer from the low SNR of the CSC. Therefore, a high SNR CSC dedicated coil is required to use these techniques for the CSC imaging. Images with higher SNR and reduced distortion were obtained in the DTI of the CSC using the CSC coil compared with the manufacturer's coil. The fraction of the restricted compartment in the white matter can be estimated using ultrahigh-b radial DWI which can be a biomarker for the characterization of the white matter (77,78). The 2.0 times SNR improvement in

the ultrahigh-b radial DWI was measured from the white matter region of the ultrahigh-b ($b = 7348$ s/mm^2) DW images using the CSC coil compared with the manufacturer's coil. Almost no signal was left in the gray matter region at the very high b-value (b = 7348 s/mm^2), therefore, the value of SNR was measured only from the white matter region.

The eight-channel CSC coil covers the spinal cord from the brain stem down to T3-T5 vertebrae level, which is greater coverage compared with the C-spine covered by the 12-channel spine elements of the 32-channel head and spine array (128). The coverage can be extended further down by adding more elements along the cord. The design is not necessarily limited to the eight-channel, the number of elements can be increased; however, the butterfly-loop pair should be extended along the z-axis (B_0 field direction).

4.6 Conclusions

An eight-channel CSC dedicated receive-only coil, which does not require preamp decoupling, was designed and tested on the bench. The coil was also validated on a neck-shaped phantom and demonstrated in healthy human CSC imaging. The novel CSC coil, without the preamp decoupling technique, greatly reduced the burden in an array design by using ubiquitous 50 Ω preamplifiers. The eight-channel CSC array does not require a phase shifter and cumbersome matching circuit as in the array that utilizes the preamp decoupling technique to reduce the coupling between the nonadjacent elements. The improved SNR of the new CSC coil provided superior T_2-weighted images of the CSC compared with the manufacturer's coil. The CSC images with reduced

distortion and higher SNR were obtained in the DTI and ultrahigh-b radial DWI experiments using the new CSC coil. The number of channels in the array can be increased by extending more loop-butterfly pairs along the B_0 field direction.

CHAPTER 5

TWO-DIMENSIONAL SINGLE-SHOT DIFFUSION-WEIGHTED STIMULATED EPI WITH REDUCED FOV FOR ULTRA-HIGH-B RADIAL DIFFUSION-WEIGHTED IMAGING OF SPINAL CORD

This chapter is adapted from a paper entitled "Two-dimensional single-shot diffusion-weighted stimulated EPI with reduced FOV for ultrahigh-b radial diffusion-weighted imaging of spinal cord"authored by Nabraj Sapkota, Xianfeng Shi, Lubdha M. Shah, Erica F. Bisson, John W. Rose, and Eun-Kee Jeong. The paper has been published online in the journal of Magnetic Resonance in Medicine (MRM) in June 2016.

5.1 Abstract

High-resolution diffusion-weighted imaging (DWI) of the spinal cord (SC) is problematic because of the small cross-section of the SC and the large field inhomogeneity. Obtaining the ultrahigh-b DWI poses a further challenge. The purpose of the study was to design and validate 2D single-shot diffusion-weighted stimulated echo planar imaging with reduced field of view (2D ss-DWSTEPI-rFOV) for ultrahigh-b radial DWI (UHB-rDWI) of the SC. A novel time-efficient 2D ss-DWSTEPI-rFOV sequence was developed based on the stimulated echo sequence. Reduced-phase field of view was

obtained by using two slice-selective 90° radiofrequency pulses in the presence of the orthogonal slice selection gradients. The sequence was validated on a cylindrical phantom and demonstrated on SC imaging. Ultrahigh-b radial diffusion-weighted (b_{max} = 7,300 s/mm^2) images of the SC with greatly reduced distortion were obtained. The exponential plus constant fitting of the diffusion-decay curve estimated the constant fraction (restricted water fraction) as 0.36 ± 0.05 in the SC white matter. A novel 2D ss-DWSTEPI-rFOV sequence has been designed and demonstrated for high-resolution UHB-rDWI of localized anatomic structures with significantly reduced distortion induced by nonlinear static field inhomogeneity.

5.2 Introduction

Magnetic resonance imaging (MRI) is commonly used for spinal cord (SC) imaging because of its high soft-tissue contrast and noninvasiveness; however, the conventional MRI techniques such as T_1- and T_2-weighted imaging are generally unable to detect lesions in early stages (111). An advanced imaging technique, diffusion tensor imaging (DTI), has emerged as a robust technique for the evaluation of a variety of SC diseases such as multiple sclerosis (7,142) and SC injury (143). The axial and radial diffusivities obtained from the DTI have been increasingly utilized as potential surrogate measures of axon and myelin injuries. Unfortunately, the diffusivity measures derived from the DTI are not always consistent and successful at detecting abnormalities (7,8). Use of another advanced MRI technique, high-b diffusion-weighted imaging (DWI), has been evolving for neural tissue imaging because it provides enhanced contrast between white matter (WM) and gray matter (GM) (73) and detects additional subtle WM lesions

(75,76). Ultrahigh-b radial DWI (UHB-rDWI), i.e., DWI with the ultrahigh-b diffusion-weighting in the direction perpendicular to the fibers, can be used to estimate the restricted compartment in WM, which may be considered as a biomarker for the characterization of the WM (77,78). Our previous report (110), which was based on Monte Carlo simulation and UHB-rDWI experiments in ex vivo SC WM, demonstrated that the signal from restricted space (axonal) remains almost constant while signal from hindered space (outside of axons) decays with increasing b-value. The Monte Carlo simulation indicated that the total signal (sum of the signals from the restricted and hindered spaces) remains constant for b values greater than 5000 s/mm^2 as the signal from the hindered space dies out completely at about b = 5000 s/mm^2. The constant signal measured in the ultrahigh-b region (b > 5000 s/mm^2) may be used to characterize the WM.

Although ultrahigh-b DWI of the SC can provide valuable information to evaluate WM, obtaining ultrahigh-b DWI with b-value greater than 5000 s/mm^2 is challenging using the conventional diffusion-weighted spin echo (DWSE) acquisition technique. Because of the limited gradient strength in most clinical MRI systems, ultrahigh-b DWI requires long echo-time, TE (26). For instance, TE of 133 ms is required to achieve b = 4000 s/mm^2 with gradient strength 40 mT/m using diffusion-weighted (DW) TRSE (twice-refocused spin-echo) (144) in our current whole-body MRI system. Therefore, DWSE imaging is not suitable for UHB-rDWI. To overcome the problem of the signal loss due to long TE in DWSE imaging, diffusion-weighted stimulated echo (DWSTE) imaging has been used (77,78,102) for UHB-rDWI. DWSTE imaging is especially suited for tissues with $T_1 >> T_2$ and short T_2 compared with TE, such as muscle (145,146) and

cartilage (147). DWSTE imaging becomes more beneficial over DWSE imaging at higher field (> $3T$), because the T_2 of water protons decreases and T_1 increases as the field strength increases. Fixation of tissues further lowers the value of T_2 (148) and decreases the diffusivity (100). Therefore, DWSTE may also be beneficial in ultrahigh-b DWI of ex-vivo tissue (52,149). DWSTE imaging is also essential where the validation of the short gradient pulse (SGP) approximation, i.e., short diffusion pulse and long diffusion time, is required, as in q-space (35) and AxCaliber (37) imaging.

High-resolution DWI of the SC is problematic because of the small cross-section of the SC and the large field inhomogeneity in the static field (B_0) created by the magnetic susceptibility change at the tissue–bone interfaces (138). The field inhomogeneity induces distortion in the conventional 2D single-shot diffusion-weighted EPI (2D ss-DWEPI) images, and the distortion increases with increased in the spatial resolution. The distortion can be reduced by effectively reducing the field of view (FOV) in the phase-encoding direction, thereby reducing the off-resonance induced artefacts. However, reducing the FOV smaller than object size in the phase-encoding direction induces wraparound artefact in the image. To overcome this problem of wraparound artefact caused by reduced-phase FOV, several methods such as 2D radiofrequency (RF) excitation along with 180° refocusing (150), zoom-EPI (151), outer volume suppression (152), and double 180° refocusing along the phase-encoding direction (138) have been proposed for DWSE imaging. However, to our knowledge, no reduced-phase FOV technique has been implemented in DWSTE imaging. For reliable DWI of SC, the source DW images must also be free from motion-induced artefact, which requires a single-shot acquisition such as ss-DWEPI (153).

In this work, we present a novel time-efficient acquisition technique, two-dimensional single-shot DW stimulated EPI with reduced-phase FOV (2D ss-DWSTEPI-rFOV), which is based on the STE sequence proposed by Soellinger et al. (154) in their bound-pool water fraction measurement scheme. Further improvement on the previous design was made by grouping the slices into three interleaved groups. The variation in b-value is obtained by varying the mixing time (TM), and hence, the diffusion time. The new sequence was validated on a cylindrical phantom and demonstrated on human cervical spinal cord (CSC) imaging.

5.3 Methods

5.3.1 Pulse Sequence Description

The schematic diagram of 2D ss-DWSTEPI-rFOV is shown in Figure 5.1a, which was described in detail by Jeong et al. (138). In brief, the reduced FOV in the phase-encoding direction was obtained by using two slice-selective 90° RF pulses in the presence of the orthogonal slice selection gradients (G_{SS}) (155). The evolution of magnetization in the 2D ss-DWSTEPI-rFOV is depicted in Figure 5.1b. First, the 90°_{SS} RF pulse with the G_{SS} in the slice direction flips the longitudinal magnetization within the entire imaging volume to the transverse plane, and then the 90°_{PE} RF pulse with the G_{SS} in the phase-encoding direction prepares the magnetization from the entire slice but limited phase FOVs (light gray region in Figure 5.1b). After the 90°_{PE} RF pulse, $90^{\circ}_{S1,}90^{\circ}_{S4,}\dots,90^{\circ}_{S19}$ RF pulses with the G_{SS} in the slice direction were applied at the different mixing times, respectively, to the slices 1, 4, …, 19 (dark gray region in Figure 5.1b) to flip the prepared magnetization down to the transverse plane.

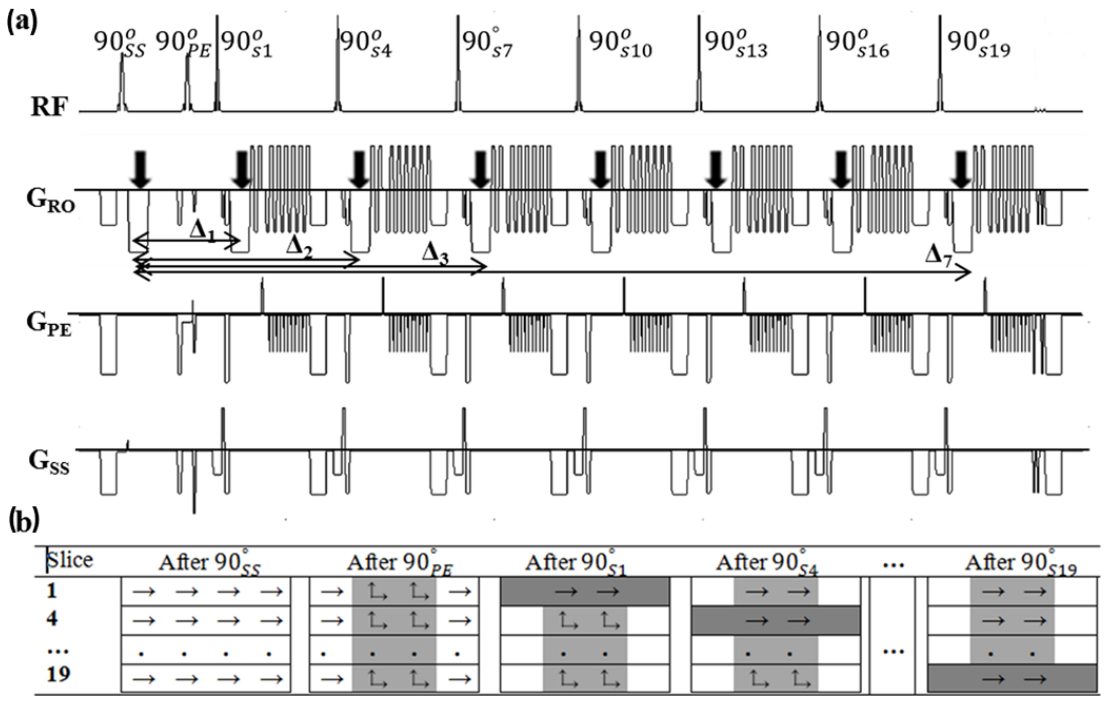

Figure 5.1:(a) Pulse-sequence diagram of 2D ss-DWSTEPI-rFOV. (b) Evolution of magnetization after each RF pulse. In (a), down-pointing arrows represent diffusion gradients G_D and $\Delta_1, \Delta_2, \ldots, \Delta_7$ represent seven diffusion times available for the slice permutation. The length of the arrow in (b) is arbitrary and does not represent the magnitude of magnetization. Imaging schemes for a group of seven slices among 21 total slices are shown.

The slice ordering scheme is based on a technique that is used for measuring the bound-pool water fraction (154). The entire slices are divided into three interleaved groups as shown in Figure 5.2. The experiment is repeated n times (number of slices per group) permuting the slice orders such that images from each slice are acquired for all TMs. Generally, RF pulses ($90^\circ_{S1,} 90^\circ_{S4,} \ldots 90^\circ_{S19,} \ldots$) are not perfectly rectangular in the frequency domain, and the RF pulse applied for a particular slice may also affect magnetization of the neighboring slices, which causes an unnecessary signal drop in the measurement, and hence, introduces error in the quantification. Therefore, the multislice group is essential to avoid the RF leaking into the adjacent slices. The multislice group is

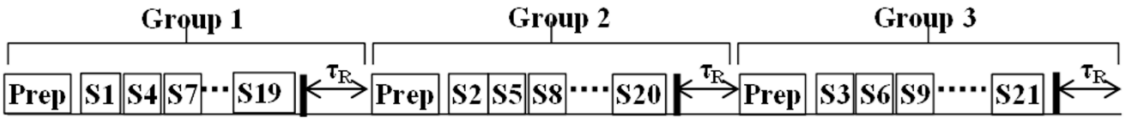

Figure 5.2: Timing diagram for the slice ordering in 2D ss-DWSTEPI-rFoV imaging with 21 total slices. The prep block ($90^{o}_{SS} - G_D - 90^{o}_{PE}$) prepares magnetization from the total phase and slice FOVs. Images of the slices belonging to group 1 (slices 1, 4, 7, 11, 15, and 19) were acquired subsequently with different T_Ms. The τ_R(~2 ms) represents recovery time before the magnetization from the same phase, and slice FOVs are prepared to acquire the images of the slices belonging to group 2 and so on.

also crucial in the imaging of more than 10 slices to keep the values of TM in the range of 0–500 ms; otherwise, TM would be significantly long and the signal decays heavily during the long TM due to the T_1 decay. For instance, the values of TM without multislice grouping ranges from 0 to 700 ms for 10 slices, 0 to 1000 ms for 15 slices, and 0 to 1500 ms for 21 slices. Three nonselective 90° pulses may also be applied at the end of each slice group (not shown in figure) to saturate all longitudinal magnetization so that each slice in every repetition will have the same longitudinal magnetization. The saturation pulse eliminates the error caused by different T_1 recovery of the longitudinal magnetization at the different TMs.

5.3.2 Correction for T_1 Decay

The longitudinal magnetization, which is prepared and restored by the first two 90° RF pulses as shown in Figure 5.1, undergoes an exponential decay of $1/T_1$ during the mixing time even without diffusion-weighting. The exchange between the free- and bound-pool water molecules further increases the decay with an additional rate η. Therefore, the apparent decay rate becomes $1/T_1' = 1/T_1 + \eta$ (154).

The multiple b-value DW images were acquired by increasing TM. Since the b-value is increased by increasing TM, the signal decays due to T_1' decay as well as diffusion decay (T_1'-diffusion decay) as given by the equation

$$S_{T_1'-diff} = S_o \exp(-bD) \exp\left(-\frac{TM}{T_1'}\right) \quad [5.1]$$

where S_o is the signal measured without T_1' and diffusion decay, $b = \gamma^2 G_D^2 \delta^2 (\Delta - \frac{\delta}{3})$; γ is a gyromagnetic ratio, and $G_D, \delta,$ and Δ are the amplitude, duration, and separation of the diffusion-weighting gradient pair. T_2 decay is included in S_o and is constant for all b-values because T_E is fixed for all b-values.

In the absence of diffusion-weighting, the signal decays due to only the T_1' decay and is given by the equation

$$S_{T_1'} = S_o \exp\left(-\frac{TM}{T_1'}\right) \quad [5.2]$$

The effect of T_1' decay from the T_1'-diffusion decay can be removed by dividing the signal measured with diffusion-weighting by the signal measured without diffusion-weighting at the same TM. The signal decay due to only the diffusion decay can be obtained by dividing Eq. [5.1] by Eq. [5.2] and is given by the equation

$$S_{diff} = \exp(-bD) \quad [5.3]$$

where $S_{diff} = S_{T_1'-diff}/S_{T_1'}$ is the signal measured at a particular b-value under pure diffusion decay.

The signal decay curves measured with and without diffusion-weighting are, respectively, called the T_1'-diffusion-curve and T_1'-curve. The T_1'-diffusion-curve undergoes T_1' decay as well as diffusion decay whereas the T_1'-curve undergoes only T_1'

decay. When the T_1'-diffusion-curve is divided by the T_1'-curve measured for the same values of TM, the new curve called the diffusion-curve, is obtained, which undergoes only the diffusion decay. Dividing the T_1'-diffusion-curve by the T_1'-curve often introduces fluctuations into the diffusion-curve, particularly at the ultrahigh-b diffusion-weighting, where the signal-to-noise ratio is low. Therefore, to get a smooth diffusion-curve, the T_1'-diffusion-curve is divided by a curve obtained by fitting the T_1'-curve with an appropriate fitting function, for instance, a monoexponential function in phantom imaging and bi-exponential function in human SC in vivo imaging (154).

5.3.3 MRI Experiments

Imaging studies of the 2D ss-DWSTEPI-rFOV pulse sequence were performed on a 3 T clinical MRI system (Trio, Siemens Medical Solutions, Erlangen, Germany) equipped with maximum gradient strength of 40 mT/m and gradient slew rate of 200 mT/m/s. The pulse sequence was developed using the Integrated Development Environment for Applications (IDEA) pulse sequence development environment.

5.3.3.1 Phantom experiment. Axial images of a cylindrical phantom filled with saline, doped with 0.1 nM $MnCl_2$, were acquired using 2D ss-DWSTEPI-rFOV at room temperature. The following imaging parameters were used: TE = 64 ms, TR = 3.0 s, read FOV = 256 mm, phase FOV = 88 mm, slice thickness = 4 mm, number of slices = 21, acquisition matrix = 128 × 44. Seven different b-values (b_{max} = 591 s/mm^2) were obtained by applying the constant diffusion gradient (duration – δ = 12 ms and strength – G_D = 11 mT/m) along the read-out (left-right) direction for the seven different TMs ranging from 9 to 465 ms. The b_0 (b = 0 s/mm^2) images were also obtained without

diffusion-weighting for the corresponding TMs. Total imaging time for both b_0 and DW images was 10 min 30 s.

5.3.3.2 In vivo experiment. After approval was obtained from the Institutional Review Board, in vivo imaging of a volunteer who provided informed consent was performed. The 2D ss-DWSTEPI-rFOV technique was used to acquire axial DW images of the CSC using a home-built eight-channel, receive-only CSC array. The imaging parameters used were the same as those for the phantom studies except read FOV = 128 mm, phase FOV = 44 mm, and b values in the range of 0–7300 s/mm^2. Seven different b-values (b_{max} = 7300 s/mm^2) were obtained by applying the constant diffusion gradient (δ = 12 ms and G_D = 38 mT/m) along the read-out direction (radial DWI) for seven different TMs ranging from 9 to 465 ms. The b_0 images were also obtained without diffusion-weighting for the corresponding TMs.

5.4 Results

5.4.1 Phantom Experiment

The b_0 and DW images obtained from the phantom using the 2D ss-DWSTEPI-rFOV technique for different TMs (i.e., 9, 237, and 465 ms) are shown in Figure 5.3a-b. A typical T_1'-curve obtained from a region of interest (ROI) is shown in Figure 5.3c. The T_1'-curve decays monoexponentially with TM, and hence, is fitted with the mono-exponential function (Eq. [5.2]) because the water molecules in the phantom have single T_1 value with $\eta = 0$. The monoexponential fitting of the T_1'-curve estimated the value of T_1' as 976 ± 2 ms. A typical T_1'-diffusion-curve obtained from the same ROI is also shown in Figure 5.3c. The diffusion-curve, which undergoes only the diffusion decay, was

obtained by dividing the T_1'-diffusion-curve by the fitted T_1'-curve (dashed line passing through square symbols in Figure 5.3c) and is also shown in Figure 5.3c. The diffusion of the water molecules in the phantom is free diffusion, and hence, the signal decay due to diffusion of molecules must be monoexponential (Eq. [5.3]). The diffusion-curve was fitted with the monoexponential function. The monoexponential fitting of the diffusion-curve estimated the diffusivity of the water molecules as (2.51 ± 0.03) $\times 10^{-3}$ mm^2/s.

5.4.2 In Vivo Experiment

The in vivo b_0 images and DW images of the human CSC obtained using the 2D ss-DWSTEPI-rFOV sequence for different values of TMs are shown in Figure 5.4a-b. Typical T_1'-curves obtained from WM and GM pixels (1 mm × 1 mm × 4 mm) of the CSC at the C3 vertebra level are shown in Figure 5.4c-d. The T_1'- curves were fitted with the bi-exponential function as suggested by Soellinger et al. (154) in their bound-pool water fraction measurement. Typical T_1'-diffusion-curves obtained from a WM and GM pixels (1 mm × 1 mm × 4 mm) of the CSC at the level of C3 vertebra are also shown in Figure 5.4c-d. The diffusion-curve for each WM and GM pixel, which undergoes only the diffusion decay, was obtained dividing the corresponding T_1'-diffusion-curve by the fitted T_1'-curve (dashed line passing through square symbols in Figure 5.4c-d) and are also shown in Figure 5.4c-d. The radial DW signal measured in WM is mainly the sum of the constant signal from the restricted space (axonal) and approximately monoexponentially decaying signal from hindered space (110); therefore, the radial diffusion-curve may be fitted with exponential plus constant fitting function (49,78). The exponential plus constant fitting of the diffusion-curve estimated the constant fraction as

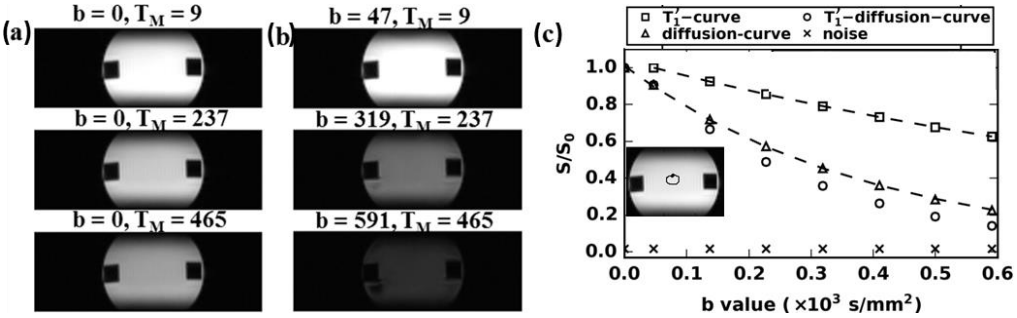

Figure 5.3: Phantom imaging: (a) b_0 images; (b) DW images; and (c) typical signal decay curves (T_1'-curve, T_1'-diffusion-curve, and diffusion-curve) obtained from a ROI. In (c), the dashed lines passing through square symbols and triangle symbols represent the monoexponentially fitted T_1'-curve and diffusion-curve, respectively. The T_1'-curve in (c) is plotted against TMs = 9, 85, 161, 237, 313, 389, and 465 ms, but TMs are not displayed on the horizontal axis.

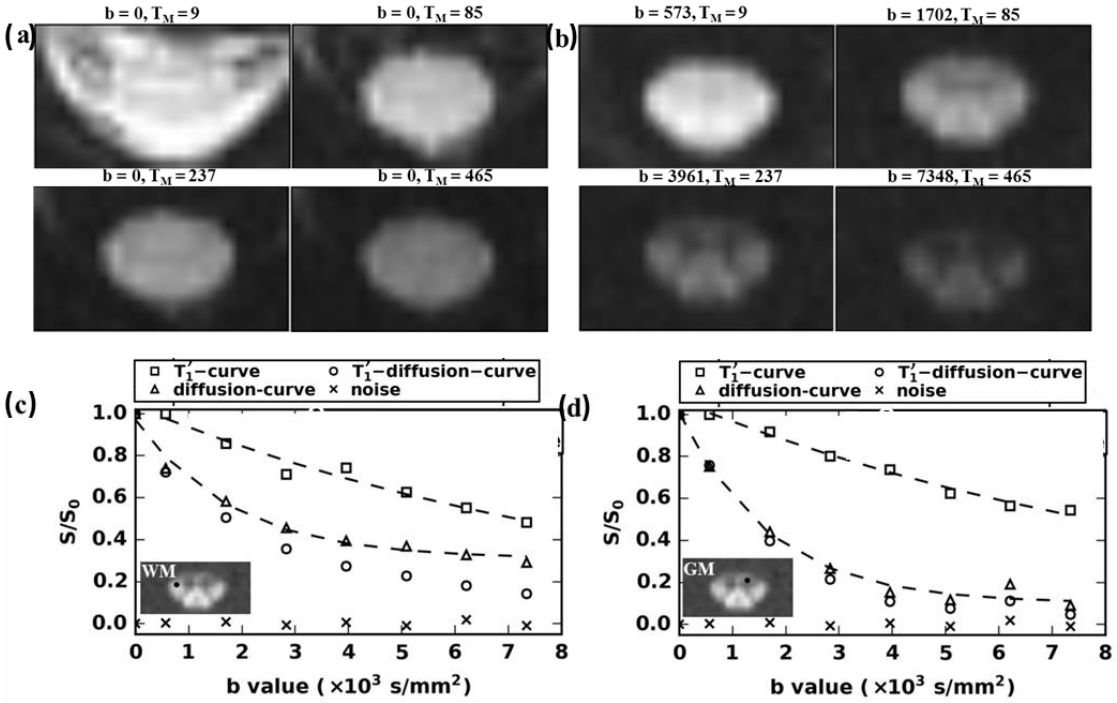

Figure 5.4: In vivo imaging: (a) b_0 images, (b) DW images, and (c-d) typical signal decay curves (T_1'-curve, T_1'-diffusion-curve, and diffusion-curve) from WM and GM pixels of the CSC at C3 vertebra level, respectively. Dashed lines in (c-d) represent the bi-exponential fitting of the T_1'-curve (line passing through the square symbols) and exponential plus constant fitting of the diffusion-decay curve (line passing through the triangle symbols). T_1'-curves in (c-d) are plotted against TMs = 9, 85, 161, 237, 313, 389, and 465 ms, but TMs are not displayed on the horizontal axis.

0.32 ± 0.03 in a WM pixel with the decaying fraction and diffusivity, respectively, as 0.68 ± 0.02 and (0.55± 0.08) $\times 10^{-3}\ mm^2/s$. The constant fraction in the exponential plus constant fitting may represent fraction of restricted water (axonal fraction) in the WM (110). The map of the restricted water fraction obtained from a 4-mm-thick slice (C3) is shown in Figure 5.5. The average values of the fraction measured in ROIs shown in Figure 5.5 were 0.36 ± 0.05 (ROI1) and 0.37 ± 0.08 (ROI2) in lateral WM columns.

5.5 Discussion

The diffusivity of the water molecules in the phantom was estimated as (2.51 ± 0.03) × $10^{-3}\ mm^2/s$, which is slightly higher than the reported value of the self-diffusion coefficient of water molecules, which is noted as 2.30 × $10^{-3}\ mm^2/s$ at $25°C$ (156,157). The higher values of diffusivity estimated may be due to additional translational motion of water molecules associated with the table vibration during the application of diffusion-weighting gradient.

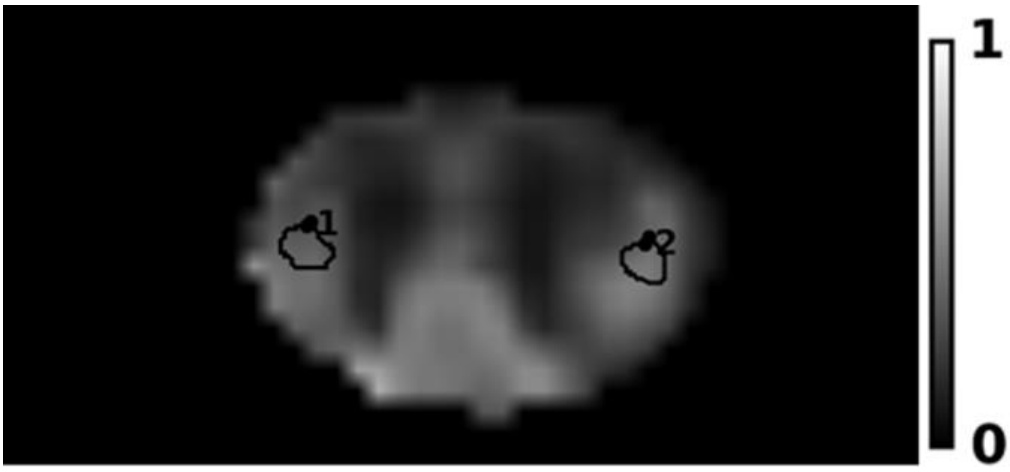

Figure 5.5: Restricted water fraction map for an axial slice of the CSC at the level of the C3 vertebra.

The T_1'-curve in neural tissues (WM and GM) is complex and deviates from the monoexponential decays. The T_1'-curve was fitted with a bi-exponential function as described by Soellinger et al. and Ropele et al. (154,158). The diffusion of the water molecules in biological tissue is also intricate and difficult to interpret. However, the Monte Carlo simulation of water diffusion in WM and ultrahigh-b study of the ex-vivo CSC demonstrated almost constant signal from the axonal space and approximately monoexponentially decaying signal from the space outside the axons when the diffusion gradient was applied perpendicular to the CSC (110). The signal remaining in the ultrahigh-b (> 5000 s/mm^2) region may represent restricted water in axons, and the decay rate, if any exists, may indicate the degree of demyelination. Signal from the myelin space is considered to be negligible because of the very short T_2 of water molecules in myelin space compared with T_E. Therefore, the diffusion-decay curve was fitted with the exponential plus constant function and a constant component was assigned to axonal space as described by Sapkota et al. (110). In this study, the mean value of the restricted water fraction at the C3 vertebra level was estimated as 0.36 ± 0.05 in the lateral WM columns (ROIs shown in Figure 5.5), which agreed well with the previously reported average value of 0.34 ± 0.08 (78) from anterior, posterior, and lateral WM columns using 10 in vivo studies of the human CSC at the C4-C5 vertebra level (TM = 500 ms, b_{max} = 7350 s/mm^2). More in vivo studies should be conducted to validate the restricted water fraction estimated in this work.

Unlike conventional DWSTE (102), the 2D ss-DWSTEPI-rFOV sequence does not waste the long TM (> 250 ms) to acquire images from a single slice, but rather acquires images from all slices of a specific slice group within the TM. Therefore, the

time efficiency using the new sequence was greatly improved, which results in improving the signal-to-noise ratio of the measurement for a fixed acquisition time. Furthermore, implementation of the reduced FOV scheme described in this work is more beneficial in the new sequence as the first 90° RF pulse flips the magnetization from total slice FOV and the second 90° RF pulse with G_{SS} in the phase-encoding direction prepared magnetization from total slice and phase FOVs. The magnetization from the slice and phase FOVs is prepared once while imaging a group of slices. In conventional DWSTE, the three slice-selective 90° RF pulses are applied on each slice while imaging the slice. The second 90° RF pulse is applied with the G_{SS} in the phase-encoding direction for the reduced-phase FOV imaging, which flips the magnetization to the transverse plane in and out of the imaging slice. The repeated application of the second 90° RF pulse for the imaging of each slice continuously decreases the initial longitudinal magnetization (138).

In this study, variation in b-values is achieved by varying the mixing time, and hence, the diffusion time. The 2D ss-DWSTEPI-rFOV sequence is beneficial only if the DW images with multiple b-values are needed. In 2D ss-DWSTEPI-rFOV images, the signal decays because of the combined effect of the T_1' decay as well as diffusion decay. To remove the effect of the T_1' decay from the experimentally measured T_1'-diffusion-decay curve, a set of b_0 images for all TMs should be acquired, which adds an extra effort in data acquisition and post-processing. However, the b_0 images may also be used to calculate bound-pool water fraction to evaluate the myelination in WM as described by Soellinger et al. (154). Some applications such as q-space imaging (159) require the variation in b-value by increasing diffusion gradient strength rather than the diffusion time as demonstrated here. The variation in b-value can also be achieved by increasing

gradient strength in the 2D ss-DWSTEPI-rFOV imaging; however, different slices would have different $T_M s$, and hence, the different sets of b-values. The slices should not be permuted between measurements to keep the mixing time (diffusion time) constant.

At present, only a limited number of clinical whole-body MRI systems are equipped with increased gradient strength, such as 80 mT/m. High-b DWI (b = ~ 4000 s/mm^2) can be measured with moderate T_2 signal loss using DWSE; however, DWSTE can still offer a benefit by acquiring even higher b-values for rDWI to assure complete suppression of the signal from the hindered water such as extra-axonal water. The benefit of DWSTE for UHB- rDWI using this increased gradient strength needs to be analyzed.

5.6 Conclusions

A novel 2D ss-DWSTEPI-rFOV sequence for the ultrahigh-b DWI with reduced FOV scheme was successfully designed and demonstrated in the phantom as well as in CSC in vivo imaging. The new sequence can be used to acquire high-resolution ultrahigh-b DW images with higher signal-to-noise ratio from localized anatomic structures such as the SC and the optic nerve with significantly reduced distortion induced by nonlinear static field inhomogeneity.

CHAPTER 6

SUMMARY, CONCLUSIONS, AND FUTURE WORKS

6.1 Summary

With the remarkable advances in hardware and acquisition techniques, to this date, it can be believed that MRI can only be a noninvasive imaging technique for the diagnosis and prognosis of the spinal cord thoroughly. However, MRI of the spinal cord is problematic due to the small area of cross-section, which demands the high-resolution imaging. The conventional imaging methods such as T_1-weighted and T_2-weighted imaging generally underestimate the disease burden because the changes in the conventional imaging methods may appear in the late stages of the disease. Imaging of the spinal cord using the advanced imaging techniques such as diffusion and perfusion MRI is further challenging. The magnetic susceptibility difference between the tissue and bone induces severe geometrical distortion on the images obtained with the conventional single-shot EPI. The involuntary motions of the patient, such as cardiac motion, respiratory movements, carotid, and cerebro-spinal fluid pulsations, induce blurring or ghosting artefacts in the multishot EPI. The chemical-shift effect of the lipids, which is presence in the fatty marrow, may also degrade the accuracy on the quantification of pathologic burden. Besides these technical challenges, the foremost fundamental challenge is in the interpretation of the outcomes of the diffusion MRI of the complex

biological tissues such as WM and GM. To our knowledge, the origin of the signal measured in the diffusion MRI of the WM has not been completely understood yet. This dissertation focuses on the various aspects; first, it contributes significantly towards the understanding of the signal measured in the diffusion MRI of the spinal cord WM by performing the MCS of water diffusion in WM, and analyzing the ultrahigh-b DW images of the excised pig spinal cord. Secondly, the dissertation focuses on the construction of an 8-channel CSC dedicated phased array coil to improve SNR of the CSC images. Finally, it contributes to the design of a time efficient and fast acquisition technique 2D ss-DWSTEPI-rFOV, which acquires stimulated echoes with reduced phase FOV in a single-shot. The single-shot and reduced phase FOV features mitigates the motion and off-resonance related artefacts, respectively.

6.2 Conclusions

The MCS of water diffusion in WM provides adequate knowledge to interpret the signal measured in the diffusion MRI. The results of the MCS predicted that the signal from the EA spaces decreases gradually with increase in b-value. The EA space signal can be suppressed completely with sufficiently high b-value (~20,000 s/mm^2 for our specimen and ~ 5000 s/mm^2 for in vivo CSC). In contrary, the signal from the IA space remained almost constant, independent of b-value. The DW signal behavior in the WM is very intricate and difficult to resolve because of the complex structure of the WM. Therefore, it is essential to suppress the signal from the hindered spaces (EA space) by applying sufficiently high diffusion-weighting. After suppressing the signal from the hindered space, the remaining signal is solely from the restricted (IA) space, which does

not decay with the b-value. The interpretation of the signal from the purely restricted (IA) space is much easier and straight-forward because the signal does not decay with the b-value in an ideal situation. The axonal integrity and intactness may be evaluated more accurately by assessing the signal solely from the restricted space. The radial and axial UHB-DWI of the excised pig spinal cord supported the fact that the restricted signal in the radial DWI is mainly originated from the IA space. The fraction and decay rate (if exists) of the restricted signal in the UHB-region are the two essential hallmarks for the characterization of the WM.

An 8-channel CSC dedicated phased array coil yielded the higher SNR images of the CSC compared with the manufacturer's coil. The array was designed in such way that the mutual interactions between elements were negligible. The negligible mutual interaction between the elements was achieved using the circular and butterfly-shaped elements with appropriate geometrical overlapping. Since the interaction between elements was negligible, the proposed array was constructed without implementing the preamp decoupling technique. The new CSC array design reduces the coil construction burden by eliminating phase shifter and cumbersome matching circuitry, which are required for the array that utilizes the preamplifier decoupling technique. The high-quality T_2-weighted, diffusion tensor, and UHB radial DW images were obtained using the proposed CSC dedicated array coil.

Motion and off-resonance related artefacts were greatly reduced in the human in vivo spinal cord imaging using the proposed acquisition technique 2D ss-DWSTEPI-rFOV. The 2D ss-DWSTEPI-rFOV comes with the fast acquisition (single-shot EPI) and reduced phase FOV schemes to mitigate the motion and off-resonance related artefacts,

respectively. The reduced phase FOV was obtained by applying two slice-selective RF pulses in the presence of the orthogonal slice selection gradients. Furthermore, the 2D ss-DWSTEPI-rFOV sequence is beneficial in terms of the SNR compared with the conventional STE sequence accompanied by the similar reduced phase FOV scheme because the magnetization of a slab (3D) is prepared once while imaging a group of slices in the new sequence. In contrast, the magnetization of a slice (2D) is prepared while imaging each slice in the conventional STE sequence. The repeated application of the RF pulses in the presence of the orthogonal slice selection gradient decreases the magnetization. The new stimulated-echo based DWI sequence also allows choosing a long diffusion time, and hence, a very high b-value without making TE relatively long.

6.3 Future Works

Although the MCS of water diffusion in WM provides in-depth knowledge to interpret the signal measured in the diffusion MRI of healthy spinal cord, the interpretation of the signal measured in the pathologic cord may not be still straight-forward. The current version of MCS software simulates the diffusive motion of the molecules in the WM, which is composed of myelinated cylindrical axons. In the pathologic spinal cord, the microscopic environment may not be the same. The diffusive motion may be hindered (to some degree) even in the axial direction because of the presence of the immune cells and microphases in the EA space. Therefore, the MCS of water diffusion with the various disease conditions, such as axonal beading and the presence of immune cell and microphases in the EA space, may provide the insightful information to the DW signal behavior, which could be used for the diagnosis and

prognosis of the WM diseases. The understanding of the water diffusion in GM may also be an area interest in some cases. Therefore, the MCS of water diffusion in GM can also provide very important information about the pathology. The results of the MCS and findings of UHB-DWI of the specimen with various diseases conditions should be validated with the findings of the immunohistology.

The eight-channel CSC dedicated array coil provided higher SNR compared with the manufacturer's coil; however, an optimal array design (size and number of elements) which yields maximum SNR at the CSC is not exactly known yet. An electromagnetic simulation using Maxwell's equation may predict the optimal size and number of elements of an array which gives the maximum SNR at the CSC. Construction of an array with optimal SNR at the CSC and validation using MRI would be of great interest in the area of CSC coil design.

While measuring a half of the transverse magnetization at the position of the stimulated echo using 2D ss-DWSTEPI-rFOV, another half of the transverse magnetization is wasted at the position of the spin echo. Therefore, acquiring both halves of the magnetization and combining them using an appropriate method is highly essential in order to increase the utility of the 2D ss-DWSTEPI-rFOV sequence.

REFERENCES

1. Schwartz ED, Flanders AE. Spinal trauma: imaging, diagnosis, and management. Wolters Kluwer Health/Lippincott, Willliams & Wilkins; Philadelphia 2007.

2. Knaap MS van der, Valk J. Magnetic resonance of myelination and myelin disorders. Springer Science & Business Media; Berlin 2005.

3. Cohen-Adad J, Wheeler-Kingshott C. Quantitative MRI of the spinal cord. Academic Press; San Diego 2014.

4. Bondurant FJ, Cotler HB, Kulkarni MV, McArdle CB, Harris JH. Acute spinal cord injury. A study using physical examination and magnetic resonance imaging. Spine 1990;15:161–8.

5. Rajasekaran S, Kanna RM, Shetty AP. Diffusion tensor imaging of the spinal cord and its clinical applications. J Bone Joint Surg Br 2012;94:1024–31. doi: 10.1302/0301-620X.94B8.29618.

6. Torrey HC. Bloch equations with diffusion terms. Phys Rev 1956;104:563–565. doi: 10.1103/PhysRev.104.563.

7. Oh J, Zackowski K, Chen M, et al. Multiparametric MRI correlates of sensorimotor function in the spinal cord in multiple sclerosis. Mult Scler 2013;19:427–35.

8. Zollinger LV, Kim TH, Hill K, Jeong EK, Rose JW. Using diffusion tensor imaging and immunofluorescent assay to evaluate the pathology of multiple sclerosis. J Magn Reson Imaging 2011;33:557–64. doi: 10.1002/jmri.22502.

9. Kellogg JMB, Rabi II, Ramsey NF, Zacharias JR. The magnetic moments of the proton and the deuteron. The radiofrequency spectrum of H2 in various magnetic fields. Phys Rev 1939;56:728–743. doi: 10.1103/PhysRev.56.728.

10. Rabi II, Zacharias JR, Millman S, Kusch P. A New method of measuring nuclear magnetic moment. Phys Rev 1938;53:318–318. doi: 10.1103/PhysRev.53.318.

11. Bloch F, Hansen WW, Packard M. The nuclear induction experiment. Phys Rev 1946;70:474–485. doi: 10.1103/PhysRev.70.474.

12. Purcell E, Torrey H, Pound R. Resonance absorption by nuclear magnetic moments in a solid. Phys Rev 1946;69:37–38. doi: 10.1103/PhysRev.69.37.

13. Bloembergen N, Purcell E, Pound R. Relaxation effects in nuclear magnetic resonance absorption. Phys Rev 1948;73:679–712. doi: 10.1103/PhysRev.73.679.

14. Slichter CP. Principles of magnetic resonance. Springer Science & Business Media; Berlin 1996.

15. Damadian R. Tumor detection by nuclear magnetic resonance. Science 1971;171:1151–3.

16. Lauterbur PC. Image formation by induced local interactions: examples employing nuclear magnetic resonance. Nature 1973;242:190–191. doi: 10.1038/242190a0.

17. Mansfield P, Grannell PK. “Diffraction” and microscopy in solids and liquids by NMR. Phys Rev B 1975;12:3618–3634. doi: 10.1103/PhysRevB.12.3618.

18. Kumar A, Welti D, Ernst RR. NMR fourier zeugmatography. J Magn Reson 1975;18:69–83. doi: 10.1016/0022-2364(75)90224-3.

19. Thapa B, Kaggie J, Sapkota N, Frank D, Jeong E-K. Design and development of a general-purpose transmit/receive (T/R) switch for 3T MRI, compatible for a linear, quadrature and double-tuned RF coil. Concepts Magn Reson Part B Magn Reson Eng 2016. doi: 10.1002/cmr.b.21321.

20. Hahn E. Spin echoes. Phys Rev 1950;80:580–594. doi: 10.1103/PhysRev.80.580.

21. Woessner DE. Effects of diffusion in nuclear magnetic resonance spin-echo experiments. J Chem Phys 1961;34:2057. doi: 10.1063/1.1731821.

22. Bernstein MA, King KF, Zhou XJ. Handbook of MRI pulse sequences. Elsevier; Amsterdam 2004. doi: 10.1016/B978-0-12-092861-3.50029-7.

23. Burstein D. Stimulated echoes: description, applications, practical hints. Concepts Magn Reson 1996;8:269–278. doi: 10.1002/(SICI)1099-0534(1996)8:4<269:AID-CMR3>3.0.CO;2-X.

24. Frahm J, Merboldt K, Hänicke W, Haase A. Stimulated echo imaging. J Magn Reson 1985;64:81–93. doi: 10.1016/0022-2364(85)90033-2.

25. Liang Z-P, Lauterbur PC. Principles of magnetic resonance imaging: a signal processing perspective. SPIE Optical Engineering Press; New York 2000.

26. Stejskal EO, Tanner JE. Spin diffusion measurements: spin echoes in the presence of a time-dependent field gradient. J Chem Phys 1965;42:288. doi: 10.1063/1.1695690.

27. Bihan DL, Breton E. Imagerie de diffusion in-vivo par résonance magnétique nucléaire. Comptes-Rendus l’Académie des Sci 1985;93:27–34.

28. Taylor DG, Bushell MC. The spatial mapping of translational diffusion coefficients

by the NMR imaging technique. Phys Med Biol 1985;30:345–9.

29. Merboldt K-D, Hanicke W, Frahm J. Self-diffusion NMR imaging using stimulated echoes. J Magn Reson 1985;64:479–486. doi: 10.1016/0022-2364(85)90111-8.

30. Moseley ME, Kucharczyk J, Mintorovitch J, Cohen Y, Kurhanewicz J, Derugin N, Asgari H, Norman D. Diffusion-weighted MR imaging of acute stroke: correlation with T2-weighted and magnetic susceptibility-enhanced MR imaging in cats. Am J Neuroradiol 1990;11:423–429.

31. Cleveland GG, Chang DC, Hazlewood CF, Rorschach HE. Nuclear magnetic resonance measurement of skeletal muscle: anisotrophy of the diffusion coefficient of the intracellular water. Biophys J 1976;16:1043–53. doi: 10.1016/S0006-3495(76)85754-2.

32. Moseley ME, Cohen Y, Kucharczyk J, Mintorovitch J, Asgari HS, Wendland MF, Tsuruda J, Norman D. Diffusion-weighted MR imaging of anisotropic water diffusion in cat central nervous system. Radiology 1990;176:439–45. doi: 10.1148/radiology.176.2.2367658.

33. Chenevert TL, Brunberg JA, Pipe JG. Anisotropic diffusion in human white matter: demonstration with MR techniques in vivo. Radiology 1990;177:401–5. doi: 10.1148/radiology.177.2.2217776.

34. Basser PJ, Mattiello J, LeBihan D. MR diffusion tensor spectroscopy and imaging. Biophys J 1994;66:259–67. doi: 10.1016/S0006-3495(94)80775-1.

35. Cory DG, Garroway AN. Measurement of translational displacement probabilities by NMR: an indicator of compartmentation. Magn Reson Med 1990;14:435–44.

36. Callaghan PT, Coy A, MacGowan D, Packer KJ, Zelaya FO. Diffraction-like effects in NMR diffusion studies of fluids in porous solids. Nature 1991;351:467–469. doi: 10.1038/351467a0.

37. Assaf Y, Blumenfeld-Katzir T, Yovel Y, Basser PJ. AxCaliber: a method for measuring axon diameter distribution from diffusion MRI. Magn Reson Med 2008;59:1347–54. doi: 10.1002/mrm.21577.

38. Zhang H, Schneider T, Wheeler-Kingshott CA, Alexander DC. NODDI: practical in vivo neurite orientation dispersion and density imaging of the human brain. Neuroimage 2012;61:1000–16. doi: 10.1016/j.neuroimage.2012.03.072.

39. Wang MC, Uhlenbeck GE. On the theory of the brownian motion II. Rev Mod Phys 1945;17:323–342. doi: 10.1103/RevModPhys.17.323.

40. Price WS. Pulsed-field gradient nuclear magnetic resonance as a tool for studying translational diffusion: Part 1. Basic theory. Concepts Magn Reson 1997;9:299–336. doi: 10.1002/(SICI)1099-0534(1997)9:5<299::AID-CMR2>3.0.CO;2-U.

41. Carr H, Purcell E. Effects of Diffusion on free precession in nuclear magnetic resonance experiments. Phys Rev 1954;94:630–638. doi: 10.1103/PhysRev.94.630.

42. Fick A. On liquid diffusion. J Memb Sci 1995;100:33–38.

43. Stejskal EO. Use of spin echoes in a pulsed magnetic-field gradient to study anisotropic, restricted diffusion and flow. J Chem Phys 1965;43:3597. doi: 10.1063/1.1696526.

44. Tanner JE, Stejskal EO. Restricted self-diffusion of protons in colloidal systems by the pulsed-gradient, spin-echo method. J Chem Phys 1968;49:1768. doi: 10.1063/1.1670306.

45. Balinov B, Jonsson B, Linse P, Soderman O. The NMR self-diffusion method applied to restricted diffusion. simulation of echo attenuation from molecules in spheres and between planes. J Magn Reson Ser A 1993;104:17–25. doi: 10.1006/jmra.1993.1184.

46. Söderman O, Jönsson B. Restricted diffusion in cylindrical geometry. J Magn Reson Ser A 1995;117:94–97. doi: 10.1006/jmra.1995.0014.

47. Szafer A, Zhong J, Gore J. Theoretical model for water diffusion in tissues. Magn Reson Med 1995;33:697–712.

48. Hall MG, Alexander DC. Convergence and parameter choice for Monte-Carlo simulations of diffusion MRI. IEEE Trans Med Imaging 2009;28:1354–64. doi: 10.1109/TMI.2009.2015756.

49. Peled S. New perspectives on the sources of white matter DTI signal. IEEE Trans Med Imaging 2007;26:1448–55. doi: 10.1109/TMI.2007.906787.

50. Ford JC, Hackney DB. Numerical model for calculation of apparent diffusion coefficients (ADC) in permeable cylinders--comparison with measured ADC in spinal cord white matter. Magn Reson Med 1997;37:387–94.

51. Ford JC, Hackney DB, Lavi E, Phillips M, Patel U. Dependence of apparent diffusion coefficients on axonal spacing, membrane permeability, and diffusion time in spinal cord white matter. J Magn Reson Imaging 1998;8:775–82.

52. Stanisz GJ, Szafer A, Wright GA, Henkelman RM. An analytical model of restricted diffusion in bovine optic nerve. Magn Reson Med 1997;37:103–11.

53. Ford JC, Hackney DB, Lavi E, Phillips M, Patel U. Dependence of apparent diffusion coefficients on axonal spacing, membrane permeability, and diffusion time in spinal cord white matter. J Magn Reson Imaging 1998;8:775–782. doi: 10.1002/jmri.1880080405.

54. Xing H, Lin F, Wu Q, Gong Q. Investigation of different boundary treatment methods in Monte-Carlo simulations of diffusion NMR. Magn Reson Med 2013;70:1167–72. doi: 10.1002/mrm.24551.

55. Roemer PB, Edelstein WA, Hayes CE, Souza SP, Mueller OM. The NMR phased array. Magn Reson Med 1990;16:192–225. doi: 10.1002/mrm.1910160203.

56. Hayes CE, Hattes N, Roemer PB. Volume imaging with MR phased arrays. Magn Reson Med 1991;18:309–319. doi: 10.1002/mrm.1910180206.

57. Kumar A, Edelstein WA, Bottomley PA. Noise figure limits for circular loop MR coils. Magn Reson Med 2009;61:1201–9. doi: 10.1002/mrm.21948.

58. Rivera M, Vaquero JJ, Santos A, Ruiz-Cabello J, del Pozo F. MRI visualization of small structures using improved surface coils. Magn Reson Imaging 1998;16:157–66.

59. Murphy MK, Frnandez EJ, Clark DS. A comparison of three radiofrequency coils for NMR studies of conductive samples. Magn Reson Med 1989;12:382–389. doi: 10.1002/mrm.1910120311.

60. Decorps M, Blondet P, Reutenauer H, Albrand J, Remy C. An inductively coupled, series-tuned NMR probe. J Magn Reson 1985;65:100–109. doi: 10.1016/0022-2364(85)90378-6.

61. Li L, Kruger RA. An electrodeless measuring technique for determining conductivity of biological tissues at radio frequencies. Phys Med Biol 1988;33:1443–1452. doi: 10.1088/0031-9155/33/12/009.

62. Hoult DI. The principle of reciprocity in signal strength calculations?A mathematical guide. Concepts Magn Reson 2000;12:173–187. doi: 10.1002/1099-0534(2000)12:4<173::AID-CMR1>3.0.CO;2-Q.

63. Hoult D., Lauterbur PC. The sensitivity of the zeugmatographic experiment involving human samples. J Magn Reson 1979;34:425–433. doi: 10.1016/0022-2364(79)90019-2.

64. Hayes CE, Axel L. Noise performance of surface coils for magnetic resonance imaging at 1.5 T. Med Phys 1985;12:604–7. doi: 10.1118/1.595682.

65. Fujita H, Yang X, Zheng T. Array coil types and design principles. In Proceedings of the 14th Annual Meeting of ISMRM weekend syllabus, Seattle, Washington, USA, 2006.

66. Wang J, Reykowski A, Dickas J. Calculation of the signal-to-noise ratio for simple surface coils and arrays of coils. IEEE Trans Biomed Eng 1995;42:908–917. doi: 10.1109/10.412657.

67. Fujita H, Zheng T, Yang X, Finnerty MJ, Handa S. RF surface receive array coils: the art of an LC circuit. J Magn Reson Imaging 2013;38:12–25. doi: 10.1002/jmri.24159.

68. Yang X, Zheng T, Fujita H. T/R switches, baluns, and detuning elements in MRI RF coils. In Proceedings of the 14th Annual Meeting of ISMRM weekend syllabus, Seattle, Washington, USA, 2006.

69. Nordmeyer-Massner JA, De Zanche N, Pruessmann KP. Noise figure characterization of preamplifiers at NMR frequencies. J Magn Reson 2011;210:7–15. doi: 10.1016/j.jmr.2011.01.025.

70. Roemer PB, Edelstein WA, inventors; General Electric Company, assignee. Nuclear magnetic resonance (NMR) imaging with multiple surface coils. US Patent 4,825,162. April 25, 1989.

71. Erdogmus D, Yan R, Larsson EG, Principe JC, Fitzsimmons JR. Image construction methods for phased array magnetic resonance imaging. J Magn Reson Imaging 2004;20:306–14. doi: 10.1002/jmri.20115.

72. Kumar A, Bottomley PA. Optimized quadrature surface coil designs. MAGMA 2008;21:41–52. doi: 10.1007/s10334-007-0090-2.

73. DeLano MC, Cooper TG, Siebert JE, Potchen MJ, Kuppusamy K. High-b-value diffusion-weighted MR imaging of adult brain: image contrast and apparent diffusion coefficient map features. Am J Neuroradiol 2000;21:1830–1836.

74. Seo HS, Chang K-H, Na DG, Kwon BJ, Lee DH. High b-value diffusion (b = 3000 s/mm2) MR imaging in cerebral gliomas at 3T: visual and quantitative comparisons with b = 1000 s/mm2. Am J Neuroradiol 2008;29:458–63. doi: 10.3174/ajnr.A0842.

75. Cihangiroglu M, Citci B, Kilickesmez O, Firat Z, Karlıkaya G, Uluğ AM, Bingol CA, Kovanlikaya I. The utility of high b-value DWI in evaluation of ischemic stroke at 3T. Eur J Radiol 2011;78:75–81. doi: 10.1016/j.ejrad.2009.10.011.

76. Horsfield MA, Jones DK. Applications of diffusion-weighted and diffusion tensor MRI to white matter diseases - a review. NMR Biomed 2002;15:570–7. doi: 10.1002/nbm.787.

77. Nilsson M, Lätt J, Nordh E, Wirestam R, Ståhlberg F, Brockstedt S. On the effects of a varied diffusion time in vivo: is the diffusion in white matter restricted? Magn Reson Imaging 2009;27:176–87. doi: 10.1016/j.mri.2008.06.003.

78. Rangwala NA, Hackney DB, Dai W, Alsop DC. Diffusion restriction in the human spinal cord characterized in vivo with high b-value STEAM diffusion imaging. Neuroimage 2013;82:416–25. doi: 10.1016/j.neuroimage.2013.05.122.

79. Hwang SN, Chin C-L, Wehrli FW, Hackney DB. An image-based finite difference model for simulating restricted diffusion. Magn Reson Med 2003;50:373–82. doi: 10.1002/mrm.10536.

80. Inglis BA, Bossart EL, Buckley DL, Wirth ED, Mareci TH. Visualization of neural tissue water compartments using biexponential diffusion tensor MRI. Magn Reson Med 2001;45:580–587. doi: 10.1002/mrm.1079.

81. Mulkern RV, Gudbjartsson H, Westin CF, et al. Multi-component apparent diffusion

coefficients in human brain. NMR Biomed 1999;12:51–62.

82. Mulkern RV, Zengingonul HP, Robertson RL, et al. Multi-component apparent diffusion coefficients in human brain: relationship to spin-lattice relaxation. Magn Reson Med 2000;44:292–300.

83. Niendorf T, Dijkhuizen RM, Norris DG, van Lookeren Campagne M, Nicolay K. Biexponential diffusion attenuation in various states of brain tissue: implications for diffusion-weighted imaging. Magn Reson Med 1996;36:847–57.

84. Van Zijl PC, Moonen CT, Faustino P, Pekar J, Kaplan O, Cohen JS. Complete separation of intracellular and extracellular information in NMR spectra of perfused cells by diffusion-weighted spectroscopy. Proc Natl Acad Sci USA 1991;88:3228–32.

85. Beaulieu C. The basis of anisotropic water diffusion in the nervous system - a technical review. NMR Biomed 2002;15:435–55. doi: 10.1002/nbm.782.

86. Nilsson M, van Westen D, Ståhlberg F, Sundgren PC, Lätt J. The role of tissue microstructure and water exchange in biophysical modelling of diffusion in white matter. MAGMA 2013;26:345–70. doi: 10.1007/s10334-013-0371-x.

87. MacKay A, Whittall K, Adler J, Li D, Paty D, Graeb D. In vivo visualization of myelin water in brain by magnetic resonance. Magn Reson Med 1994;31:673–7.

88. Assaf Y, Freidlin RZ, Rohde GK, Basser PJ. New modeling and experimental framework to characterize hindered and restricted water diffusion in brain white matter. Magn Reson Med 2004;52:965–78. doi: 10.1002/mrm.20274.

89. Neuman CH. Spin echo of spins diffusing in a bounded medium. J Chem Phys 1974;60:4508. doi: 10.1063/1.1680931.

90. van Gelderen P, DesPres D, van Zijl PC, Moonen CT. Evaluation of restricted diffusion in cylinders. Phosphocreatine in rabbit leg muscle. J Magn Reson B 1994;103:255–60.

91. Callaghan PT. Pulsed-gradient spin-echo NMR for planar, cylindrical, and spherical pores under conditions of wall relaxation. J Magn Reson Ser A 1995;113:53–59. doi: 10.1006/jmra.1995.1055.

92. Kiselev VG. The cumulant expansion: an overarching mathematical framework for understanding diffusion NMR. In: D.K. Jones (Ed.) Diffusion MRI: theory, methods, and applications. Oxford University Press; New York 2011. p 152–168.

93. Jensen JH, Helpern JA, Ramani A, Lu H, Kaczynski K. Diffusional kurtosis imaging: The quantification of non-gaussian water diffusion by means of magnetic resonance imaging. Magn Reson Med 2005;53:1432–1440. doi: 10.1002/mrm.20508.

94. Sapkota N, Shi X, Shah LM, Bisson EF, Rose JW, Jeong E-K. Two-dimensional

single-shot diffusion-weighted stimulated EPI with reduced FOV for ultrahigh-b radial diffusion-weighted imaging of spinal cord. Magn Reson Med 2016. doi: 10.1002/mrm.26302.

95. Assaf Y, Cohen Y. Non-mono-exponential attenuation of water and N-acetyl aspartate signals due to diffusion in brain tissue. J Magn Reson 1998;131:69–85. doi: 10.1006/jmre.1997.1313.

96. Pfeuffer J, Provencher SW, Gruetter R. Water diffusion in rat brain in vivo as detected at very largeb values is multicompartmental. Magn Reson Mater Physics, Biol Med 1999;8:98–108.

97. Assaf Y, Cohen Y. Assignment of the water slow-diffusing component in the central nervous system using q-space diffusion MRS: implications for fiber tract imaging. Magn Reson Med 2000;43:191–9.

98. Meier C, Dreher W, Leibfritz D. Diffusion in compartmental systems. I. A comparison of an analytical model with simulations. Magn Reson Med 2003;50:500–9. doi: 10.1002/mrm.10557.

99. Klawiter EC, Schmidt RE, Trinkaus K, Liang H-F, Budde MD, Naismith RT, Song S-K, Cross AH, Benzinger TL. Radial diffusivity predicts demyelination in ex vivo multiple sclerosis spinal cords. Neuroimage 2011;55:1454–60. doi: 10.1016/j.neuroimage.2011.01.007.

100. Kim TH, Zollinger L, Shi XF, Rose J, Jeong E-K. Diffusion tensor imaging of ex vivo cervical spinal cord specimens: the immediate and long-term effects of fixation on diffusivity. Anat Rec (Hoboken) 2009;292:234–41. doi: 10.1002/ar.20823.

101. Sehy JV, Banks AA, Ackerman JJH, Neil JJ. Importance of intracellular water apparent diffusion to the measurement of membrane permeability. Biophys J 2002;83:2856–63. doi: 10.1016/S0006-3495(02)75294-6.

102. Merboldt KD, Hänicke W, Frahm J. Diffusion imaging using stimulated echoes. Magn Reson Med 1991;19:233–9.

103. Grussu F, Schneider T, Zhang H, Alexander DC, Wheeler–Kingshott CAM. Neurite orientation dispersion and density imaging of the healthy cervical spinal cord in vivo. Neuroimage 2015;111:590–601. doi: 10.1016/j.neuroimage.2015.01.045.

104. Kodiweera C, Wu Y-C. Data of NODDI diffusion metrics in the brain and computer simulation of hybrid diffusion imaging (HYDI) acquisition scheme. Data Br 2016;7:1131–8. doi: 10.1016/j.dib.2016.03.063.

105. Ronen I, Budde M, Ercan E, Annese J, Techawiboonwong A, Webb A. Microstructural organization of axons in the human corpus callosum quantified by diffusion-weighted magnetic resonance spectroscopy of N-acetylaspartate and post-mortem histology. Brain Struct Funct 2014;219:1773–85.

106. Lasič S, Oredsson S, Partridge SC, Saal LH, Topgaard D, Nilsson M, Bryskhe K. Apparent exchange rate for breast cancer characterization. NMR Biomed 2016;29:631–9. doi: 10.1002/nbm.3504.

107. Lampinen B, Szczepankiewicz F, van Westen D, Englund E, C Sundgren P, Lätt J, Ståhlberg F, Nilsson M. Optimal experimental design for filter exchange imaging: Apparent exchange rate measurements in the healthy brain and in intracranial tumors. Magn Reson Med 2016. doi: 10.1002/mrm.26195.

108. Nilsson M, Lätt J, van Westen D, Brockstedt S, Lasič S, Ståhlberg F, Topgaard D. Noninvasive mapping of water diffusional exchange in the human brain using filter-exchange imaging. Magn Reson Med 2013;69:1573–81. doi: 10.1002/mrm.24395.

109. Aslund I, Nowacka A, Nilsson M, Topgaard D. Filter-exchange PGSE NMR determination of cell membrane permeability. J Magn Reson 2009;200:291–295. doi: 10.1016/j.jmr.2009.07.015.

110. Sapkota N, Rose J, Miller S, Bowman B, Shah L, Bisson E, Yoon S, Jeong EK. Estimation of intra-axonal fraction in spinal cord white matter by using Monte Carlo simulation of water diffusion and high b-value diffusion sensitized MRI. In Proceedings of the 23rd Annual Meeting of ISMRM, Toronto, Canada, 2015. Abstract 3044.

111. Facon D, Ozanne A, Fillard P, Lepeintre JF, Tournoux-Facon C, Ducreux D. MR diffusion tensor imaging and fiber tracking in spinal cord compression. Am J Neuroradiol 2005;26:1587–1594.

112. Bammer R, Fazekas F, Augustin M, Simbrunner J, Strasser-Fuchs S, Seifert T, Stollberger R, Hartung HP. Diffusion-weighted MR imaging of the spinal cord. Am J Neuroradiol 2000;21:587–91.

113. Maier SE, Mamata H. Diffusion tensor imaging of the spinal cord. Annals of the New York Academy of Sciences 2005;1064:50–60.

114. Clark CA, Werring DJ. Diffusion tensor imaging in spinal cord: Methods and applications - A review. NMR Biomed 2002;15:578–586. doi: 10.1002/nbm.788.

115. Shanmuganathan K, Gullapalli RP, Zhuo J, Mirvis SE. Diffusion tensor MR imaging in cervical spine trauma. Am J Neuroradiol 2008;29:655–659. doi: 10.3174/ajnr.A0916.

116. Griswold MA, Jakob PM, Heidemann RM, Nittka M, Jellus V, Wang J, Kiefer B, Haase A. Generalized autocalibrating partially parallel acquisitions (GRAPPA). Magn Reson Med 2002;47:1202–10. doi: 10.1002/mrm.10171.

117. Sodickson DK, Manning WJ. Simultaneous acquisition of spatial harmonics (SMASH): Fast imaging with radiofrequency coil arrays. Magn Reson Med 1997;38:591–603. doi: 10.1002/mrm.1910380414.

118. Guclu CC, Boskamp E, Zheng T, Becerra R, Blawat L. A method for preamplifier-decoupling improvement in quadrature phased-array coils. J Magn Reson Imaging 2004;19:255–8. doi: 10.1002/jmri.10449.

119. Li Y, Xie Z, Pang Y, Vigneron D, Zhang X. ICE decoupling technique for RF coil array designs. Med Phys 2011;38:4086–93.

120. Keren H, inventor; Elscint, Ltd., assignee. Quadrature surface coil array. US Patent 5,198,768. March 30, 1993.

121. Adriany G, Van de Moortele P-F, Wiesinger F, et al. Transmit and receive transmission line arrays for 7 Tesla parallel imaging. Magn Reson Med 2005;53:434–45. doi: 10.1002/mrm.20321.

122. Wright S, Wald L. Theory and applications of array coils in MR spectroscopy. NMR Biomed 1997;10:394–410.

123. Keil B, Biber S, Rehner R, Tountcheva V, Wohlfarth K, Hoecht P, Hamm M, Meyer H, Fischer HJ, Wald LL. A 64-channel array coil for 3T head/neck/C-spine imaging. In Proceedings of the 19th Annual Meeting of ISMRM, Montreal, Quebec, Canada, 2011. p. 160.

124. Reykowski A, Hemmerlein M, Fischer H. 16 channel head/neck matrix coils for 3 tesla. In Proceedings of the 13th Annual Meeting of ISMRM, Miami, Florida, USA, 2005. p. 908.

125. Bodurka J, Ledden P, Bandettini P. SENSE optimized sixteen element receive array for cervical spinal cord imaging at 3 T. In Proceedings of the 16th Annual Meeting of ISMRM, Toronto, Ontario, Canada, 2008. p. 1078.

126. Sapkota N, Kaggie J, Hadley R, Jeong E-K. A semi-optimized phased array coil design for high-resolution MRI of cervical spinal cord. In Proceedings of the 21st Annual Meeting of ISMRM, Salt Lake City, Utah, USA, 2013. p. 2736.

127. Peterson DM, Duensing GR, Caserta J, Fitzsimmons JR. An MR transceive phased array designed for spinal cord imaging at 3 Tesla: preliminary investigations of spinal cord imaging at 3 T. Invest Radiol 2003;38:428–435.

128. Cohen-Adad J, Mareyam A, Keil B, Polimeni JR, Wald LL. 32-Channel RF coil optimized for brain and cervical spinal cord at 3 T. Magn Reson Med 2011;66:1198–1208. doi: 10.1002/mrm.22906.

129. Zhang B, Balchandani P, Fayad ZA, Kim J, Cannistraci C, Stoeckel B, Junqian X. 7T 2ch wrap-around coil array for cervical spinal cord imaging. In Proceedings of the 23rd Annual Meeting of ISMRM, Toronto, Ontario, Canada, 2015. p. 0626.

130. Kraff O, Bitz AK, Kruszona S, Orzada S, Schaefer LC, Theysohn JM, Maderwald S, Ladd ME, Quick HH. An eight-channel phased array RF coil for spine MR imaging at 7

T. Invest Radiol 2009;44:734–40. doi: 10.1097/RLI.0b013e3181b24ab7.

131. Sigmund EE, Suero GA., Hu C, Mcgorty K, Sodickson DK, Wiggins GC, Helpern J a. High-resolution human cervical spinal cord imaging at 7T. NMR Biomed 2012;25:891–899. doi: 10.1002/nbm.1809.

132. Vossen M, Teeuwisse W, Reijnierse M, Collins CM, Smith NB, Webb AG. A radiofrequency coil configuration for imaging the human vertebral column at 7 T. J Magn Reson 2011;208:291–297. doi: 10.1016/j.jmr.2010.11.004.

133. Zhao W, Cohen-Adad J, Polimeni JR, Keil B, Guerin B, Setsompop K, Serano P, Mareyam A, Hoecht P, Wald LL. Nineteen-channel receive array and four-channel transmit array coil for cervical spinal cord imaging at 7T. Magn Reson Med 2014;72:291–300. doi: 10.1002/mrm.24911.

134. Petropoulos LS, Zou MX, Zheng T, inventors; General Electric Company, assignee. Integrated cervical-thoracic-lumbar spine MRI array coil. US Patent 6,980,002. December 27, 2005.

135. Chan PH, Guan Y, Robb FJ, Su S, inventors; General Electric Company, assignee. Quadrature and linear RF coil array for MRI of human spine and torso. US Patent 8,441,258. May 14, 2013.

136. Hoult DI. The principle of reciprocity in signal strength calculations?A mathematical guide. Concepts Magn Reson 2000;12:173–187. doi: 10.1002/1099-0534(2000)12:4<173:AID-CMR1>3.0.CO;2-Q.

137. Edelstein WA, Hardy CJ, Mueller OM. Electronic decoupling of surface-coil receivers for NMR imaging and spectroscopy. J Magn Reson 1986;67:156–161.

138. Jeong E-K, Kim S-E, Guo J, Kholmovski EG, Parker DL. High-resolution DTI with 2D interleaved multislice reduced FOV single-shot diffusion-weighted EPI (2D ss-rFOV-DWEPI). Magn Reson Med 2005;54:1575–9. doi: 10.1002/mrm.20711.

139. Hayes CE, Roemer PB. Noise correlations in data simultaneously acquired from multiple surface coil arrays. Magn Reson Med 1990;16:181–91.

140. Constantinides CD, Atalar E, McVeigh ER. Signal-to-noise measurements in magnitude images from NMR phased arrays. Magn Reson Med 1997;38:852–7.

141. Kellman P, McVeigh ER. Image reconstruction in SNR units: a general method for SNR measurement. Magn Reson Med 2005;54:1439–47. doi: 10.1002/mrm.20713.

142. Hesseltine SM, Law M, Babb J, Rad M, Lopez S, Ge Y, Johnson G, Grossman RI. Diffusion tensor imaging in multiple sclerosis: assessment of regional differences in the axial plane within normal-appearing cervical spinal cord. Am J Neuroradiol 2006;27:1189–93.

143. Deo AA, Grill RJ, Hasan KM, Narayana PA. In vivo serial diffusion tensor imaging of experimental spinal cord injury. J Neurosci Res 2006;83:801–10. doi: 10.1002/jnr.20783.

144. Reese TG, Heid O, Weisskoff RM, Wedeen VJ. Reduction of eddy-current-induced distortion in diffusion MRI using a twice-refocused spin echo. Magn Reson Med 2003;49:177–82. doi: 10.1002/mrm.10308.

145. Noehren B, Andersen A, Feiweier T, Damon B, Hardy P. Comparison of twice refocused spin echo versus stimulated echo diffusion tensor imaging for tracking muscle fibers. J Magn Reson Imaging 2015;41:624–32. doi: 10.1002/jmri.24585.

146. Steidle G, Schick F. Echoplanar diffusion tensor imaging of the lower leg musculature using eddy current nulled stimulated echo preparation. Magn Reson Med 2006;55:541–8. doi: 10.1002/mrm.20780.

147. Brihuega-Moreno O, Heese FP, Hall LD. Optimization of diffusion measurements using Cramer-Rao lower bound theory and its application to articular cartilage. Magn Reson Med 2003;50:1069–76. doi: 10.1002/mrm.10628.

148. Shepherd TM, Thelwall PE, Stanisz GJ, Blackband SJ. Aldehyde fixative solutions alter the water relaxation and diffusion properties of nervous tissue. Magn Reson Med 2009;62:26–34. doi: 10.1002/mrm.21977.

149. Ong HH, Wehrli FW. Quantifying axon diameter and intra-cellular volume fraction in excised mouse spinal cord with q-space imaging. Neuroimage 2010;51:1360–6. doi: 10.1016/j.neuroimage.2010.03.063.

150. Saritas EU, Cunningham CH, Lee JH, Han ET, Nishimura DG. DWI of the spinal cord with reduced FOV single-shot EPI. Magn Reson Med 2008;60:468–473. doi: 10.1002/mrm.21640.

151. Wheeler-Kingshott CAM, Hickman SJ, Parker GJM, Ciccarelli O, Symms MR, Miller DH, Barker GJ. Investigating cervical spinal cord structure using axial diffusion tensor imaging. Neuroimage 2002;16:93–102. doi: 10.1006/nimg.2001.1022.

152. Wilm BJ, Svensson J, Henning A, Pruessmann KP, Boesiger P, Kollias SS. Reduced field-of-view MRI using outer volume suppression for spinal cord diffusion imaging. Magn Reson Med 2007;57:625–630. doi: 10.1002/mrm.21167.

153. Turner R, Le Bihan D, Maier J, Vavrek R, Hedges LK, Pekar J. Echo-planar imaging of intravoxel incoherent motion. Radiol 1990;177:407–14. doi: 10.1148/radiology.177.2.2217777.

154. Soellinger M, Langkammer C, Seifert-Held T, Fazekas F, Ropele S. Fast bound pool fraction mapping using stimulated echoes. Magn Reson Med 2011;66:717–24. doi: 10.1002/mrm.22846.

155. Frahm J, Merboldt K-D, Hänicke W. Localized proton spectroscopy using stimulated echoes. J Magn Reson 1987;72:502–508. doi: 10.1016/0022-2364(87)90154-5.

156. Holz M, Heil SR, Sacco A. Temperature-dependent self-diffusion coefficients of water and six selected molecular liquids for calibration in accurate 1H NMR PFG measurements. Phys Chem Chem Phys 2000;2:4740–4742. doi: 10.1039/b005319h.

157. Mills R. Self-diffusion in normal and heavy water in the range 1-45.deg. J Phys Chem 1973;77:685–688. doi: 10.1021/j100624a025.

158. Ropele S, Seifert T, Enzinger C, Fazekas F. Method for quantitative imaging of the macromolecular 1H fraction in tissues. Magn Reson Med 2003;49:864–71. doi: 10.1002/mrm.10427.

159. Farrell JAD, Smith SA, Gordon-Lipkin EM, Reich DS, Calabresi PA, van Zijl PCM. High b-value q-space diffusion-weighted MRI of the human cervical spinal cord in vivo: feasibility and application to multiple sclerosis. Magn Reson Med 2008;59:1079–89. doi: 10.1002/mrm.21563.